ACTINIDE CONCENTRATION MONITORING AND EXTRACTION FROM MOLTEN FLUORIDE AND CHLORIDE SALTS

by

Milan Stika

A dissertation submitted to the faculty of
The University of Utah
in partial fulfillment of the requirements for the degree of

Doctor of Philosophy

Department of Metallurgical Engineering

The University of Utah

December 2017

The University of Utah Graduate School

STATEMENT OF DISSERTATION APPROVAL

The dissertation of **Milan Stika**

has been approved by the following supervisory committee members:

Michael F. Simpson ,	Chair(s)	**15 August 2017** Date Approved
Michael L. Free ,	Member	**15 August 2017** Date Approved
York Reed Smith ,	Member	**15 August 2017** Date Approved
Henry S. White ,	Member	**15 August 2017** Date Approved
Guy Fredrickson ,	Member	**15 August 2017** Date Approved

by **Manoranjan Misra** , Chair/Dean of

the Department/College/School of **Metallurgical Engineering**

and by **David B. Kieda** , Dean of The Graduate School.

ABSTRACT

The electrochemical properties of actinides in molten salt are of importance in the nuclear pyrochemical material processing. Specifically, the ability to perform fast (real-time) concentration monitoring in such environments is of great importance (and currently not developed). This dissertation aims to develop such concentration monitoring tools that could be applied to either Generation IV nuclear reactor systems, or to spent fuel pyroprocessing.

The application in Generation IV systems is treated in the first part of the dissertation. Here, fluoride salts containing thorium and uranium have been investigated using an electrochemical technique called cyclic voltammetry. Signal to concentration correlations have been developed for single-analyte and mixed salts, and other electrochemical data were collected (reduction mechanism, reversibility criteria, diffusion coefficient).

The application in spent fuel pyroprocessing is treated in the second part of the dissertation. Here, chloride salts containing thorium and uranium have been investigated using a variety of electrodeposition techniques (chronoamperometry, chronopotentiometry, repeating chronoamperometry). A new, hyphenated analytical technique was developed, which combines a separation step (electrochemical deposition) with a detection step (alpha particle spectroscopy).

A theoretical framework for this new technique was presented, together with experimental verification. The verification (signal to concentration correlation) was complicated by unexpectedly low deposition rate in the mixed salt. This interference prompted investigation, and produced a hypothesis which attempts to explain the lower rate as being the result of departure from the mass transfer-limited deposition regime.

Haničce

CONTENTS

LIST OF FIGURES

LIST OF TABLES

LIST OF ACRONYMS

Acronym	Meaning
AIChE	American Institute of Chemical Engineers
CA	Chronoamperometry / chronoamperogram
CE	Counter electrode
CP	Chronopotentiometry / chronopotentiogram
CV	Cyclic voltammetry / voltammogram
FP	Fission product(s)
ICP-AES	Inductively-coupled plasma atomic emission spectrometry
ICP-MS	Inductively-coupled plasma mass spectrometry
LFTR	Liquid Fluoride Thorium Reactor
MOX	Mixed-oxide fuel
MSR	Molten salt reactor
MSRE	Molten Salt Reactor Experiment
NPV	Normal pulse voltammetry
ORNL	Oak Ridge National Laboratory
PCR	Principal component regression
RCA	Repeating chronoamperometry / chronoamperogram
RE	Reference electrode
SEM-EDS	Scanning electron microscopy with energy dispersive X-ray spectroscopy
TRU	Transuranic element
UNF	Used nuclear fuel
WE	Working electrode

NOTATION AND SYMBOLS

Symbol	Meaning
α	Transfer coefficient
Γ	Electron transfer to mass transfer ratio
η	Overpotential
ν	Scan rate
ρ	Density
τ	Transition time
τ_{RC}	Cell time constant
a_{ox}, a_{red}	Activity of oxidized (reduced) species
A	Electrode area
c	Bulk species concentration
c_{ox}, c_{red}	Surface concentration of oxidized (reduced) species
C_d	Double-layer capacitance
D_i	Distribution coefficient
D_{ox}, D_{red}	Diffusion coefficient of oxidized (reduced) species
e_p	Peak height
E	Applied potential
E^0	Standard redox potential
$E^{0'}$	Apparent standard redox potential
E_{acc}	Accelerating voltage (SEM)
E_i	Initial potential
$E_p, E_p/2$	Peak potential, half peak potential
E_{pulse}	Pulse potential

Symbol	Meaning
E_{relax}	Relaxation potential
E_s	Switching potential
F	Faraday's constant
ΔG_f	Free energy of formation
h	Immersion depth
I, i	Current (density)
I_0, i_0	Exchange current (density)
i_a, i_c	Anodic (cathodic) current density
i_{avg}	Average current density
I_c	Charging current
i_d	Diffusion-limited current density
I_f	Faradaic current
I_l, i_l	Limiting current (density)
I_p	Peak current
i_{tot}	Total observed current density
k	Proportionality constant
k^0	Standard heterogeneous rate constant
k_f, k_b	Forward (backward) reaction rate constant
m	Mass transfer coefficient
M	Atomic mass
n	Number of moles
Q	Charge
Q_{raw}	Raw charge
Q_{tot}	Total charge
R	Universal gas constant
R_s	Solution resistance
t	Time

Symbol	Meaning
t_a, t_c	Anodic (cathodic) current duration
t_{raw}	Raw deposition time
T	Temperature
W_p	Peak width
X_i	Mole fraction
z	Number of exchanged electrons
Z	Atomic number
z_{max}	Analytical area (SEM)

ACKNOWLEDGEMENTS

Many people were instrumental in making this work possible. First of all, I would like to thank my advisor Dr. Michael Simpson for having me, and for all the guidance, support, and kindness he provided during my time at the University of Utah. It was a pleasure to be a graduate student under your supervision.

I would like to thank Dr. Laurent Massot from Laboratoire de Génie Chimique (Toulouse, France) for many valuable e-mail discussions. Another thank you to Dr. Matthew DeLong from the Department of Physics and Astronomy at the University of Utah, and Dr. Jeff Berg from the Idaho National Laboratory for suggestions on sample preparations.

A big thank you goes to my committee member Dr. Guy Fredrickson for improving the dissertation with an immense number of great suggestions. I thank all my lab mates, especially Dr. Devin Rappleye, for their helpful attitude and many scientific (and nonscientific) discussions we had.

Finally, I'd like to thank my family for all the support and blessings I continuously receive from them. I'd like to thank my parents and my brother for always being there when I needed them. My wife Hanka deserves a special thank you for her never-ending love, encouragement, support, tolerance, and understanding. I love you!

CHAPTER 1

INTRODUCTION

In the field of metallurgy, molten salt electrochemistry has been used for extractive metallurgy of aluminum and magnesium (prospectively titanium) (1). Its other application, explored in this dissertation, pertains to nuclear material processing.

The Oak Ridge National Laboratory (ORNL) demonstrated with a pilot plant in the 1960s that a nuclear reactor featuring a molten salt as its fuel is a possibility, with several advantages over traditional solid-fuel reactors (2–5).

This molten salt reactor (MSR) is now sparking new interest and is part of a Generation IV nuclear reactor initiative (6). The ORNL concept is the basis for other, recently announced variations by several companies, including *Flibe Energy* (US), *Terrapower* (US), *Terrestrial Energy* (CAN), etc. Most of these designs require some form of concentration monitoring of fissile elements and potentially other elements in the salt as well. *Part I* of this dissertation aims to provide real-time concentration monitoring of actinides (especially fissile actinides)—a crucial analytical tool to enable optimal reactor control.

The original ORNL design features an on-site salt treatment facility, which may incorporate element extraction (either actinide or rare-earth group) and reintroduction as part of the clean-up procedure (7). For instance Flibe Energy's Liquid Fluoride Thorium Reactor (LFTR) features such extraction/reintroduction of elements in the salt (8). This salt processing would greatly benefit from having a real-time process monitoring tool. *Part I* of the dissertation covers such process monitoring as well.

Similar to the salt treatment for MSR, used nuclear fuel (UNF) from traditional solid fuel reactors can also be processed in a molten salt bath to recycle valuable elements and close the nuclear fuel cycle. This treatment based on molten chloride electrochemistry exists on a pilot scale and is called pyroprocessing (9). The process

is currently being developed into commercial stage particularly in the Republic of Korea (10) to treat all their domestic production of UNF in such a facility.

The most instrumental unit operation of the pyroprocessing flowsheet is the electrorefiner, which selectively extracts actinides from the UNF by electrodeposition onto a cathode. Concentration monitoring and optimization of the extraction is a top priority in this application and *Part II* of the dissertation explores this electrorefiner monitoring.

Specifically, a novel, hyphenated concentration monitoring technique is introduced that combines electrodeposition separation step with alpha spectroscopy detection. The idea is to deposit (preconcentrate) a thin layer of actinide metal from the molten salt bath onto the cathode, which itself is a semiconductor alpha particle detector. This detector then collects an alpha particle spectrum. Based on the spectrum, individual isotopes are identified, and—if combined with the electrochemical signal from the deposition step—their amounts quantified. The electrochemical signal from the deposition step is therefore combined with the alpha spectrum signal to determine individual analyte concentrations in the salt—something very difficult to achieve using only a single technique.

Thus, the dissertation is divided into two parts: *Part I* concerns fluoride salt work (MSR reactor monitoring and associated salt treatment monitoring), while *Part II* concerns chloride salt work (electrorefiner operation monitoring). The reason for this division is a convenience in presenting the two systems separately, since each system explores different approach to achieve the same goal (concentration monitoring). The two parts feature different types of molten salts (fluorides vs. chlorides), different techniques (cyclic voltammetry vs. electrodeposition techniques) and apply to different types of nuclear systems (molten salt reactors vs. electrorefiners).

The common thread of the two parts is the effort to achieve real-time process monitoring of high-temperature systems featuring nuclear materials. Both parts are still encompassed under relatively narrow field of the electrochemical actinide concentration monitoring in molten salts for nuclear applications. Methods used in one system can generally be employed (with modifications) in the other system.

PART I

FLUORIDES

CHAPTER 2

APPLICATION IN MSR TECHNOLOGY

The first portion of this work concerns actinide monitoring in molten fluorides, with application in molten salt reactor electrochemistry. The application is twofold: either direct reactor control, or control of extraction—a particular unit operation of salt processing.

Results from the electrochemical studies in fluorides were published in the AIChE Journal (11). Essential paragraphs, figures and tables from that publication have been reproduced here.

2.1 Molten salt reactor operation

This section introduces in more detail the MSR. To be clear, this refers to nuclear reactors in which the actual fuel is contained in a molten salt solution that circulates through the core and primary heat exchanger. It is necessary to describe this nontraditional, revolutionary nuclear reactor concept in sufficient detail to be able to fully appreciate the benefits that utilization of this concept can bring. Without emphasizing the advantages, the electrochemical concentration monitoring might seem purposeless, due to it being developed for some (currently) nonexisting application. For more details about the MSR concept, a short list of references is given (4, 5, 12–16).

2.1.1 Concept

The ORNL Molten Salt Breeder Reactor concept was envisioned to operate a circulating molten fluoride salt of the following composition (4):

$LiF-BeF_2-ThF_4-UF_4$ (72–16–12–0.3 mol%)

A lithium beryllium fluoride mixture is the base salt with favorable thermo-hydraulic properties: good thermal conductivity, heat capacity, acceptable density

and viscosity. It has also favorable nuclear properties: some moderating capability, negative temperature coefficient of reactivity, very low thermal neutron absorption cross section (lithium has to be enriched in ^{7}Li isotope). Thorium fluoride is a fertile material added for breeding capability, and uranium fluoride (preferably ^{233}U isotope) is the fissile material that produces heat in the process.

This reactor was tailored to perform best in the thorium-uranium fuel cycle, where it produces very little problematic transuranic elements (TRU). Minimization of TRU results in lower radiotoxicity of the waste, implying shorter storage times and perhaps completely avoiding the necessity of building a deep geological repository. The reactor can operate in the traditional uranium-plutonium fuel cycle as well, but then the advantage of TRU minimization is lost—see comparison of both nuclear fuel cycles in Figure 2.1.

The salt circulates in a primary circuit through a reactor core where the fission happens (due to moderating graphite elements being present in the core), into a heat exchanger where the heat is removed (and subsequently converted to electricity) by a secondary circuit, and through a pump back into the reactor core. A small portion of the stream is drawn into a salt processing plant (see next section) where the salt is conditioned. An overview of the reactor is shown in Figure 2.2.

With the renewed interest in MSRs, other concepts utilizing different salts, different neutron spectra or different fuel cycles are emerging (see, for example, websites of *Flibe Energy*, *Terrestrial Energy*, *Terrapower*, or *Transatomic Power*).

The MSR delivers advantages over the traditional solid-fuel reactors in all three aspects of reactor operation (economy, safety, waste management):

- Zero fuel element fabrication cost [economy].
- Continuous refueling (high plant capacity factor) [economy].
- Breeding or self-breeding capability [economy, waste management].
- High thermal efficiency due to high-temperature operation [economy].
- Low-pressure operation, no expensive containment [economy, safety].

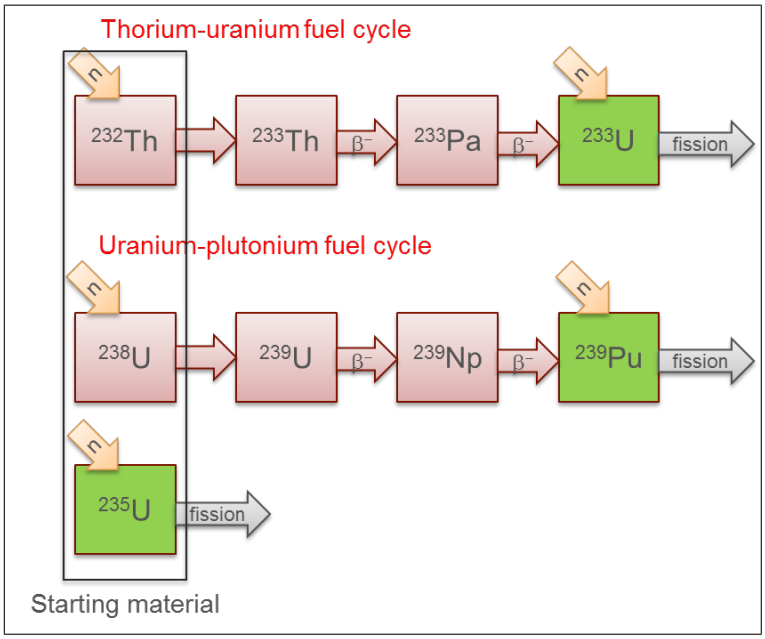

Figure 2.1. Comparison of thorium-uranium and uranium-plutonium fuel cycles. In thorium-uranium cycle the generation of transuranic elements is minimized.

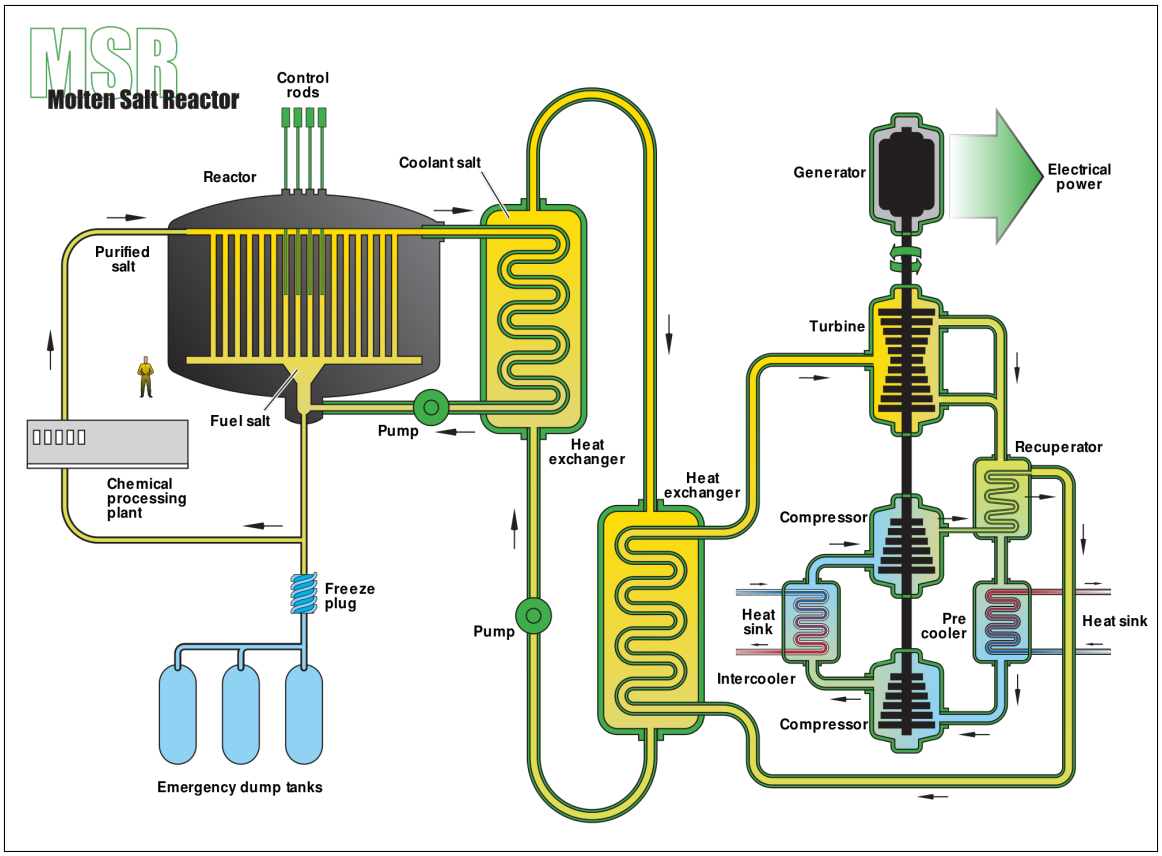

Figure 2.2. Molten salt reactor overview. [U.S. Department of Energy Nuclear Energy Research Advisory Committee, public domain]

- Excellent resistance of salts to irradiation [economy, safety].
- Absence of cladding material translates into no burn-up restrictions [economy, waste management].
- Ability to operate in thorium-uranium fuel cycle [waste management].
- Ability to use in-house reprocessing for waste minimization [waste management].
- Ability to accept UNF from traditional reactors [waste management].
- Salts chemically inert to oxygen or water exposure [safety].
- Operation with low excess reactivity [safety].
- Overall excellent passive safety during normal and anomalous operation [safety].

To illustrate the last item (overall excellent passive safety), consider a scenario based on the Fukushima nuclear reactor accident (rapid reactor shutdown, subsequent loss of power). In MSR designs, the piping features an actively cooled freeze valve which—when melted—diverts the molten salt from the reactor vessel into another, sub-critical vessel with passive cooling (dump tank). This freeze valve will function in the same way if there is a sudden loss of power (active cooling of the valve is interrupted), or if the temperature of the salt is significantly increased by some abnormal action. In all cases the reactor shuts down on its own due to inherently safe design. No operator interaction is required either during or after the shutdown and no core damage is anticipated (since fuel is not in the core, and is already molten). In other words the reactor meets the "walk away safe" criteria, unlike currently operational reactors.

Most of these advantages are the result of a different approach taken, where concepts of chemical engineering are extensively applied in nuclear engineering, which almost never occurred in the past designs (and does not occur even today). The molten salt reactor provides a unique, important nexus of chemical and nuclear engineering.

In order to remain objective, some drawbacks of the technology need to be stated as well. One such drawback is the necessity of using special materials—the vessel

and piping requires corrosion resistant nickel-based alloy instead of traditional, less expensive stainless steel. Lithium content needs to be enriched in ^{7}Li isotope if operating in (epi)thermal neutron spectrum, something that would incur extra costs (however, the comparatively more expensive enrichment of uranium required by most traditional reactors is mitigated). Also, the chemical processing adds another level of complexity not seen by traditional reactor systems.

2.1.2 Reactor monitoring

By monitoring the actinide concentration (uranium and thorium, or uranium and thorium and plutonium—depending on the fuel cycle) in the reactor salt, one would be able to regulate the nuclear chain reaction and optimize reactor performance.

For example, if too few uranium fissile isotopes are present in the core, the chain reaction cannot be sustained. Injection of more uranium fluoride is then necessary to increase the concentration of these fissile isotopes. Likewise, if the concentration is higher than necessary, reactor output will increase, which can be either desired (reaching operation at higher power level) or undesired (power excursion) scenario.

In case of thorium, too few fertile atoms signify that the breeding capability is not fully utilized. Likewise, too many thorium atoms interfere with the fission chain reaction by capturing too many neutrons, in which case the performance of the reactor is again suboptimal.

Monitoring the actinide concentration in real time is therefore crucial. This work explores the applicability of cyclic voltammetry (CV) as a method of rapid determination of uranium and thorium concentrations in a surrogate reactor salt.

2.2 Salt processing

This section introduces the salt processing which is an integral part of the MSR design. Process control of one particular unit operation—the molten salt/molten bismuth reductive extraction—is described in more detail.

2.2.1 Concept

In order to maintain optimum performance, the reactor salt needs periodic clean-up. In general, the salt processing serves three purposes:

- Remove neutron poisons.
- Separate newly bred fuel from salt stream.
- Reintroduce actinides into reactor for transmutation.

The diligence with which these three principles are pursued depends on how ambitious the operation goals are.

If breeding ratio over one (more fissile material is generated than consumed) and strict separation of fission products (FP) waste is desired (avoiding the necessity of deep geological repository), then on-line continuous reprocessing with high throughput is required. If self-breeding is desired, on-line reprocessing with low feed rate is sufficient. If breeding is not a goal, thorium can be eliminated from the system and the clean-up process becomes simpler and less frequent.

The advantage of having a molten system is that a small stream can be diverted from the main pipeline into the clean-up facility, and then returned back to the main pipeline again.

The clean-up process was conceived to contain these unit operations:

- Molten salt fluorination (to remove uranium as gaseous UF_6).
- Molten salt/molten bismuth reductive extraction (to isolate protactinium and/or fission products).
- Fuel reconstitution.

Other possible operations considered are vacuum distillation, and electrodeposition of actinides onto solid or liquid cathodes.

2.2.2 Reductive extraction

Molten salt/molten bismuth reductive extraction is a liquid-liquid reactive extraction process where two immiscible liquids are contacted and analyte's oxidation state is lowered by a reducing agent. This causes it to extract into the other liquid. In our case, actinides (thorium, uranium) are analytes present as fluorides in molten salt, and lithium metal present in molten bismuth (forming an alloy) is the reducing agent.

Lithium reduces actinides and they transfer into bismuth. The extraction proceeds according to the following reactions:

$$ThF_4(salt) + 4Li(bismuth) \rightleftarrows Th(bismuth) + 4LiF(salt) \tag{2.1}$$

$$UF_4(salt) + 4Li(bismuth) \rightleftarrows U(bismuth) + 4LiF(salt) \tag{2.2}$$

Different analytes are reduced with variable ease and their solubility in bismuth is also variable, thus, separation between analytes is achieved. Reductive extraction can separate actinides from FPs (4, 7, 17, 18), which is a widely recognized feature not explored in this thesis. Instead, attention is brought towards thorium-uranium separation.

In the MSR design described above (where thorium and uranium are in the same salt), there is little reason to separate them using reductive extraction, since uranium is already separated by the (preceding) fluorination unit operation. However, there are alternative MSR designs, which call for a second fluid—a blanket surrounding the primary (reactor) salt and containing large amounts of thorium. Such a concept is depicted in Figure 2.3.

The fertile thorium blanket would catch escaping neutrons and transmute into protactinium and later into fissile uranium (^{233}U) according to the scheme below:

$$n + {}^{232}_{90}Th \rightarrow {}^{233}_{90}Th \xrightarrow{\beta-} {}^{233}_{90}Pa \xrightarrow{\beta-} {}^{233}_{90}U \tag{2.3}$$

This blanket design vastly improves the breeding capacity of the MSR. Moreover, it eliminates thorium from the reactor salt, which is beneficial in simplifying some of salt processing operations. Paradoxically, ORNL was initially pursuing this—more convoluted—design and only later on switched to a single-fluid design (due to a breakthrough in separation technology that allowed thorium to be mixed in with lanthanides in a single salt).

In order to harness this newly bred fissile material, a U/Th separation technology needs to be applied to this blanket salt. Salt fluorination is one option, converting uranium into gaseous UF_6. However, its precursor from Equation 2.3—protactinium—is not volatilized in this process and remains in the salt. This is detrimental, because in a neutron flux normally seen by the blanket salt ^{233}Pa can transmute into ^{234}Pa and

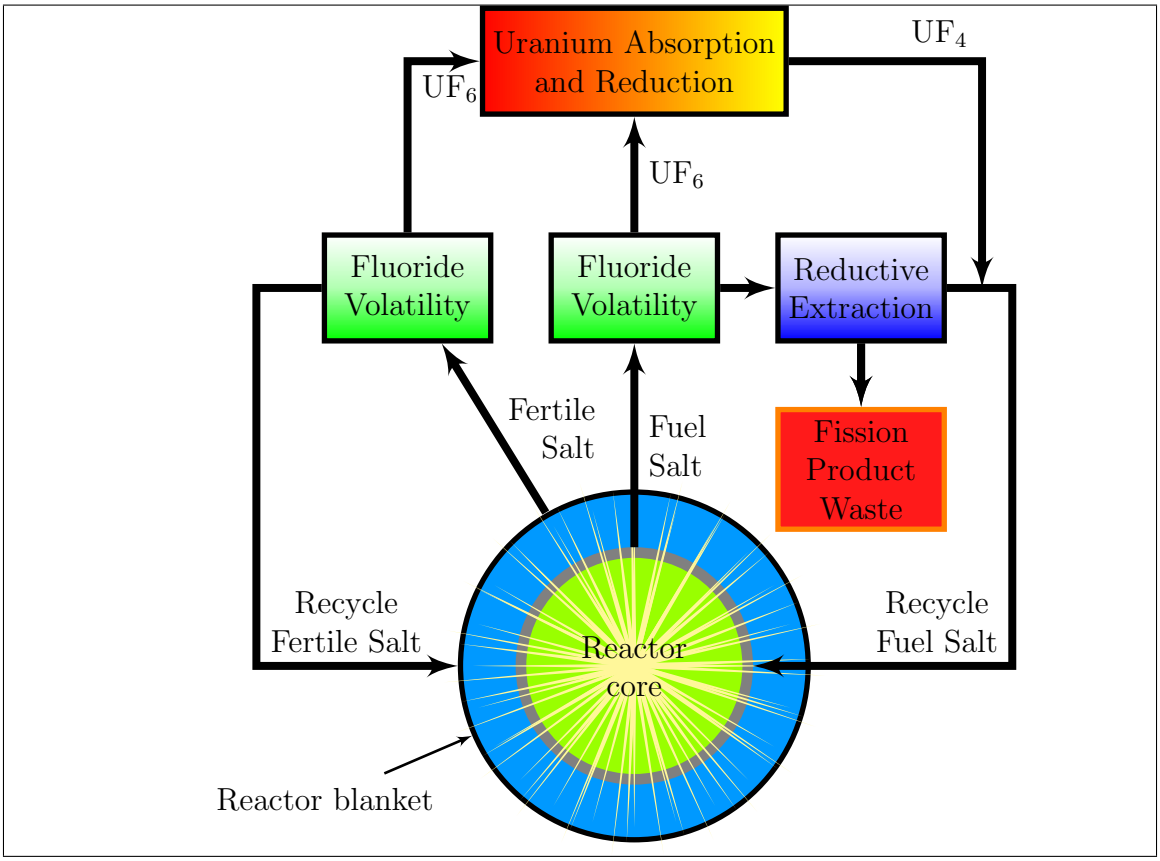

Figure 2.3. Two-fluid molten salt reactor concept. [© Kirk Sorensen]

is lost. Reductive extraction, on the other hand, can advantageously extract both protactinium and uranium into bismuth, while leaving thorium in the salt.

Once both protactinium and uranium are separated from the circulating salt, they can be stored in a tank where protactinium is allowed to decay. A periodic fluorination of this stagnant salt will produce pure UF_6, leaving any un-decayed protactinium behind. This newly bred uranium is then converted to the desired chemical form UF_4 and either added to the reactor or sold as a product.

A distribution coefficient D_i defined below specifies the ratio according to which an analyte i distributes itself between the two phases:

$$D_i = \frac{X_{i,bismuth}}{X_{i,salt}} \tag{2.4}$$

where X_i represents the mole fraction of analyte i in particular phase. Mole fraction can be exchanged for other concentration quantity, but is most often used in molten salt field.

2.2.3 Extraction process monitoring

Thorium has a lower distribution coefficient than the two other actinides (protactinium, uranium), which is beneficial, but some portion of it still extracts into bismuth. The goal is to quantitatively extract all the protactinium and uranium, and accept that some co-extraction of thorium happens. The co-extraction should be minimized by a suitable process control.

This work explores the applicability of CV to monitor in real-time the progress of extraction and to mark its completeness, so that the process can be stopped at the right time. Electrodes monitoring uranium concentration in the salt should report gradual peak diminishing until the peak essentially disappears, as uranium (and protactinium) is being extracted into bismuth.

CHAPTER 3

LITERATURE SURVEY

The only operational MSR to date was an experimental unit under the Molten Salt Reactor Experiment (MSRE) program, operated in the 1960s by ORNL (5). All data regarding actual reactor operation are therefore limited to that period. This experimental unit did not feature thorium blanket, nor any sophisticated salt processing routine (although the salt processing was being simultaneously developed). Also, the reactor power output was low (8 MW_{th} maximum), signifying the alteration of salt composition due to fission was next to negligible (reactor accumulated a total 70,000 MWh of operation).

There was no direct (electro) chemical monitoring present; the reactor operation relied exclusively on reactivity balance calculations. Chemical analysis was performed only on salt samples which were drawn several times a week. Coulometric titrations (19) of aqueous solutions were done to determine uranium content. Oxide concentration was analyzed by evaluation of H_2O produced upon treatment of the sample with anhydrous HF (20). Uranium ratio U(IV)/U(III)—an important indicator of the oxidizing power of the salt (and therefore its corrosiveness towards structural materials)—was reported to be "*especially difficult* [to measure]" (4).

From this point of view, electrochemical actinide monitoring using CV (or other electrochemical technique) would prove helpful (especially with salt redox potential), but unnecessary in this particular small scale reactor. On the other hand, a commercial-scale reactor with much larger power output would certainly benefit from real-time electrochemical data (corrosion mitigation, economy of operation).

Following the success of MSRE, a development of 1,000 MW_e demonstration unit featuring both thorium and sophisticated salt processing was commenced (never concluded), and more effort into development of the salt processing unit operations

and process monitoring begun. Regarding molten salt/molten bismuth reductive extraction, a report from 1972 (very late stage of development, short before the project was canceled) noted (21):

> The continuous interchange of salt between the reactor and processing plant requires quick and reliable analytical techniques for salt composition, uranium and protactinium content, and U(IV)/U(III) ratio. If on-line methods are not developed, laboratory analyses could be used, but these are slow, involve the hazard and expense of sample handling, and require holdup tanks with additional inventory at the sample points. Similarly, on-line monitoring of reductive extraction and metal transfer operations by readings on the salt and/or bismuth phases would allow firm process control; however, we believe that these operations can be properly conducted without sophisticated instrumentation.

It seems like a rapid process monitoring, although clearly recognized as important, was not a priority since the report implies that on-line methods have not been developed yet. The fall back option was the laboratory analysis with all its drawbacks—lag time, labor intensity, and health risks associated with handling irradiated, beryllium containing samples. The report mentions 18 sampling stations throughout the plant to support this option. ORNL therefore didnt have mature on-line process monitoring experience.

Beginning with 1990s, electrochemical methods developed to a point where more laboratories gained interest in performing molten salt electrochemistry for nuclear applications (12, 18). That is where the majority of this work draws from. The theory of CV and its application to uranium and thorium fluoride analysis (including concentration determination) is well documented (22–26). Works in separation of actinides or lanthanides from the salt using electrochemical methods (inert or reactive electrodes—solid or liquid) are also available (17, 27–29).

No reference, however, explores the combined thorium-uranium fluoride system, nor attempts to develop concentration correlations for it. The particular cases of (a) reactor monitoring, and (b) molten salt/molten bismuth thorium/uranium separation process would benefit from having a quick monitoring technique (provided for example by CV). Therefore, this work is considered both relevant (as evidenced by the quoted text from (21)) and novel to the field of molten salt electrochemistry for nuclear applications.

CHAPTER 4

THEORETICAL TREATMENT

In this chapter, the basic theoretical framework of CV is discussed—as well as other related concepts—to support the experimental work reported. A more comprehensive theoretical treatment can be found (e.g.) in (30).

Unless otherwise stated, conditions of planar electrode geometry are considered, as well as diffusion being the only mass transfer component. The assumption of small electrode area vs. sufficiently large solution volume (small A/V conditions) is also held, signifying that the passage of current does not alter the bulk concentrations of species. By "concentration" the salt concentration of the oxidized species is implicitly assumed, since the salt concentration of the reduced form in a soluble-insoluble transition (deposition on cathode) is zero.

4.1 Linear sweep voltammetry

The theory of CV is better explained by starting with closely related, but more straightforward method—linear sweep voltammetry. Here, a potential applied to the working electrode (WE) is varied (swept) at some constant rate. This rate is called a scan rate ν [V s^{-1}] and since it remains constant, a simple relationship between time t [s] and applied potential E [V] can be written:

$$E = E_i - \nu t \tag{4.1}$$

where E_i is the initial potential. Thus, time or potential can be calculated one from another. Plots of current vs. time (I vs. t) and current vs. potential (I vs. E) are identical for scanning in the positive (anodic) direction, and mirrored (symmetrical with respect to y-axis) for scanning in the negative (cathodic) direction. Besides scan rate, one has to specify the initial and the end potential.

4.2 Cyclic voltammetry

In CV, the above mechanism is employed, but rather than stopping the measurement when the end potential is reached, the scanning direction is reversed (switched) and the reverse sweep continues until a specified potential is reached. This can be repeated several times over (hence: cyclic). In addition to the previously mentioned parameters, one has to specify the switching potential(s) E_s and the number of scans (repetitions).

The relationship between time and applied potential is split into two cases. Before reaching E_s Equation 4.1 holds; after reaching E_s the equation is modified:

$$E = E_s + \nu t \tag{4.2}$$

Note that the I vs. E and I vs. t plots are very different now. The first one is a loop of multiple scans placed on top of each other. This can be beneficial in analyzing whether the electrochemical response is stable over several scans (the invariance of position and magnitude of various peaks). The current vs. time plot unfolds those loops into a continuous single curve. This is useful for peak analysis and other data treatment (baseline correction, semidifferentiation, etc.), since now each point on the x-axis has only one assigned value of y-axis, as opposed to the previous case. Plots of I vs. E and I vs. t are depicted in Figure 4.1.

By scanning the potential in this manner, much useful information about the system can be obtained. The reversibility of the reaction has to be determined first.

4.3 Electrochemical reversibility

There are two kinds of reversibility: chemical and electrochemical (which is a practical case of thermodynamic reversibility).

In order for a chemical reaction to be reversible, the products have to be able to react back to form reactants again. If products exit the reaction system or undergo further transformation (or if the activation barrier to reverse the direction is too large), they are no longer able to react back and such reaction is termed irreversible. Chemically reversible reactions are a necessary—but not sufficient—requirement of transient electrochemical techniques like CV.

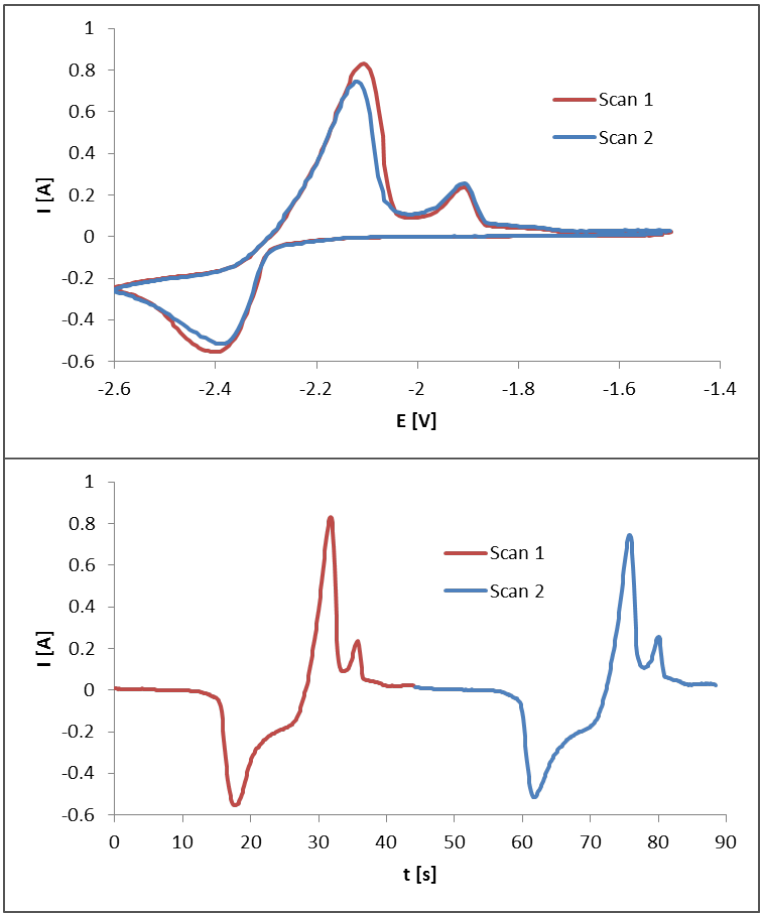

Figure 4.1. Plots of current vs. potential and current vs. time for the same CV run (2.2 wt% $ThCl_4$ in LiCl-KCl).

Electrochemical reversibility assumes processes at the electrode, which are inherently heterogeneous. The reaction kinetics are facilitated by a (heterogeneous) electron transfer. Reversible processes are characterized by fast reaction kinetics relative to mass transfer, while irreversible processes are characterized by slow reaction kinetics. If there is a perturbation (a change in applied potential, most notably), fast reaction kinetics ensure that equilibrium is established rapidly. Irreversible processes do not establish equilibrium rapidly.

In other words, reversible electrode reactions follow thermodynamic laws—particularly Nernst equation—which links the electrode potential with species activity:

$$E = E^0 + \frac{RT}{nF} ln \frac{a_{Ox}}{a_{Red}} \tag{4.3}$$

where E^0 is the standard redox potential of the couple, R [J mol^{-1} K^{-1}] is the universal

gas constant, T [K] is temperature, z is the number of exchanged electrons, F [C mol^{-1}] is Faraday's constant, and a_{Ox} and a_{Red} are activities of the oxidized and reduced species, respectively. For reversible systems, Nernst equation transforms into more convenient form:

$$E = E^{0'} + \frac{RT}{zF} ln \frac{c_{Ox}}{c_{Red}} \tag{4.4}$$

where $E^{0'}$ is the apparent standard redox potential (where activity coefficients are grouped with E^0), and c_{Ox} and c_{Red} are surface concentrations of the oxidized and reduced species, respectively.

It is therefore the electrochemical reversibility that needs to be determined in order to extract useful information about the system. For a redox couple:

$$Ox + ze^- \underset{k_b}{\overset{k_f}{\rightleftarrows}} Red \tag{4.5}$$

the forward (k_f) and the backward (k_b) rate constants are equal at equilibrium. Equilibrium is achieved when the applied potential is equal to the redox potential of the couple (E^0).

Under these circumstances, a single constant—the standard heterogeneous rate constant for the electron transfer k^0 [cm s^{-1}]—can be defined. In order to determine whether k^0 is large or small, a parameter Λ is often used. Λ is a ratio of the heterogeneous reaction rate (electron transfer) and mass transfer rate (31, 32):

$$\Lambda = \frac{k^0}{\sqrt{D_{Ox}^{1-\alpha} D_{Red}^{\alpha} (\frac{zF}{RT}) \nu}} \tag{4.6}$$

where D_{Ox} and D_{Red} [cm^2 s^{-1}] are diffusion coefficients of the oxidized and reduced species, respectively, and α is the transfer coefficient.

Table 4.1 shows the conditions under which a reaction can be considered reversible or irreversible. Conditions falling in between these two extremes are termed *quasi-reversible* (32).

Alternative methods of determining reversibility are also used. One method takes advantage of the fact that in CV the reversibility is manifested by the shift in respective reduction and oxidation peaks. The farther away these peaks are from each other, the less reversible (slower) the reaction kinetics (electron transfer) is.

Table 4.1. Conditions for reversibility using parameter Λ (32).

Reversibility	Λ value
Reversible	> 15
Quasi-reversible	$15 > \Lambda > 10^{-2(1+\alpha)}$
Irreversible	$< 10^{-2(1+\alpha)}$

Another method compares the peak potential (E_p) with the potential at half peak ($E_{p/2}$). Equations for reversible and irreversible case were derived (31, 33–36):

$$\Delta E_p^{rev} = |E_p - E_{p/2}| = \frac{0.774RT}{zF} \tag{4.7}$$

$$\Delta E_p^{ir} = |E_p - E_{p/2}| = \frac{1.857RT}{\alpha zF} \tag{4.8}$$

Yet another method looks at invariance of peak potential (E_p) with scan rate. Here, the solution resistance (R_s) must be known and compensated for, since it can have significant impact on the accuracy of WE potential reading due to ohmic drop, an equivalent of Ohm's law for solutions. Ohmic drop (or uncompensated resistance) signifies that a fraction of the applied potential is traded for overcoming the solution resistance. The magnitude of this fraction depends on current:

$$E = IR_s \tag{4.9}$$

4.4 Concentration determination

The significance of whether the system is reversible or irreversible lies in the equations that can be used to relate peak current to concentration (or diffusion coefficient). If the system is reversible, then Berzins-Delahay (33) equation is applicable for soluble/insoluble reaction:

$$I_p^{rev} = 0.61zFAc(\frac{zF}{RT})^{1/2}\nu^{1/2}D^{1/2} \tag{4.10}$$

where I_p [A] is the cathodic peak current, A [cm^2] is an electrode area, and c [mol cm^{-3}] is an analyte concentration.

Conversely, if the reaction is irreversible, the following equation is applicable (30):

$$I_p^{ir} = 0.496zFAc(\frac{\alpha zF}{RT})^{1/2}\nu^{1/2}D^{1/2} \tag{4.11}$$

Practically, the only difference between these two equations is the leading constant and the transfer coefficient α (which signifies the fraction of the applied potential that promotes the forward reaction). Plotting peak current vs. the square root of scan rate will yield linear plots for both cases. The linearity of i vs. $\sqrt{\nu}$ is therefore not conclusive in determination of reversibility.

In order to properly determine concentration based on CV measurement, one has to first determine the reversibility of the system and then use the appropriate equations. Note that these equation were derived specifically for soluble/insoluble (i.e., reduction to metal) case. A different set of equations would be used for soluble/soluble reaction.

4.5 Diffusion coefficient determination

Besides concentration, the diffusion coefficient (D) is another important parameter of electrochemical theory. It makes sense to first determine D using Equations 4.10 or 4.11 by inserting known (verified) value of concentration (c). This can be repeated for several concentrations to obtain a relationship between D and c. Then, a value of D is selected (perhaps averaged over the range) and now concentration becomes the unknown variable that we ultimately want to determine.

Many researchers publish their diffusion coefficients for particular systems. An alternative approach for concentration determination would therefore be to select representative values from the literature.

4.6 Semidifferentiation

A serious limitation of the CV is its inability to resolve closely positioned peaks. The leading edge of the peak is influenced by the electron transfer kinetics. Fast (reversible) kinetics results in sharp leading edge, while sluggish (irreversible) kinetics results in broader leading edge, potentially obscuring the next peak to appear.

The peak shape is not influence solely by reaction kinetics. After the peak current is reached, mass transfer processes are dominating and the current profile after the

peak is governed by these processes. If diffusion is the limiting factor, then current decays with the inverse of a square root of time, according to Cottrell equation (30, 37):

$$I = zFAc\sqrt{\frac{D}{\pi t}} \tag{4.12}$$

The resulting shape is a characteristic "tail" of the CV peak. In other words, diffusion broadens the peak significantly, making it asymmetrical, with the second half broader than the first half. Thus, if there is another peak in close proximity, deconvolution of the compound signal is necessary and without guaranteed success. Alternatively, multivariate analytical techniques can provide more reliable and accurate correlations (38).

For this reason the semidifferentiation—a very useful treatment of the data—is sometimes used to improve the signal. As the name suggests, the signal from the CV in the form of i vs. t is differentiated with respect to $t^{1/2}$. The resulting plot has much sharper, symmetrical peaks and can therefore distinguish peaks in closer proximity.

Tests for reversibility, as well as charge transfer numbers, kinetic parameters and diffusion coefficients can be obtained from these derived equations (31, 39, 40):

$$W_p^{rev} = \frac{3.53RT}{zF} \tag{4.13}$$

$$W_p^{ir} = \frac{2.94RT}{\alpha zF} \tag{4.14}$$

$$e_p^{rev} = -\frac{z^2F^2A\nu c\sqrt{D}}{4RT} \tag{4.15}$$

$$e_p^{ir} = -\frac{\alpha z^2F^2A\nu c\sqrt{D}}{3.367RT} \tag{4.16}$$

where W_p is the peak width and e_p is the peak height.

CHAPTER 5

EXPERIMENTAL SETUP

This section describes the setup arrangement for fluoride experiments. Experiment scheduling, as well as a note on selection of the solvent, is also included.

5.1 Inert atmosphere glovebox

All electrochemical experiments were performed in an inert argon atmosphere glovebox (Innovative Technologies). The glovebox maintains O_2 and H_2O levels below 2 ppm. This is to avoid reactions with oxygen and water, which lead to oxidation of the salt (24), since all fluoride- and chloride-based chemicals used are extremely hygroscopic. All salt samples were therefore stored in the glovebox as well.

The glovebox is equipped with a heat exchanger connected to a chiller (Polyscience WisperCool) to prevent the glovebox atmosphere from heating up during high temperature experiments. The coolant in the chiller is a 50:50 ethylene glycol:distilled water mixture. Photograph of the glovebox setup is shown in Figure 5.1.

5.2 Furnace

A top loading electric resistance furnace (Kerr Auto Electro-Melt) was used to heat the salt up to 1173 K (900 °C). The interior of the furnace consists of a graphite liner and a point heating element. A 50 mm hole was drilled into the furnace lid to permit the passage of the electrodes. The photograph of the furnace is shown in Figure 5.2.

5.3 Potentiostat

A potentiostat is a device that can manipulate and measure potential or current at an electrode. In this work the Autolab PGSTAT302N (Metrohm) was used, controlled by NOVA software. The potentiostat was placed outside the glovebox, with leads connecting to copper posts at the back of the glovebox. Inside the glovebox, copper

Figure 5.1. Photograph of the inert atmosphere glovebox, potentiostat and chiller setup.

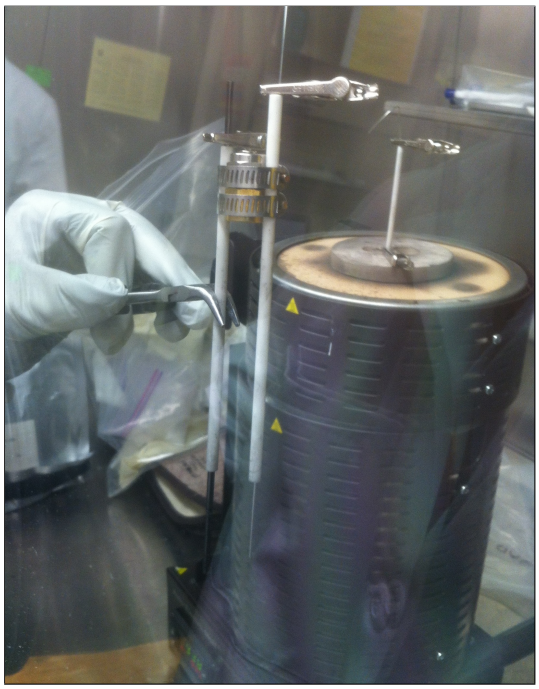

Figure 5.2. Photograph of the electrochemical setup showing the furnace (Kerr Auto Electro-Melt) with alumina lid and the three-electrode setup (WE and CE held together by a nut and a hose clamp, RE sitting independently in the lid).

wires with alligator clips were attached to the corresponding posts to complete the electrical connections.

In the NOVA software, the CV method with scan rates of 0.1–0.3 V s^{-1} was used to gather electrochemical data which was later extensively processed. The chronoamperometry (CA) method was sometimes briefly used for electrochemically cleaning the electrode surface.

5.4 Chemicals

The base salt was LiF (Alfa Aesar, 99.98 %) predried in a glovebox by running one 24 h drying cycle during which the temperature in a furnace was varied between 100, 300 and 600 °C. The analyte salts were ThF_4 (Materion, 99.99 %) and UF_4 (IBI-Labs, 99.8 %). Photographs of solidified ingots of LiF−ThF_4 and LiF−UF_4 are shown in Figure 5.3.

For the reductive extraction experiment, bismuth (Alfa Aesar, 99.99 %, needles) together with lithium (Alfa Aesar, 99 %, chips) were used to make a Bi-Li alloy.

5.5 Electrochemical cell

Nickel (MTI Albany) or glassy carbon (HTW-Germany) crucibles inside the furnace were used to contain fluoride salts. A three-hole alumina customized plug sat on the furnace lid and served as a non-conductive electrode holder. Two larger openings in the alumina plug were further reduced in size by ceramic detachable reductions (plugs) which permitted thin alumina electrode sheaths to be snugly inserted.

A three-electrode setup was employed. The (sheathed) WE and counter electrode (CE) were coupled together at a constant distance (and to remain parallel) by a nut and a hose clamp setup depicted in Figure 5.2. The reference electrode (RE) was sitting in the smallest opening independently.

The temperature of the salt inside the furnace was (occasionally) checked by a K-type thermocouple (precision of ±2 K).

The WE was a 1 mm diameter molybdenum wire (Alfa Aesar, 99.94 %). The RE was a 0.5 mm diameter platinum wire (Alfa Aesar, 99.95 %)—a quasi-reference electrode based on a $Pt/PtO_x/O^{2-}$ couple (41). The CE was a 3 mm diameter glassy

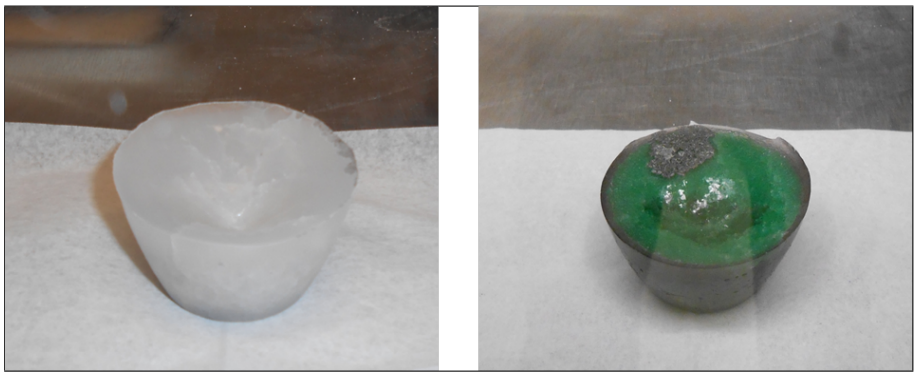

Figure 5.3. Photograph of salt ingots of $LiF-ThF_4$ (left) and $LiF-UF_4$ (right).

carbon rod (Alfa Aesar), providing sufficient surface area.

5.6 Salt analysis

Analyte concentration from samples was determined using inductively-coupled plasma atomic emission spectroscopy (ICP-AES) or mass-spectroscopy (ICP-MS). The photograph of the ICP-AES machine (Spectro Genesis FES) is shown in Figure 5.4.

The salt was sampled while molten using an alumina tube. The solidified sample was then shaken off the tube, crushed in a mortar and pestle, weighed and dissolved overnight in 60 mL of conc. HCl, together with a 4 mL H_3BO_3 addition to compensate the free fluoride content.

The solution was visually inspected to confirm complete dissolution of salt and 4 mL were pipetted to a 15 mL sample tube together with 11 mL of diluted HNO_3 to match the matrix of ICP-AES standards (Inorganic Ventures).

The standards were treated in the same way—a small volume of conc. HCl was inserted into them to match the sample matrix. All samples and standards therefore had the same composition and total volume (15 mL): 11 mL HNO_3 (7 vol%) + 4 mL HCl (35 vol%).

5.7 Selection of base salt

Ideally, the solvent is identical to the one used in actual MSR: $LiF-BeF_2$. However, using BeF_2 presents significant industrial hygiene challenges that we chose

Figure 5.4. Photograph of the ICP-AES machine (Spectro Genesis FES) used for salt sample analysis.

to avoid until later stages of investigation and technology development. Studies published on this topic usually selected $LiF-CaF_2$ eutectic and focused either on uranium (22, 23, 25, 26) or thorium (17, 24) exclusively.

However, calcium—along with other elements commonly encountered in fluorides like potassium (KF) or sodium (NaF)—has a high thermal neutron absorption cross section, rendering it unsuitable for use in the reactor salt, or even in the blanket salt/bismuth contactor unit (4).

This nuclear constraint practically disqualifies all other fluorides except a few with very low thermal neutron cross sections (^{7}Li, ^{11}B, Be, perhaps Mg). The use of $LiF-BF_3$ is not possible since BF_3 is a gas. Thus, we selected lithium fluoride alone as the closest surrogate solvent. Two disparities need to be remembered, however.

First, the high melting point of LiF alone (1123 K, 850 °C) would make it impractical for use in the MSR without other salt(s) to lower the melting point. The ease of working with a single-component, non-toxic system is believed to be worth the disadvantage of salt's higher melting point.

Second, the omission of BeF_2 results in a broader electrochemical window (the cathodic limit is given by more cathodic reduction of lithium, instead of the more noble beryllium). For our goal—the concentration monitoring of both thorium and uranium—LiF is a suitable solvent. In the $LiF-BeF_2$ system such monitoring of thorium would not be possible due to similar reduction potentials of Be and Th.

5.8 Experiment scheduling

5.8.1 Electrochemical experiments

Initially, the validity of the electrochemical setup had to be verified by replicating a previously published electrochemical experiment. This was accomplished by replicating the work of Saila (42), where DyF_3 was analyzed in $LiF-CaF_2$ media. Satisfactory agreement between the published value for the diffusion coefficient and the one obtained in the experiment was reached.

The effect of moisture (24) was fully experienced in this test run, manifesting itself with drastically lower electrochemical signal of dysprosium than expected. This effect is described in more detail in Section 6.1.

After the setup was validated, experiments with thorium-only and uranium-only analytes were scheduled, with the ultimate goal of obtaining the relationship between peak current and analyte concentration (i.e,. a calibration curve).

When calibration curves for the two analytes were generated, both thorium and uranium were mixed in a single salt, producing a ternary system. The assumption that relatively high concentrations in a multianalyte system could be reliably estimated based on single analyte calibration curves was experimentally tested.

5.8.2 Salt/bismuth extraction

For salt/bismuth extraction experiments, the metal ingot and the salt ingot were prepared separately before being combined together and melted.

For the metal Bi-Li alloy, Bi needles were melted in a crucible and an ingot was produced. Then the ingot was remelted and Li chips were added. Sufficient time was allowed for Li to dissolve in Bi. Then the furnace was shut down to obtain solid Bi-Li ingot.

The salt ingot of desired composition was prepared by combining the base salt with analyte, while realizing a CV measurement to determine analyte concentration.

Finally, the two ingots were combined together in a single crucible and melted. Electrodes were inserted into the salt section (top) as soon as the salt melted, in an attempt to capture the most of the extraction. Simultaneously, periodic sampling of the salt was done for ICP-AES concentration analysis.

A photograph of the two distinct phases fused in a single ingot is shown in Figure 5.5. It is noted that once both phases were contained in a crucible, there was a considerable chance that the crucible will crack upon cooling or upon the next heating.

The reason is the anomalous behavior of bismuth, which expands upon solidification (water also exhibits this anomaly). In a crucible where bismuth is the only phase, this is facilitated by mere upward expansion. However, if there is a (frozen) layer of salt on top of the bismuth during cooling, bismuth is forced to expand sideways, stressing (and potentially cracking) the crucible walls.

Figure 5.5. Photograph of the LiF−ThF_4/Bi-Li ingot. Note the salt color difference when compared with Figure 5.3.

CHAPTER 6

RESULTS AND DISCUSSION

6.1 Analyte Concentrations

Expected and *measured* analyte concentrations are distinguished here. The *expected concentration* is simply the prediction based on weighed amounts of added salts, whereas the *measured concentration* is determined by sampling the salt after the experiment and analyzing by ICP-AES (or ICP-MS).

The measured concentration is almost always lower than the expected. Particularly for the first addition of analyte, the difference is appreciable. One factor behind this discrepancy, as explained in (24), may stem from the reaction of thorium fluoride with residual moisture in the salt. Two-step precipitation with an intermediate product ($ThOF_2$) is likely encountered (ΔG_f values obtained from (43)):

$$ThF_4 + O^{2-} \rightleftarrows ThOF_2 + 2F^- \qquad \Delta G_f(1173\text{ K}) = \text{-}6.8\ [\text{kJ (mol ThF}_4)^{-1}] \quad (6.1)$$

$$ThOF_2 + O^{2-} \rightleftarrows ThO_2 + 2F^- \qquad \Delta G_f(1173\text{ K}) = \text{-}4.1\ [\text{kJ (mol ThOF}_2)^{-1}] \quad (6.2)$$

The final product (ThO_2) precipitates out of solution and becomes electrochemically inactive. A visual inspection of solidified salt indeed revealed areas of white precipitate, similar to in (24).

For this reason, the electrochemically active portion of ThF_4 will always be somewhat lower than the expected amount, and the magnitude of this transformation strongly depends on the residual moisture content. When plotting results, both expected and measured thorium concentration are included for comparison.

A similar discrepancy was observed for UF_4 additions (measured concentrations were lower than expected ones), with the proposed mechanism (ΔG_f values obtained from (43)):

$$UF_4 + O^{2-} \rightleftarrows UOF_2 + 2F^- \qquad \Delta G_f(1173\text{ K}) = \text{-}37.1\ [\text{kJ (mol UF}_4)^{-1}] \qquad (6.3)$$

$$UOF_2 + O^{2-} \rightleftarrows UO_2 + 2F^- \qquad \Delta G_f(1173\text{ K}) = \text{-}26.1\ [\text{kJ (mol UOF}_2)^{-1}] \qquad (6.4)$$

Again, plots for both expected and measured uranium concentrations are included in the results. A summary of expected and measured concentrations for both analytes is listed in Table 6.1.

6.2 Thorium

6.2.1 Thorium reduction mechanism

CVs were obtained for expected ThF_4 concentrations ranging from 1.23 to 5.45 wt% ThF_4 (0.92 to 4.11 wt% Th), and one example is presented in Figure 6.1.

One cathodic peak corresponding to [Th(IV)/Th] reduction is observed, followed by two anodic peaks. From careful observation, the reduction peak, as well as the first anodic peak, are actually composed of two peaks. A clearer picture of the reduction peak(s) is given by semidifferentiating the CV—the matter is further discussed in the next section.

The presence of the second anodic peak can be explained by several possibilities. It is either (a) a manifestation of oxide contamination (similar peak was observed (24) after deliberate addition of CaO), (b) incomplete stripping of Th, or (c) the result of oxygen desorption. For the purpose of on-line monitoring as well as for reductive extraction, however, only the [Th(IV)/Th] cathodic peak is of importance. Thus, no detailed analysis of the anodic behavior was performed.

6.2.2 Thorium rate control criteria

As discussed in Section 4.3, fundamental characteristics of the redox reaction at an electrode surface are needed for determining the appropriate equations to relate concentration to measured peak current. In particular, whether the reaction is diffusion limited and whether it is reversible or irreversible dictates which equations can be used to calculate concentration.

Verification of the reduction process being controlled by the diffusion of analyte ions is done by plotting the peak current density vs. a square root of scan rate. The points follow a linear trend if the electrochemical reduction is diffusion limited.

Table 6.1. Expected and measured concentrations of Th (added as ThF_4) and U (added as UF_4).

Conc. [wt%]	Mixture T1	Mixture T2	Mixture T3	Mixture T4	Mixture T5
Th expected	0.92	1.84	2.68	3.29	4.11
Th measured	0.60±0.06	1.44±0.19	2.39±0.40	2.98±0.49	3.94±0.71
	Mixture U1	Mixture U2	Mixture U3	Mixture U4	Mixture U5
U expected	0.74	1.53	2.27	2.96	3.67
U measured	0.51±0.12	1.56±0.19	1.93±0.21	2.32±0.02	3.14±0.29

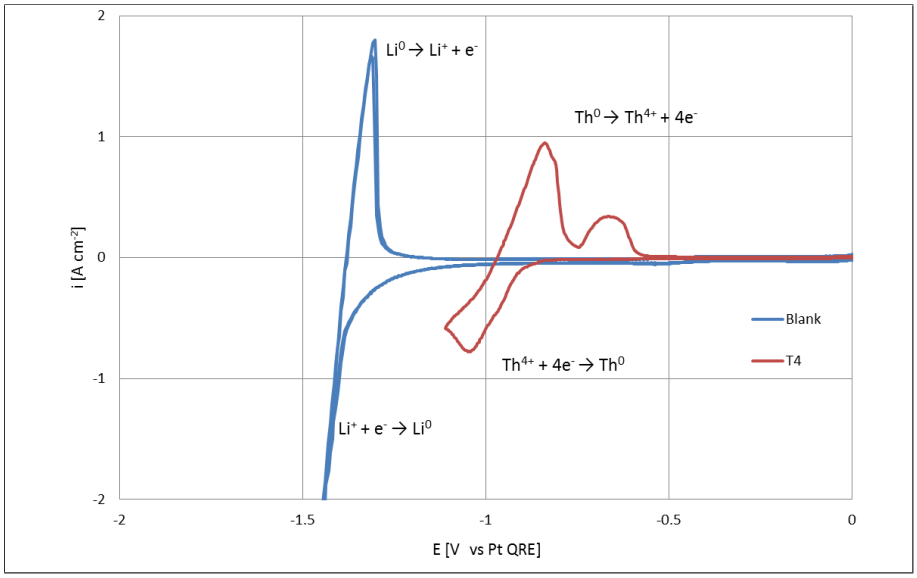

Figure 6.1. CVs of LiF (Blank) and LiF−ThF_4. $A = 0.2$ cm^2, $T = 1173$ K, $\nu = 200$ mV s^{-1}, $c(ThF_4) = 4.37$ wt%. WE: Mo, CE: glassy carbon, RE: Pt.

The plot of cathodic peak current density (with reversed sign to maintain positive values—for convenience) vs. square root of scan rate for ThF_4 over the range of concentrations investigated is shown in Figure 6.2.

The lowest three scan rates were used to produce a trend line, which was extrapolated to higher scan rates. The plot of concentration T1 shows agreement over the full range of scan rates. The plots of T2 and T3 still show some agreement, whereas the plots of T4 and T5 are starting to deviate at higher scan rates (T5 appreciably). It is concluded that the process is diffusion limited at lower scan rates (the breaking

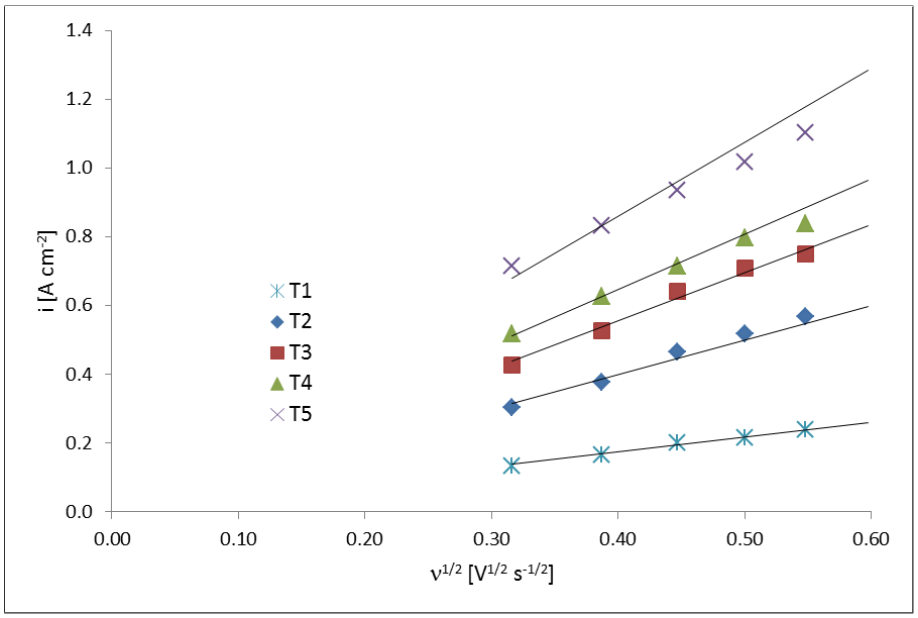

Figure 6.2. Linear relationship of Th(IV) reduction peak current density vs. the square root of scan rate. $A = 0.2$ cm^2, $T = 1173$ K, $\nu = 100$–300 mV s^{-1}. WE: Mo, CE: glassy carbon, RE: Pt. Concentrations T1–T5 are defined in Table 6.1.

point seems to lie around 0.25 V s^{-1}). Consequently, all concentration measurements were done at 0.2 V s^{-1} to stay in the diffusion-limited regime.

A reason for suboptimal results for higher concentrations in Figure 6.2 is explained by more detailed analysis of the reduction peak. By semidifferentiating the CV (as discussed in Section 4.6), a plot of convoluted current vs. time is obtained—see Figure 6.3. At higher concentrations (3 wt% ThF_4 and higher), a second peak becomes apparent in the immediate vicinity of ThF_4 reduction, which is attributed to the reduction of $ThOF_2$ (24). The reduction of $ThOF_2$ is hypothesized to happen according to the following scheme:

$$ThOF_2 \rightleftarrows ThO^{2+} + 2F^- \tag{6.5}$$

$$ThO^{2+} + 4e^- \rightleftarrows Th + O^{2-} \tag{6.6}$$

This introduces error into peak current density calculation which manifests itself in Figure 6.2. However, the objective is to measure (total) thorium concentration, not just the [Th(IV)/Th] couple. Both compounds are thorium species, and it can be argued that since the currents are additive, the total peak encompasses both

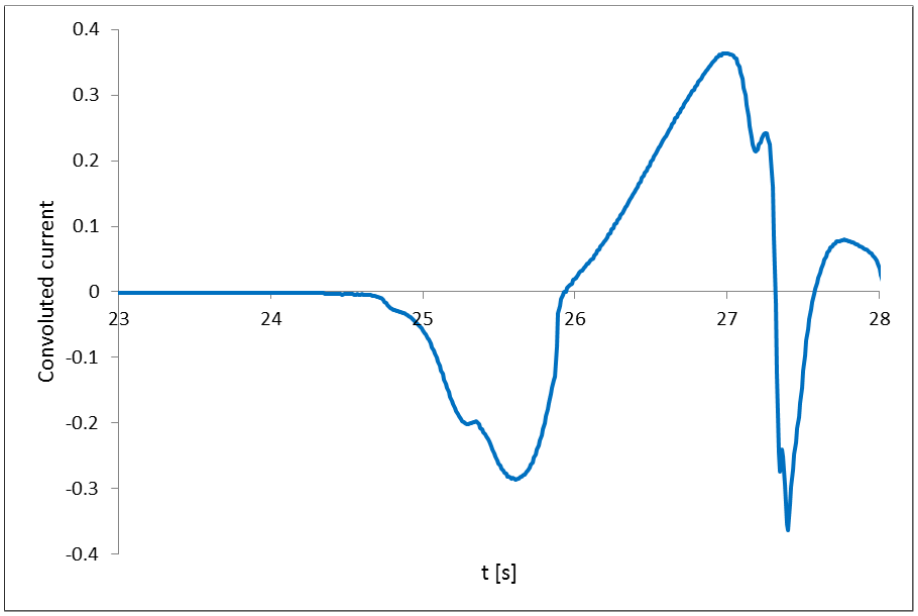

Figure 6.3. Semidifferentiated plot of CV of LiF−ThF_4. $A = 0.2$ cm^2, $T = 1173$ K, $\nu = 250$ mV s^{-1}, $c(ThF_4) = 5.45$ wt%. WE: Mo, CE: glassy carbon, RE: Pt. Plot shows the reduction peak (at $t = 25$–26 s) being composed of two components.

species. No prominent peaks are visible at lower ThF_4 concentrations, explaining good agreement in Figure 6.2.

6.2.3 Thorium reversibility criteria

One test for the reversibility of the reaction is the calculation of difference between peak (E_p) and half-peak ($E_{p/2}$) potential. This method cannot be reliably used here because the reduction peak is actually composed of two peaks (as mentioned above) and the answer would yield inconsistent results, conflicting previous studies which identified reversible behavior (24, 44).

Another test for reversibility is the independence of the cathodic peak potential relative to square root of scan rate. However, the solution resistance must be known and compensated for to accurately compare potentials at different scan rates (as discussed in Section 4.3). Also, the reference electrode must be extremely stable.

Since the solution resistance was not measured and the Pt quasi-reference electrode can become polarized, only a limited conclusion can be drawn from this analysis. The peak potential was plotted vs. square root of scan rate in Figure 6.4.

Similarly to Figure 6.2, the lowest three scan rates were used to produce a trend

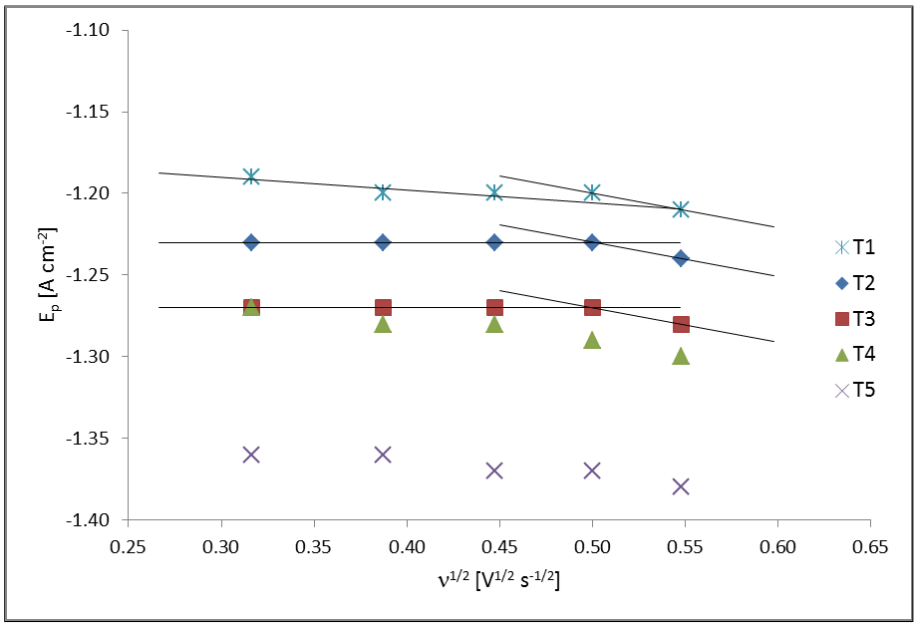

Figure 6.4. Th(IV) reduction peak potential vs. the square root of scan rate. $A = 0.2$ cm^2, $T = 1173$ K, $\nu = 100$–300 mV s^{-1}. WE: Mo, CE: glassy carbon, RE: Pt. Concentrations T1–T5 are defined in Table 6.1.

line, which was extrapolated to higher scan rates. At lower concentrations, these trend lines appear to describe reversible behavior up until 0.25 V s^{-1}. The fastest scan (0.3 V s^{-1}) is clearly off in all cases and marks the onset of quasi-reversible behavior. At higher concentrations no clear cut-off is seen, again due to uncompensated ohmic drop, uncertainty of peak potential vs. reference and also due to the appearance of second reduction peak mentioned previously.

A tentative conclusion can be drawn: below 0.25 V s^{-1} the system is regarded as reversible with limited validity at higher concentrations.

The significance of whether the system is reversible or irreversible lies in the selection of equations for relating peak current density to concentration and diffusion coefficient. In our case, concentration measurements were done at scan rates of 0.2 V s^{-1}, therefore, Equation 4.10 was used.

6.2.4 Thorium diffusion coefficient calculations

Given that the [Th(IV)/Th] reduction appears to be reversible, Equation 4.10 was combined with the slopes from Figure 6.2 to calculate the diffusion coefficient of

Th(IV) in molten LiF at 1173 K, for each concentration (T1–T5).

The resulting diffusion coefficients are plotted in Figure 6.5 for the two sets of concentrations—expected and measured. The plot based on expected concentrations indicates essentially constant diffusion coefficient over the examined concentration range. The plot based on measured concentrations indicates a slight decrease in diffusion coefficient with increasing concentration.

This illustrates the importance of salt sampling and subsequent analysis—a fraction of the added analyte is apparently consumed in the reaction with residual moisture (as discussed in Section 6.1), and so the expected concentrations gives misleading results like this one.

The diffusion coefficients averaged over the entire concentration range were:

D = 1.8 $\pm$0.2 $\times$ 10^{-5} cm^2 s^{-1} (for expected concentrations)

D = 2.8 $\pm$0.9 $\times$ 10^{-5} cm^2 s^{-1} (for measured concentrations)

These results are somewhat lower than the published (24) value of 5.0 $\pm$0.1 $\times$ 10^{-5} cm^2 s^{-1} (similar salt LiF$-$$CaF_2$$-$$ThF_4$($\approx$1 wt%) at 1113 K). When looking at the intercept value for measured concentration dataset, 4.2 $\times$ 10^{-5} cm^2 s^{-1} emerges as a diffusion coefficient at infinite dilution.

6.2.5 Thorium concentration calibration curve

To obtain a calibration curve of concentration vs. cathodic peak current from which unknown amounts of analyte can be estimated, it is more convenient to use peak current density (i.e., peak current divided by the surface area of the electrode) instead of a peak current.

The electrode area is related to the immersion depth, which was measured with an accuracy of $\pm$1 mm. Admittedly, this does limit the accuracy of measurements, particularly that of diffusion coefficients. It is still useful for the purpose of quick (real-time) estimation of analyte concentration, which is the objective.

The current is a function of c, and ν—both of which can be independently varied. A calibration curve that relates concentration to current density must specify a scan rate. In this case it is 0.2 V s^{-1}. Figure 6.6 shows peak current density plotted vs. thorium concentration (linear regression with zero intercept was applied).

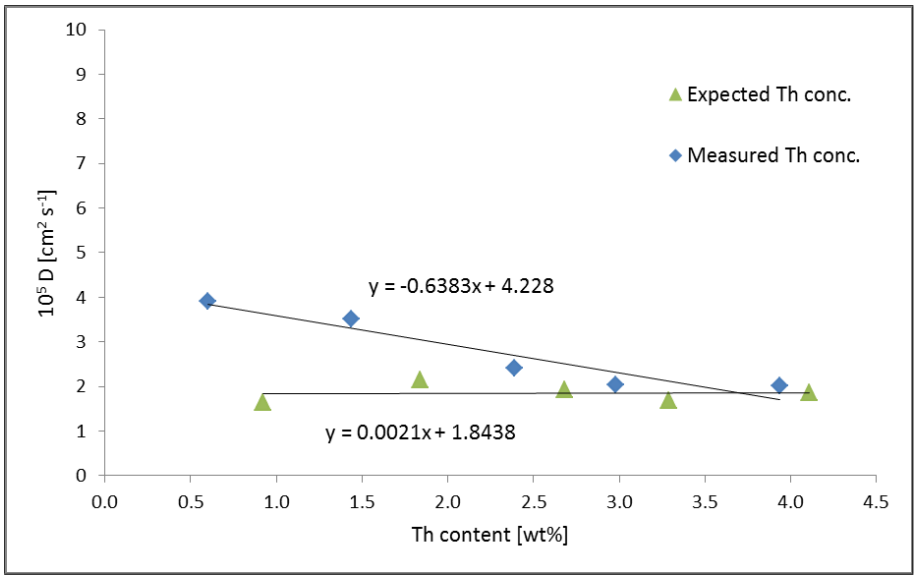

Figure 6.5. Diffusion coefficient of Th(IV) vs. expected and measured concentrations. $T = 1173$ K.

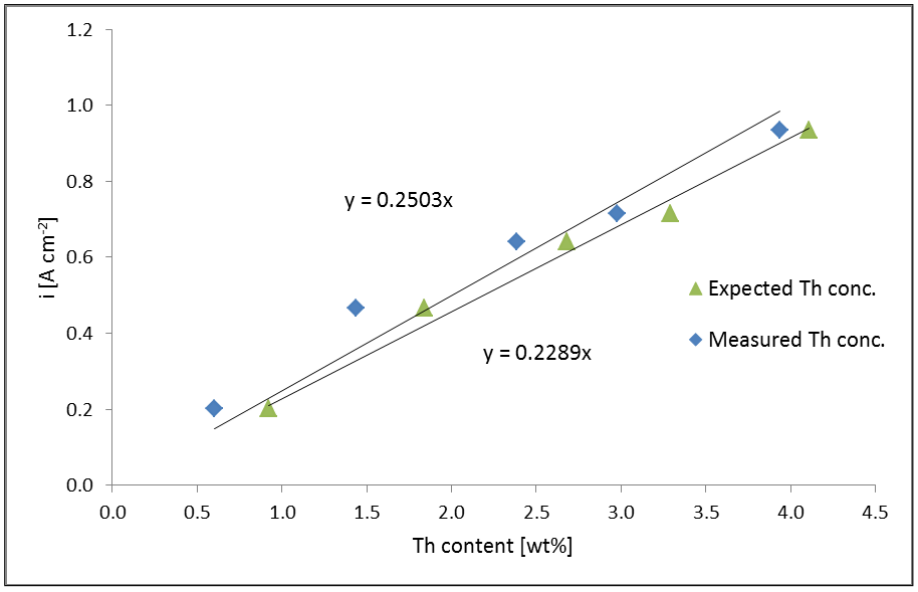

Figure 6.6. Th(IV) reduction peak current density vs. expected and measured concentrations. $T = 1173$ K, $\nu = 200$ mV s^{-1}.

The calibration curve is satisfactory, albeit far from perfect, mainly due to relatively inaccurate surface area determination. Interestingly, large differences seen in the lower concentration range (first three additions) for the expected and measured concentrations introduced only relatively minor errors (< 0.2 wt%). The higher concentration range is affected more severely.

Another phenomenon might be influencing the accuracy at the higher end of the concentration range. A negative departure from linearity was consistently observed at higher concentration for uranium in chlorides (38, 45). The most plausible explanation revolves around a mixed-kinetics (quasi-reversibility) regime, where the electron transfer kinetics cannot be completely neglected.

It is inconclusive whether an onset of this effect can be observed in Figure 6.6, the concentration range would need to expand further (perhaps to 10 wt%).

6.3 Uranium

6.3.1 Uranium reduction mechanism

CVs were obtained for expected UF_4 concentrations of 0.97 to 4.84 wt% UF4 (0.74 to 3.67 wt% U), and one example is presented in Figure 6.7.

Three cathodic peaks were observed. According to literature (22, 23, 25, 26), the first (most positive) one was identified to correspond to [U(IV)/U(III)] soluble/soluble reduction. The second, sharp peak is unknown and not described in the literature for this system. A loose shard of alumina sheath is suspected to have fallen into the salt and contaminated it with substantial quantity of aluminum ions.

This claim is supported by the reduction potential order: $E_{[U(III)/U]} < E_{[Al(III)/Al]} < E_{[U(IV)/U(III)]}$ compiled from two publications (23, 28). The possibility of appreciable aluminum ion introduction via alumina sampling tube is highly unlikely due to very short contact times (insertion took less than a second, the salt solidified in less than 5 s after withdrawal) vs. the magnitude of the aluminum peak observed. The third peak corresponds to [U(III)/U] reduction.

In the anodic run, several peaks were observed. According to the same literature mentioned in the previous paragraph, the first (most negative) stripping peak corresponds to the dissolution of solid uranium deposited during the cathodic run. Then

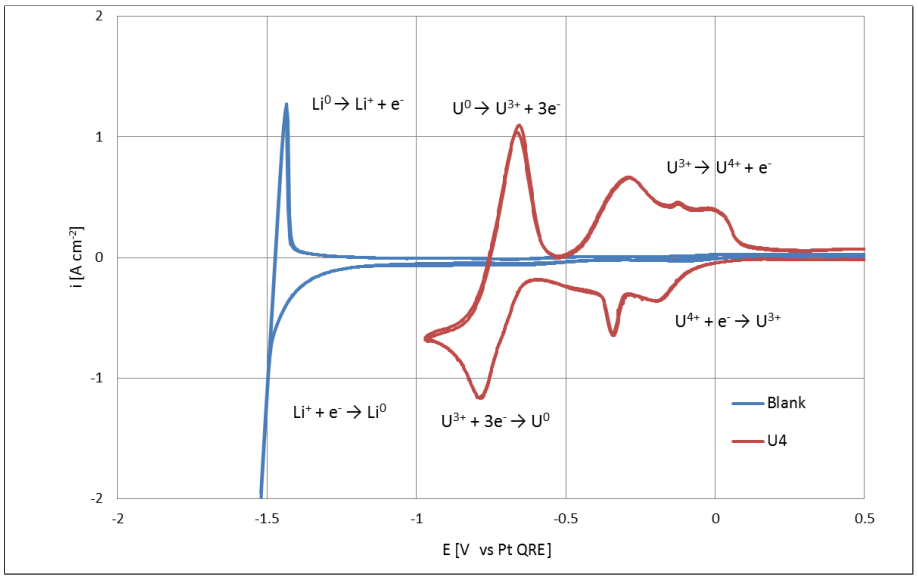

Figure 6.7. CVs of LiF (Blank) and LiF−UF_4. $A = 0.22$ cm^2, $T = 1173$ K, $\nu = 200$ mV s^{-1}, $c(UF_4) = 4.37$ wt%. WE: Mo, CE: glassy carbon, RE: Pt.

a continuum of several peaks is presumed to be a combination of [U(III)/U(IV)] oxidation peak (which is of rather broad shape) and the oxide (and aluminum) contamination discussed earlier. For the purpose of on-line monitoring as well as for reductive extraction, again only the [U(III)/U] cathodic peak is of importance.

6.3.2 Uranium rate control criteria

Verification of the [U(III)/U] reduction process being controlled by the diffusion of analyte ions was done by plotting the cathodic peak current density (with reversed sign to maintain positive values) vs. square root of scan rate in Figure 6.8.

In comparison to the thorium case, the whole scan range (0.1–0.3 V s^{-1}) now appears to follow the linear trend line set by the lowest three scan rates. This is in agreement with a previous study (23), which concluded diffusion control up to 0.5 V s^{-1}. Moreover, the trend is followed over the whole concentration range investigated.

6.3.3 Uranium reversibility criteria

A difference in peak (E_p) and half-peak ($E_{p/2}$) potential was used to determine reversibility. Neither reversible nor irreversible behavior could be reliably obtained. Furthermore, a difference in potential between the first [U(IV)/U(III)] and second

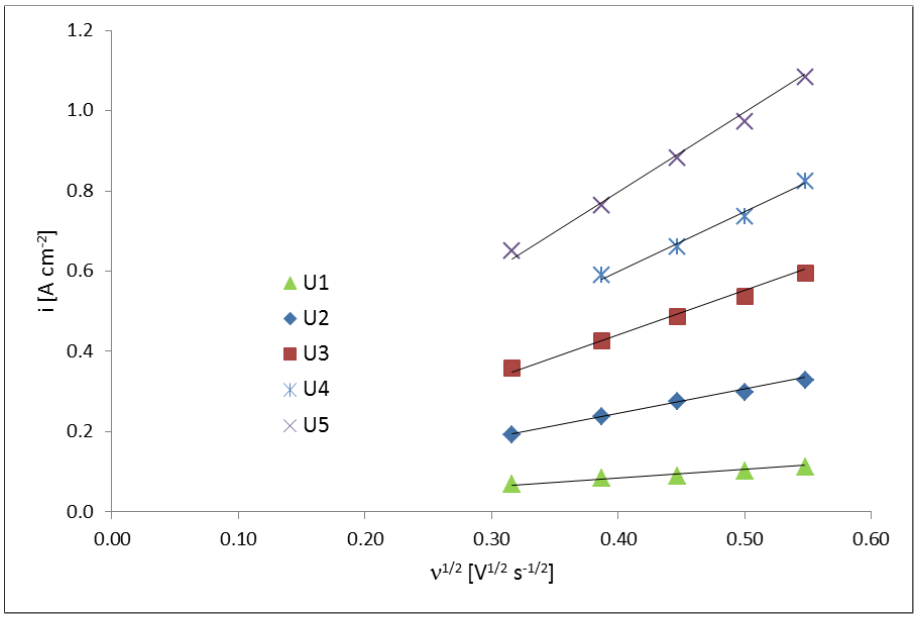

Figure 6.8. Linear relationship of U(III) reduction peak current density vs. the square root of scan rate. $A = 0.22$ cm^2, $T = 1173$ K, $\nu = 100$–300 mV s^{-1}. WE: Mo, CE: glassy carbon, RE: Pt. Concentrations U1–U5 are defined in Table 6.1.

[U(III)/U] redox couple was reported (23) to be 0.75 V, but in this work it was observed to be only 0.65 V (second redox couple appeared at less cathodic potential). Finally, uranium-molybdenum phase diagram (46) was inspected and a possible alloy formation was identified at 773 K in the molybdenum-rich region.

These three findings lead to the conclusion that the [U(III)/U] reduction peak is actually an alloy formation peak, the consequence of which is discussed later.

The peak potential was plotted vs. scan rate to determine reversibility, albeit difficulties with this analysis as outlined earlier (solution resistance contributes to the potential shift as scan rate is increased, and Pt quasi-reference electrode is not exceptionally stable).

For these reasons a slight drop in potentials was expected instead of true independence vs. scan rate. Figure 6.9 shows this slight drop (U4 shows true independence). Since the slope of the drop does not suddenly change around higher scan rates (as was the case with thorium—Figure 6.4) leads to conclusion that the system is reversible, a finding that is in agreement with similar works (22, 23).

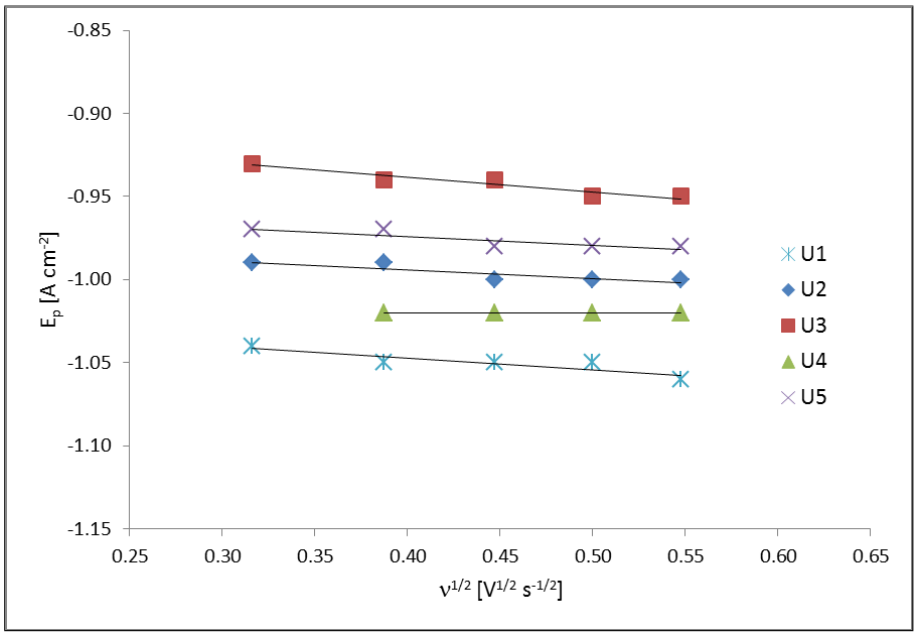

Figure 6.9. U(III) reduction peak potential vs. the square root of scan rate. $A = 0.22$ cm^2, $T = 1173$ K, $\nu = 100$–300 mV s^{-1}. WE: Mo, CE: glassy carbon, RE: Pt. Concentrations U1–U5 are defined in Table 6.1.

6.3.4 Uranium diffusion coefficient calculations

The [U(III)/U] reduction was determined to be reversible. Consequently, Equation 4.10 was combined with the slopes from Figure 6.8 to calculate the diffusion coefficient of U(III) in molten LiF at 1173 K for each concentration (U1–U5).

The resulting diffusion coefficients are plotted in Figure 6.10 for the two sets of concentrations—expected and measured. Both plots indicate a slight increase in diffusion coefficient with increasing concentration. The reduction peak of interest being actually an alloying peak has negative influence on the accuracy of this calculation.

The diffusion coefficients averaged over the entire concentration range were:

D = 3.4 $\pm$1.3 $\times$ 10^{-5} cm^2 s^{-1} (for expected concentrations)

D = 5.0 $\pm$1.8 $\times$ 10^{-5} cm^2 s^{-1} (for measured concentrations)

These averaged results are somewhat higher than the published values (23, 25) of 2.4 $\pm$0.1 $\times$ 10^{-5} cm^2 s^{-1} and 2.2 $\pm$0.7 $\times$ 10^{-5} cm^2 s^{-1} for LiF$-$CaF$_2-$UF$_4$($\approx$1 wt%), albeit at 1083 K. The temperature difference needs to be taken into account. When looking at the intercept value for measured concentration dataset, 2.3 $\times$ 10^{-5} cm^2 s^{-1} emerges as a diffusion coefficient at infinite dilution.

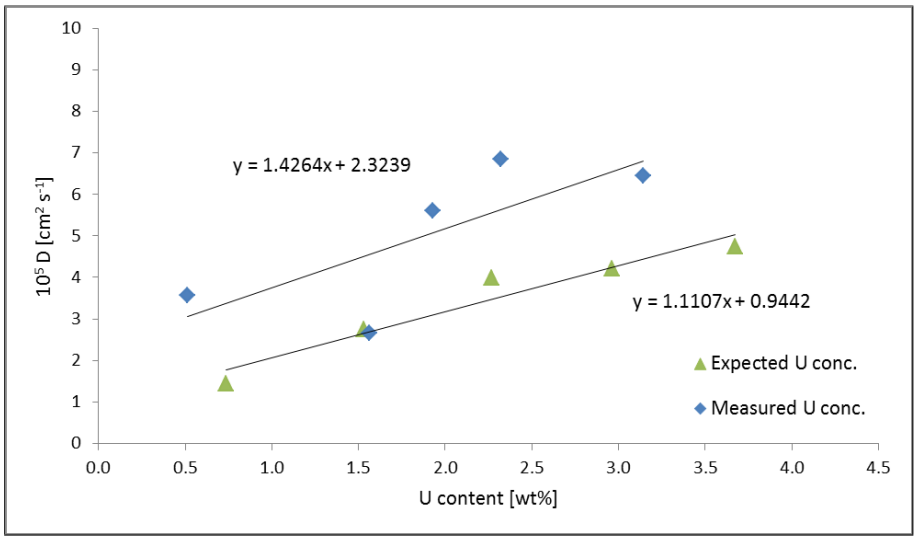

Figure 6.10. Diffusion coefficient of U(III) vs. expected and measured concentrations. $T = 1173$ K.

6.3.5 Uranium concentration calibration curve

As done previously with thorium, a plot of cathodic peak current density vs. analyte concentration (expected or measured) was used to develop a concentration calibration curve. Results for the case of 0.2 V s^{-1} are presented in Figure 6.11.

An important limitation needs to be mentioned here: since the [U(III)/U] peak was identified as corresponding to uranium-molybdenum alloy formation, this calibration curve is only applicable to molybdenum electrode.

The calibration is less satisfactory than for thorium (see Figure 6.6), particularly the second data point (U2) is off. Unlike thorium case, there is a large difference between the curves developed for expected and measured concentrations—the curve for expected concentration does not give very accurate results even in the lower range of concentrations.

6.4 Thorium and uranium system

6.4.1 Reactor monitoring

After calibration curves were obtained for thorium and uranium alone, these two analytes were combined in a ternary salt of the following composition:

$LiF-ThF_4-UF_4$ (91.7–5.4–2.9 wt%)

The parameters of the experiment are summarized in Table 6.2, along with the

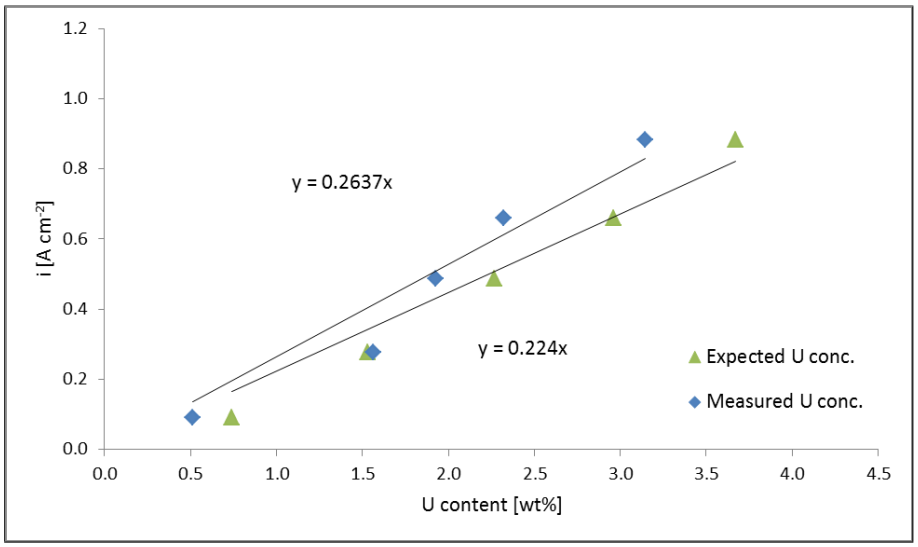

Figure 6.11. U(III) reduction peak current density vs. expected and measured concentrations. $T = 1173$ K, $\nu = 200$ mV s^{-1}.

Table 6.2. Expected, measured and resulting concentrations of Th (added as ThF_4) and U (added as UF_4) in a ternary salt.

Conc. [wt%]	Mixture U+Th	Calibration curve result
Th expected	4.06	5.51
Th measured	3.52±0.02	5.03
U expected	2.17	1.79
U measured	1.48±0.02	1.52

results discussed below. As can be seen from Table 6.2, substantial fractions of both thorium and uranium were again unaccounted between initial addition and sampling after the experiment run.

A CV of the mixture is depicted in Figure 6.12. The two distinctive cathodic peaks correspond to the expected [U(III)/U] and [Th(IV)/Th] reduction steps. The peak separation suggests a possibility of a single element (uranium) extraction without significant coextraction of the other (thorium).

Net peak heights (baseline subtracted) were then entered into the respective equations of calibration curves developed earlier and (approximate) resulting con-

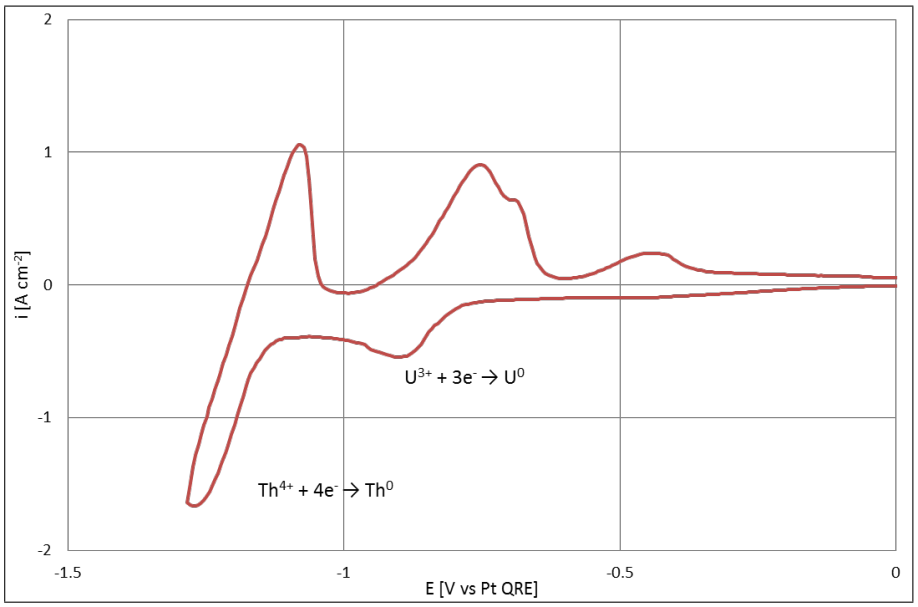

Figure 6.12. CVs of LiF−ThF_4−UF_4. $A = 0.22$ cm^2, $T = 1173$ K, $\nu = 200$ mV s^{-1}, $c(ThF_4) = 5.4$ wt%, $c(UF_4) = 2.9$ wt%. WE: Mo, CE: glassy carbon, RE: Pt.

centrations were calculated (see Table 6.2).

The results show that the method is not straightforward, and care must be taken when interpreting the results. Generally, the first species reducing on a cathode (uranium in this case) can give satisfactory information about the concentration (±0.1 wt%). The last row of Table 6.2 shows that the measured (ICP-AES) uranium content is very close to the electrochemically determined one.

On the other hand, any species that is subsequently reduced (thorium in this case) produces much larger current response which does not correspond directly to its concentration (the first species continues to be reduced). The concentration in this case would be unrealistically exaggerated—there is no real possibility how thorium content could be appreciably larger than expected.

This overestimation might stem from the fact that the surface area of the electrode is appreciably altered by the first species deposition and so the area term in the equation is no longer correct (the area term is underestimated, which in turn gives an overestimated concentration value, as these two are inversely proportional (see Equations 4.10 or 4.11).

Since there is no definite way to account for the changed surface area, the concen-

tration measurements of the subsequently reduced species are discarded as misleading (until a reliable method accounting for the change in surface area is developed). As mentioned earlier, in $LiF-BeF_2-ThF_4-UF_4$ (salt mixture of interest) the determination of thorium content would not be possible at all, due to close proximity of thorium and beryllium reduction potentials.

6.5 Extraction process monitoring

6.5.1 Thorium extraction

After reactor monitoring was successfully demonstrated—at least for uranium—a more challenging two-phase environment of the reductive extraction unit operation was attempted. A single-analyte binary salt ($LiF-ThF_4$) was selected for initial experiments. Thorium was selected first, since its distribution coefficient is lower than the one for uranium, and its extraction into bismuth is detrimental. Therefore, an estimate was sought of how much thorium would extract in the event that all uranium was already extracted from the salt but the extraction process was for some reason not stopped.

An experiment was realized where a crucible containing a bismuth-lithium alloy was in contact with $LiF-ThF_4$ salt. The solid ingot from this experiment is shown in Figure 5.5, the process is described in detail in Section 5.8.2.

The progress of the extraction was monitored by CV and by periodic sampling of the salt. Concentration in bismuth was calculated by mass balance. Noisy erratic readings of the current was obtained by CV, likely due to bismuth particle entrainment in the salt.

Figure 6.13 displays this noisy data. Blue curve shows the original CV data from the salt-only run during ingot preparation (several days prior the extraction experiment), featuring a single reduction peak. Red curve shows how the CV looked like at the beginning of the extraction monitoring, green curve shows a CV taken approximately 40 min after the beginning of extraction monitoring, and purple curve is a CV taken approximately 100 min after the beginning of extraction monitoring.

Closer examination of these plots reveals that a second reduction peak was established, one that was not seen in the original (blue) CV. The explanation for this

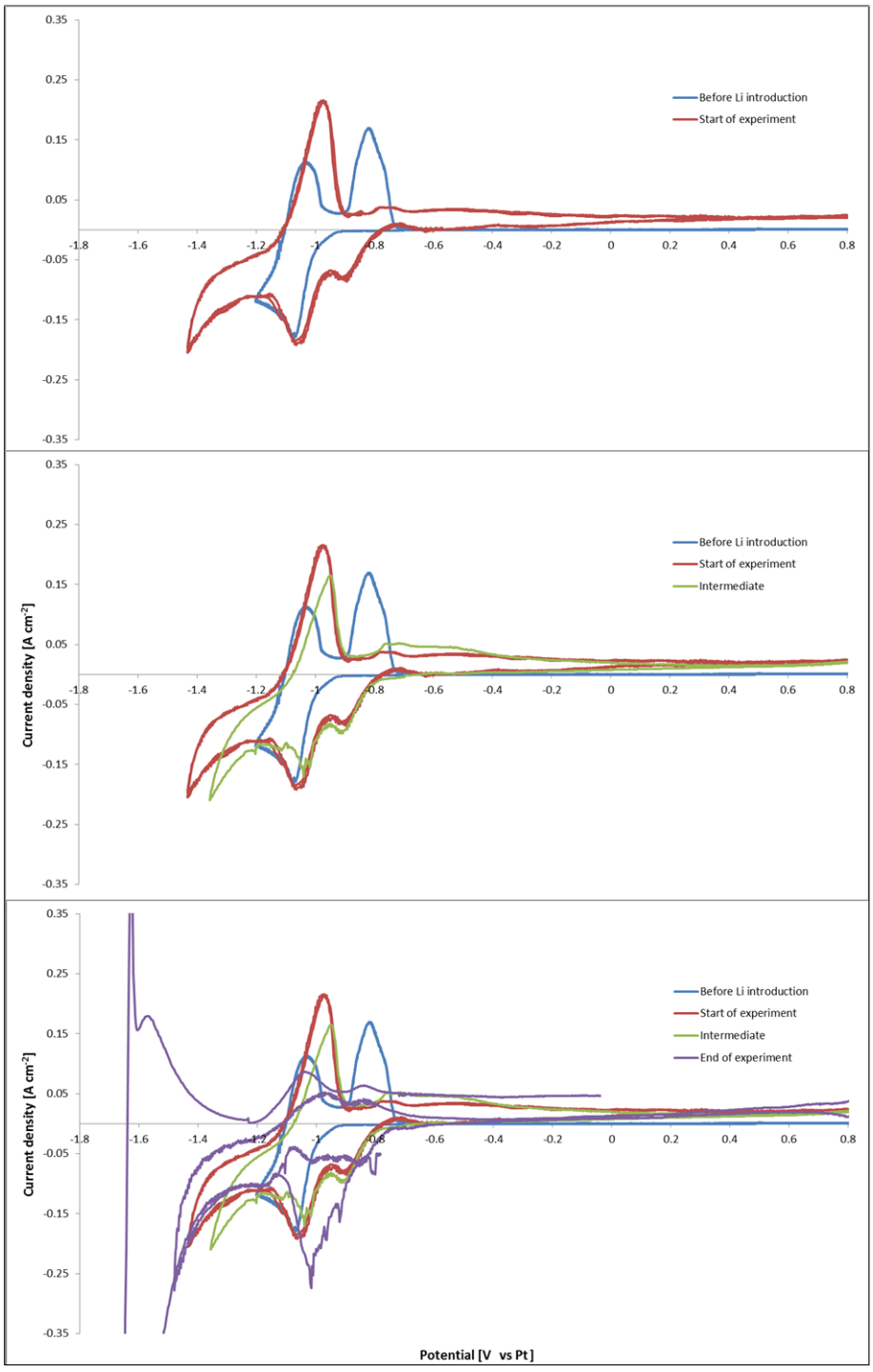

Figure 6.13. Evolution of CVs of LiF−ThF_4 (initially $c(ThF_4) = 2.31$ wt%) during extraction experiment with Bi−Li. $A = 0.22$ cm^2, $T = 1173$ K, $\nu = 200$ mV s^{-1}. WE: Mo, CE: glassy carbon, RE: Pt.

newly emerged peak is inconclusive. It might correspond to a Bi-Th alloy formation on the electrode, since bismuth particles (drops) were likely entrained in the salt.

ICP-MS analysis of the periodic salt samplings confirmed that extraction reached completion around one hour after the first sampling was taken, and about 95 % of Th was extracted—see Table 6.3 and accompanying Figure 6.14.

6.5.2 Discussion

One of the drawbacks of this measurement lies in the experimental arrangement—the reductive extraction commences immediately after both phases are at least partially molten. This prevents the capture of the initial portion of the extraction, since salt melting is not an instant process and electrodes can only be inserted when the salt is fully molten. This initial portion of the extraction, which contains the most drastic change in concentration, is inevitably lost.

Another issue was presented by bismuth drops entrained in the salt. Caution was exercised not to immerse the electrodes too deep into the salt to avoid touching the bismuth phase. Even without touching, bismuth particles most likely existed in the salt phase, probably due to bismuth's considerable vapor pressure at 1173 K. This prevented reliable data collection at the electrodes since the current was fluctuating appreciably.

ICP-MS analysis of the salt samples delivered values consistent with extraction process. Since the concentrations in the bismuth phase were calculated by mass balance, there may be error associated with the "Th in Bi" curve in Figure 6.14. If experiments were to be repeated, it would make sense to analyze the bismuth phase as well to see if the mass balance holds. This was not pursued, since it is difficult to take a sample of the bismuth phase (while both the bismuth and the salt are molten) without incurring some cross-contamination between the Bi and salt. The liquid Bi is the denser phase and settles below the molten salt. Better sampling approach is to use a metallic ladle that fills with the denser liquid upon immersion.

Another issue brought up previously (see Section 5.8.2) was the rate at which the crucibles cracked. The life of a crucible usually spanned only two or three tests where bismuth and salt were present together, due to bismuth expansion upon solidification.

Table 6.3. Results of LiF−ThF_4 sampling during extraction experiment with Bi−Li. Time is referenced to the first sampling after the salt was completely molten. Content in bismuth calculated based on mass balance.

Time [min]	Th in salt [wt%]	Th in Bi [wt%]
-	(initial: 2.31)	(complement)
0	1.00±0.03	1.31
30	0.23±0.02	2.08
50	0.13±0.02	2.18
70	0.09±0.01	2.22
100	0.12±0.01	2.19

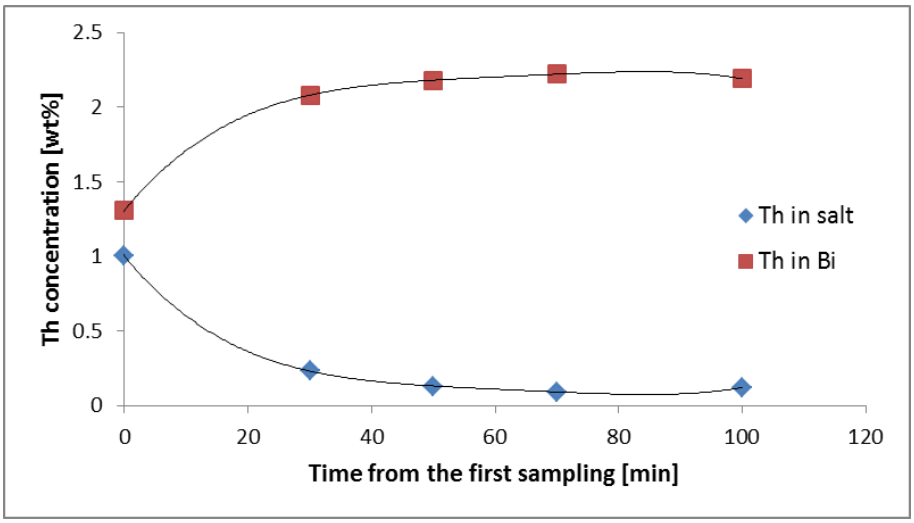

Figure 6.14. Results of LiF−ThF_4 sampling during extraction experiment with Bi−Li. Graphical representation of data in Table 6.3.

The setup could be improved significantly by having separate containers for each phase. For example, a larger salt crucible can hold a smaller crucible filled with bismuth. After salt melts, electrodes are positioned into the salt (and tested) and only then is the bismuth crucible introduced. This way the initial portion of the extraction is not lost. As another benefit of this approach, since the bismuth content is much smaller, there should be no significant entrainment of bismuth drops that would cause interference with the measurement. Extraction would reach completion

later (due to smaller interfacial area available) and thus more data points could be collected along the way.

Such a setup was conceived as a next option after these operating issues were encountered, but was not implemented since work on a new project (chloride salts) was already underway.

CHAPTER 7

PART I CONCLUSIONS

An electrochemical study of LiF−ThF_4, LiF−UF_4, and LiF−ThF_4−UF_4 systems at 1173 K was performed using CV. A molybdenum working electrode (inert to thorium) was used to investigate reduction mechanisms of both analytes, and to provide correlation between signal (peak current density) and analyte concentration.

Thorium reduces in a single step, four-electron exchange [Th(IV)/Th], which is in agreement with previous studies. Uranium reduces prior to thorium in a series of two reduction peaks. The second reduction (to uranium metal) appears to be a three-electron exchange [U(III)/U], again in agreement with previous studies.

The thorium system was found to be reversible below scan rates of 0.25 V s^{-1}, while the uranium system was found to be reversible in the whole investigated range of 0.1–0.3 V s^{-1}.

The diffusion coefficient for thorium was found to slightly decrease with increasing concentration. The average value for the concentration range investigated is $D_{Th} = 2.8 \pm 0.9 \times 10^{-5}$ cm^2 s^{-1} (for ICP-AES determined concentrations), while the value for infinite dilution is $D_{Th} = 4.2 \times 10^{-5}$ cm^2 s^{-1}. Diffusion coefficient for uranium was found to slightly increase with increasing concentration. The average value for the concentration range investigated is $D_U = 5.0 \pm 1.8 \times 10^{-5}$ cm^2 s^{-1} (for ICP-AES determined concentrations), while the value for infinite dilution is $D_U = 2.3 \times 10^{-5}$ cm^2 s^{-1}.

Considering averaging over the whole concentration range, these values can still be regarded in agreement with previous studies (which only investigated one concentration).

Calibration curves of cathodic peak current density vs. thorium or uranium concentration were produced up to about 5 wt% AnF_4. Linear regression of the

data was used with satisfactory accuracy for the considered application.

A practical importance of this result is that the linear regression gave satisfactory results even without accounting for the variability of diffusion coefficient with concentration. In other words, detailed D vs. C plots are not necessary (at least for the studied concentration range) in order to construct calibration curves.

Experiments in the ternary salt confirmed that the final reduction peaks of thorium and uranium were sufficiently apart from each other, suggesting the electrochemical separation of uranium from thorium-rich salt matrix is feasible.

Satisfactory concentration monitoring of uranium by CV (using previously developed calibration curves) was demonstrated. Concentration monitoring of thorium turned out to be problematic, due to increase in surface area by previous uranium deposition. The increase could not be accounted for by straightforward means. This increase in surface area in turn produced exaggerated signal, which would correspond to unrealistic concentration.

In the salt/bismuth extraction experiment, many technical difficulties were encountered that prevented collection of satisfactory CV data (crucible cracking, bismuth entrainment in the salt, loss of initial portion of extraction—see Chapter 6.5 for details). The analysis of the salt samples collected during the extraction run confirmed that thorium readily extracts into bismuth if no uranium is present. This is detrimental in the actual operation, and it underscores the need for tight process monitoring that would stop the extraction once all uranium is recovered.

An improved salt/bismuth experimental setup was suggested, where each phase would occupy a separate crucible—a small crucible containing bismuth would be immersed inside a larger crucible containing salt. This way the crucible cracking could be eliminated. The progress of the extraction could also be monitored right from the beginning, and the steady state would be reached later, since the mass transfer rate would be limited across a relatively small interfacial area. Bismuth entrainment in the salt would most likely be minimized as well, so clearer CVs could be expected.

Regarding the feasibility of using CV for real-time concentration monitoring in a reactor application: uranium content can be monitored with satisfactory accuracy;

some other method than CV needs to be employed for thorium monitoring. There are other electrochemical methods more suited for this task, e.g. normal pulse voltammetry (NPV). NPV employs electrode cleaning before each data point collection, thus achieving minimization of prolonged uranium codeposition and associated surface area growth.

Regarding the feasibility of using CV for the salt/bismuth extraction process monitoring application: CV can be used satisfactorily, since it is uranium that will be disappearing (extracting into bismuth) from the salt phase, and so the diminishing uranium peak could reliably indicate the approximate remaining uranium concentration. Thorium signal would most probably not interfere with the uranium peak, since the separation is sufficiently large (this was not confirmed experimentally due to technical difficulties with salt/bismuth setup).

PART II

CHLORIDES

CHAPTER 8

APPLICATION IN ELECTROREFINING

The second part of this work concerns actinide monitoring in molten chlorides, with application in spent fuel electrorefining.

Results from the electrochemical studies in chlorides were published in the ECS Transactions (47) and in JES Focus Issue on Progress in Molten Salts and Ionic Liquids (48). Essential paragraphs, figures and tables from these publications have been reproduced here.

8.1 Pyroprocessing

8.1.1 Concept

Pyroprocessing in its broader meaning is any metallurgical process which occurs at high temperatures and which facilitates some change of the metal of interest. A narrower meaning of the term—the one used here—describes the electrometallurgical treatment of the UNF consisting of several steps.

It was pioneered by the Integral Fast Reactor (IFR) program developed at the Argonne National Laboratory (ANL) (49). The program ran between 1984 to 1994 (when the federal funding was canceled, three years before completion (50)). However, the facility that treats the reactor fuel, known as Fuel Conditioning Facility (FCF; previously known as Fuel Cycle Facility) is still operational (2017). It is now a part of the Idaho National Laboratory (INL). Instead of producing fuel for IFR, it conditions the used fuel for disposal under the Spent Fuel Treatment (SFT) mission.

The IFR concept was based on a fast-neutron breeder reactor. The reactor was physically connected to a hot cell in which irradiated fuel could be disassembled, processed, and recycled to make new fuel assemblies. The idea was to close the nuclear cycle to conserve resources while minimizing waste. The concept was also aimed at achieving inherent safety of operation, and proliferation resistance (49).

Despite its limited application in the U.S., other countries have expressed interest in further developing it for commercial implementation (51–54). South Korea has expressed interest in having a full-scale commercial facility for treatment of domestic UNF (10, 55). GE Hitachi has proposed to the United Kingdom the concept called PRISM which is based on IFR. PRISM is supposed to turn UK's large plutonium stockpile into electricity—a direct competition to the mixed oxide fuel (MOX) reactor option originally considered for this purpose (56).

8.1.2 Reactor

The reactor used for the demonstration of the IFR concept was the Experimental Breeder Reactor II (EBR-II), which first achieved criticality in 1965 (50). The fuel elements used during the IFR demonstration were uranium rods alloyed with zirconium (U/Zr alloy). These were inserted into stainless steel tubes together with some sodium, which acted as a heat-transfer medium. The elements were assembled in a honeycomb fashion and were positioned in a pool of liquid sodium.

The pool design, as well as the metallic fuel, were selected to promote inherent safety during both normal and abnormal reactor operation. Specifically, the core design choices should achieve core reactivity shutdown and decay heat removal, both without reliance on operator action or outside source of power. The choice of metallic fuel furthermore promotes higher breeding capability by providing more excess neutrons than oxide fuel (57).

The inherent safety claims were verified by two tests in 1986, which simulated accidents involving loss of coolant flow, with regular shutdown devices intentionally disabled. The reactor safely shut down without operator interaction, purely due to laws of nature (49, 58).

8.1.3 Pyroprocessing flowsheet

The reactor was connected to the FCF which served as the electrometallurgical fuel treatment facility. The fuel treatment was driven by the desire of conserving resource while minimizing problematic waste, in particular eliminating plutonium and other minor actinides from the waste stream. In the traditional (once-through) cycle, large amounts of UNF containing plutonium would eventually be buried under-

ground, which would pose potential environmental—as well as proliferation—hazards (groundwater contamination; waste sites becoming plutonium mines) (49).

The goal of IFR's FCF was to reintroduce plutonium and minor actinides back into the reactor for burnup. At the same time, pure plutonium metal extraction should not be possible anywhere during the treatment, as that would contribute to proliferation risk.

In order to achieve these tasks, a flowsheet of several unit operations was devised, coined pyroprocessing. It was imperative to make these operations uncomplicated, since most steps require remote handling inside an inert atmosphere hot cell.

Nowadays, the SFT mission has goals that are different from the original IFR mission. Consequently, there are several versions of the flowsheet, each offering different products and waste streams. One version of the pyroprocessing flowsheet is depicted in Figure 8.1 for illustration.

In this particular flowsheet, the fuel is first chopped into smaller pieces, then transferred into the electrorefiner where uranium (or mixed uranium/plutonium) product is collected. This product is further treated in a cathode processor (here it can be isotopically down-blended with depleted uranium, if desired) before finally cast into ingots in a casting furnace.

There are two waste streams associated with this process. A metallic waste is essentially the cladding material plus noble FP that do not dissolve in the electrorefiner. This type of waste is cast into a metal waste form. The salt from the electrorefiner operation is another waste stream, containing (besides the solvent itself) TRU and FP. This type of waste is contacted with zeolite (an aluminosilicate microporous mineral) which incorporates the environmentally harmful components into its matrix. Once the zeolite micropores are loaded with waste, hot pressing is used to close the micropores, effectively immobilizing the waste inside the structure. This creates ceramic waste form.

The scale of the FCF pyroprocessing operation is referred to by INL as "engineering-scale." More commonly this is called "pilot-scale." Fuel batch sizes are limited to about 10–25 kg, depending on which electrorefiner is used and how it is configured. Maximum combined processing rate that is theoretically achievable for the Mark-IV

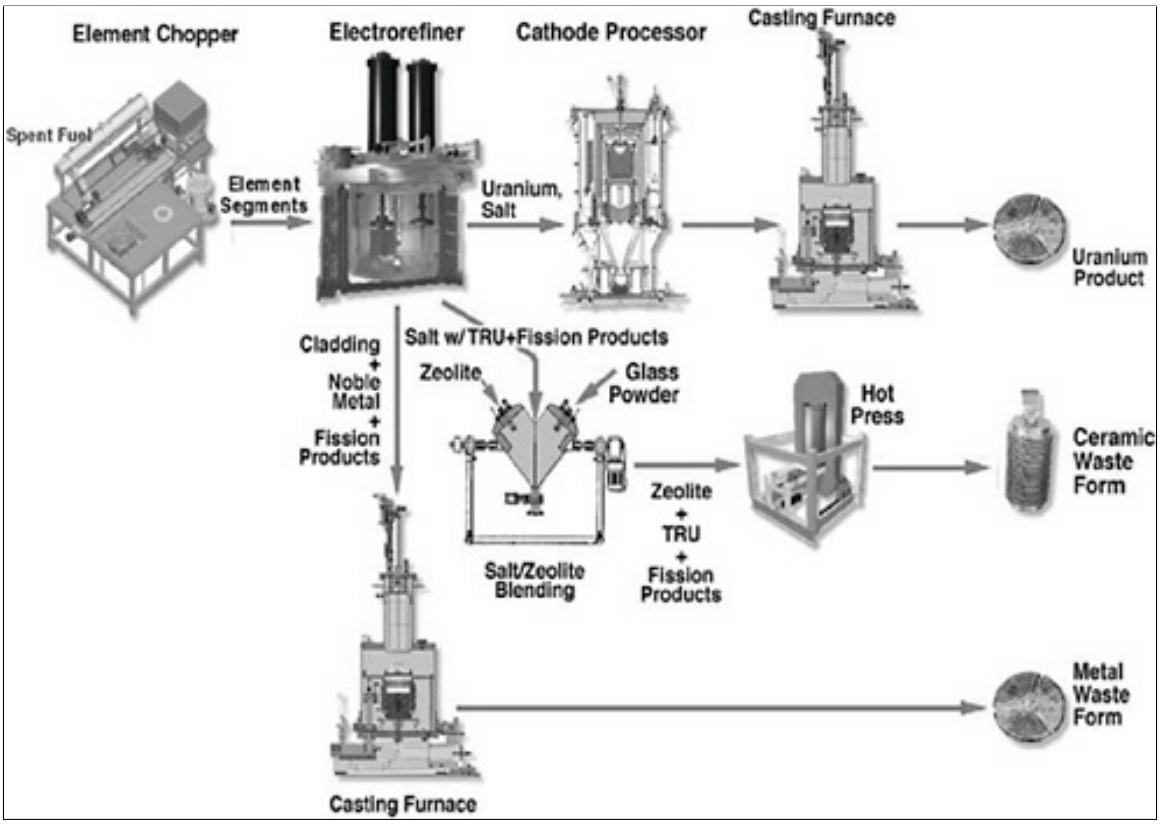

Figure 8.1. One version of the pyroprocessing flowsheet. [Argonne National Laboratory, public domain]

and Mark-V electrorefiners operating in tandem is about 5000 kg/year.

Several advantageous aspects can be identified when pyroprocessing is compared to aqueous UNF treatment:

- Applicability to both oxide and metallic fuel.
- Compact, scalable process.
- Solvents resistant to irradiation.
- Allows processing of fuel with short cooling time.
- Nonmoderating solvents.
- Ability to extract either uranium or uranium/plutonium product.
- Compact waste forms.

Limitations of the technology include the necessity of running at high temperatures (electrorefiner ≈ 500 °C, casting furnace ≈ 1200 °C) and in inert atmosphere. The product purity is lower than in competing technology (especially PUREX), which can also be regarded as an advantage from the non-proliferation standpoint. Also, safeguards against nuclear non-proliferation for this system still need to be fully developed.

8.1.4 Electrorefiner

The most instrumental unit operation of the pyroprocessing is the electrorefining operation. The electrorefiner is displayed in Figure 8.2. Here, the chopped fuel elements are inserted in a basket and immersed into a molten salt. A carbon steel rod is also inserted into the salt and electrical current is applied by connecting the two structures by an external power supply.

The basket acts as an anode, promoting dissolution (oxidation) of the least stable components—actinides (and some FP). At the same time, the steel rod acts as a cathode, promoting deposition (reduction) of (primarily) uranium.

Molten LiCl−KCl eutectic salt is selected as the solvent for its extraordinary electrochemical stability, which allows electrochemical extraction (reduction to metal) of actinide elements—something not possible in an aqueous environment. Depending on the applied voltage, either pure uranium or uranium-plutonium product is obtained.

Several modifications can be made to the process, where the inert (steel) cathode can be changed to a reactive one to promote recovery of TRU. Liquid cadmium cathode originally planned for the IFR project is one example—the cathode consists of a pool of cadmium and TRU from the salt are recovered into this pool.

Table 8.1 shows redox potentials of various components of the system. The useful electrochemical window is defined at lower limit by the decomposition potential of the solvent component—in this case the reduction of lithium—and at the upper limit by the oxidation potential of the anode material—iron in this case.

A typical electrorefiner operation consists of applying a voltage difference across the electrodes so that uranium is simultaneously oxidized at the anode and reduced at the cathode (exclusively, or together with plutonium and/or other actinides). If

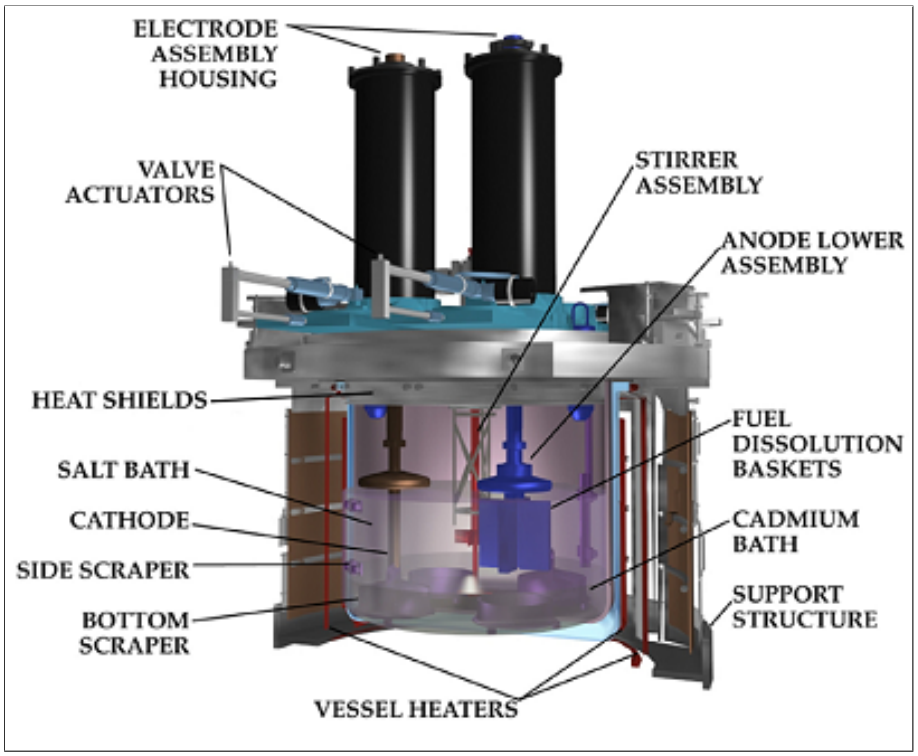

Figure 8.2. IFR Mark-IV electrorefiner. [Argonne National Laboratory, public domain]

Table 8.1. Standard redox potentials of different classes of elements of interest, and their location in the electrorefiner.

Class	Couple	E^0 [V vs. Pt(II)/Pt]	ΔE [V]	Location
Salt components	Li(I)/Li	-3.41	-	Salt (lower pot. limit)
Reactive	La(III)/La	-2.91	0.50	Dissolved in salt
FPs	Nd(III)/Nd	-2.85	0.06	
TRU and other	Pu(III)/Pu	-2.57	0.28	Salt or cathode
actinides	Th(IV)/Th	-2.41	0.16	
Uranium	U(III)/U	-2.25	0.16	Cathode
Anode material	Fe(II)/Fe	-1.17	1.08	Not dissolved
and noble FPs	Mo(III)/Mo	-0.64	0.53	(anode, upper pot. limit)

the applied voltage is too large, however, other components (reactive FPs, which were also dissolved at the anode) will start codepositing at the cathode—an inadvertent operating condition.

The key is therefore to select an optimum voltage, which changes with time as concentrations of various components are altered. Note, that the Mark-IV electrorefiner (Figure 8.2) currently in use is controlled based on amperage, not voltage, so the above reasoning does not apply.

8.1.5 Electrorefiner monitoring

Since the optimum applied voltage changes with concentrations of dissolved components, it is necessary to accurately monitor these concentrations.

Current practice involves sampling of the salt and performing traditional chemical analysis. The drawback is evident—considerable lag time between sampling and results of such analysis, which can be on the order of weeks.

Such analysis—while accurate—provides only a single snapshot of the concentration in time and implies that either: (a) the operation of the electrorefiner is paused after each sampling and restored (with applied correction) after the results are known (highly impractical); or (b) that the electrorefiner operation is inherently suboptimal since the applied voltage cannot be accurately determined in real time (this does not reflect the current operation strategy of the Mark-IV electrorefiner, which is controlled based on amperage, not voltage).

Another obvious drawback of such sampling is the necessity of handling hazardous sample. Not surprisingly, these drawbacks mirror the ones mentioned in Chapter 3. In order to improve the situation, an in-situ, real-time monitoring is sought to streamline the operation and to serve as a safeguards tool.

Voltammetry methods—like the ones described and employed in fluoride monitoring—are again a natural choice in such harsh environment due to their robustness. However, there are some limitations of voltammetry methods.

The most notable difficulties stem from (a) the poor resolution of elements with close redox potentials, and (b) from the increase in surface area caused by the deposition of the more noble element (discussed earlier in Chapter 6.4). The two

main analytes (uranium and plutonium) have similar redox potentials (implying (a)), and uranium is present in large quantities (implying (b)). Therefore, one cannot expect to achieve very accurate concentration readings from such signal. Several post-processing approaches exist to correct these shortcomings, they are discussed in the following literature survey chapter.

A significantly different approach is the employment of some other analytical technique not dependent solely on voltammetry—the one conceived in this thesis—which is in fact a combination of two techniques. The controlled-potential electrodeposition step is combined with in-situ alpha particle spectroscopy of the deposit. The drawbacks of voltammetry are avoided, while the advantage of real-time monitoring present in voltammetry is traded for a near real-time one.

The theoretical foundation of this hyphenated technique will be described in later chapters, but the general idea is that a snapshot of the actinides present in the salt can be preserved (electrodeposited) on a metal surface, which itself is a detector of alpha particles.

Alpha particles are emitted by all actinides and their spectra are unique not only for each element, but for each isotope. The resolution of a suitable detector of alpha particles permits identification and quantification of individual actinides with greater accuracy than what voltammetry would be capable of.

With isotopic resolution, many diversion scenarios involving isotopic manipulation could be detectable with this technique. This opens up an avenue for truly safeguard-grade process monitoring, which is something a voltammetry alone cannot achieve.

CHAPTER 9

LITERATURE SURVEY

The electrorefiner—a unit operation of pyroprocessing—is operated on a pilot scale in the United States (9), South Korea (10), and Japan (51). The U.S. version has evolved from the original concept into Mark-IV and Mark-V electrorefiners to treat the driver and blanket fuels of the EBR-II, respectively. In South Korea, a continuous ER concept has been developed by Korea Atomic Energy Research Institute (KAERI). Literature survey of possible actinide concentration monitoring solutions for these systems is presented here.

As mentioned in the previous chapter, the problem of cumbersome sample collection is persistent in the electrorefiner, implying insufficient process knowledge leading to sub-optimal operation and safeguarding difficulty. Attempts to solve this issue include simulations, which are supposed to provide evolution of the electrorefiner salt composition based on the last known composition and applied conditions. The advantages of not having to physically sample the salt, and having the prediction of the composition for an arbitrary point in time are immense. Several more or less successful simulation packages of the evolution of salt composition have been produced (59–62).

Nevertheless, a complete substitution of physical monitoring of the electrorefiner salt by simulations is not realistic, physical monitoring still needs to be performed. Among methods not based on voltammetry, Laser Induced Breakdown Spectroscopy (LIBS) received some attention (63, 64). However, the majority of work has been focused on voltammetry techniques due to their robustness (capable of operation in high-radiation and high-temperature environment, remote operation) and ability to deliver results in real time (45, 65–68).

ANL selected CV method as the one best suited for concentration determina-

tion (45, 68). Data treatment is not straightforward, though, and additional post-processing (e.g., semidifferentiation of the signal) is required. Problems with higher actinide concentrations not following the linearity trend were also reported. CV as well as semi-differentiation are described in more detail in Chapter 4.

A qualitatively different treatment of voltammetry data was performed by Rappleye (38, 69), who investigated the use of multivariate techniques. These use a greater portion of the signal than traditional univariate techniques, which use only a narrow region or a single point—typically a peak. Multivariate techniques of Partial Least Squares (PLS) and Principal Component Regression (PCR) were applied to simulated and real data. Particularly PCR provided consistently more accurate results than traditional peak height determination.

The limitations of voltammetry have been described earlier (see Section 8.1.5) and have been experienced first-hand in this work. *Part I* relied exclusively on CV and the results were sub-optimal (see Chapter 6).

Consequently, for *Part II* a novel technique that does not rely exclusively on voltammetry has been employed as an alternative. This novel technique was proposed by Lei R. Cao (Ohio State University) to the U.S. Department of Energy under the Nuclear Energy University Program (NEUP), which funded the project under the name: "Monitoring of Actinide Concentrations in Molten LiCl-KCl Salt using Alpha Spectroscopy" (project: CFA-15-8074) (70).

The project has two separate, yet interconnected, tasks: (a) To develop a novel, semiconductor wide-band gap detector capable of withstanding the electrorefiner environment while detecting alpha particles, with sufficient resolution. [The Ohio State University responsible for this task]; (b) To develop a technique for reliably depositing (preconcentrating) a small amount of actinides onto the detector surface. [The University of Utah responsible for this task.]

The reason for selecting alpha spectroscopy is based on several advantages described below. The two-step mode of operation of the semiconductor detector is schematically depicted in Figure 9.1.

The need for preconcentration of the actinides onto the detector surface is a necessity, given by a poor penetrating capability of alpha particles. Without pre-

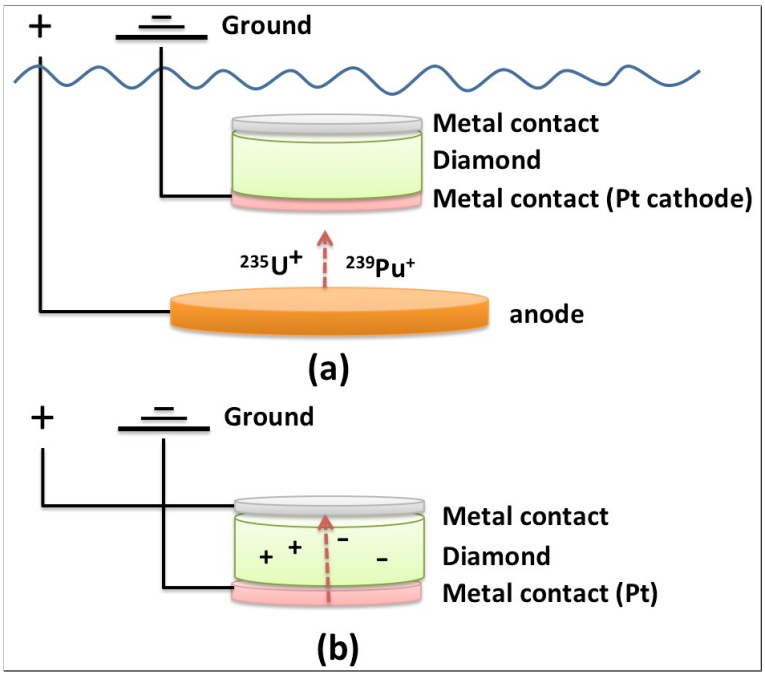

Figure 9.1. Proposed sensor structure and two-step operation: (a) electrodeposition step in the salt, (b) measurement step outside the salt. [© Lei R. Cao]

concentration, the sensing volume around the detector would be limited to a small thickness, equivalent to the range of alpha particles in the salt (tens of µm) (71). Moreover, as alpha particles would lose energy in collisions with the salt before reaching the sensor, poorly defined spectra would result. Concentrating the actinides on the sensor's surface effectively increases the detection volume by several orders of magnitude and improves the shape of the resulting spectrum.

One advantage of using alpha spectroscopy stems from the fact that only relatively few elements emit alpha particles. Coincidentally, these are the elements of interest to the nuclear energy—most notably thorium, uranium, and plutonium. On the other hand, gamma spectroscopy relies on detecting energetic photons (gamma rays), which are emitted by virtually all radioactive species. A gamma spectrogram of the electrorefiner salt contains hundreds of overlapping peaks that would require extensive deconvolution treatment. In contrast, an alpha spectrogram contains only several peaks; besides, the major ones having sufficiently different energies to be spatially well separated.

Another advantage of the alpha spectroscopy is furnished by its ability—as a

nuclear method—to distinguish individual isotopes rather than individual elements (like chemical methods, such as voltammetry). In process monitoring alone, this feature has little value. However, in the nonproliferation safeguarding scheme, such an ability is of great importance, because it brings the possibility of detecting isotopic manipulations that can not be detected by chemical methods.

For example, a scenario can be depicted where the operator is diverting fuel elements containing highly enriched uranium (valuable resource for diversion) from the anode basket of the electrorefiner, while surrogating elements with low enrichment (less valuable resource for diversion). During the electrorefining operation, everything would look normal, the masses of uranium would match the expected amounts. However, if the alpha spectroscopy-based concentration monitoring was applied, an immediate mismatch in the ratio of uranium isotopes would have been picked up.

Regarding the previous use of preconcentration of actinides by electrodeposition directly onto alpha particle detector, the literature is restricted to aqueous systems (72, 73). Here, an exhaustive precipitation of trace actinide elements from aqueous solution was performed prior to alpha particle detection—an approach different from the one explored in this thesis, where a near real-time monitoring is attempted by relatively fast (non-exhaustive) deposition step.

In summary, the newly conceived hyphenated technique—where electrochemical separation is combined with alpha spectroscopy detection—is an alternative to other techniques aimed at electrorefiner process monitoring, specifically actinide concentration determination. A similar technique has been demonstrated, albeit for determining trace concentrations of actinides in aqueous solutions. Therefore, this work is considered both relevant and novel to the field of molten salt electrochemistry for nuclear applications.

CHAPTER 10

THEORETICAL TREATMENT

In this chapter, the basic theoretical frameworks of electrodeposition and alpha spectroscopy are discussed, as well as a treatment of the hyphenated analytical technique original to this work.

Some concepts of electrochemistry have already been discussed in Chapter 4. More comprehensive treatment of the electrochemical concepts is found in (30, 74). More comprehensive treatment of alpha particle spectroscopy is found in (75).

As in Chapter 4, conditions of planar electrode are considered, as well as diffusion being the rate determining mass transfer process. The assumption of small electrode area vs. sufficiently large solution volume (small A/V conditions) is also held, signifying that the passage of current does not alter the bulk concentrations of species. By "concentration" the salt concentration of the oxidized species is implicitly assumed, since the salt concentration of the reduced form in a soluble-insoluble transition (deposition on cathode) is zero.

10.1 Double-layer charging and cell time constant

During a potential step, some amount of current is momentarily drawn to charge the electrical double-layer. This charging current I_c flows in addition to the faradaic current I_f (i.e. the current due to redox change of a chemical species). The amount of charging current depends on the magnitude of the applied potential step ΔE, the solution resistance R_s [Ω] and the double-layer capacitance C_d [F]:

$$I_c = \frac{\Delta E}{R_s} exp(\frac{-t}{R_s C_d}) \tag{10.1}$$

According to Equation 10.1—which is the analogy of the RC circuit problem in electrical engineering—the charging current decays exponentially with time. It has a circuit time constant (here called cell time constant) τ_{RC} [s] equal to $\tau_{RC} = R_s C_d$.

The current drops to 5 % of its initial value at $t = 3\tau_{RC}$, and can be considered negligible beyond $t > 5\tau_{RC}$. The total amount of charge that has been spent on charging the double layer (and not on producing a chemical change) can be calculated by integrating equation 10.1:

$$Q = EC_d[1 - exp(\frac{-t}{R_s C_d})] \tag{10.2}$$

Double-layer charging current can make a significant contribution to the total charge in some cases where rapid potential steps are employed, its influence then needs to be taken into account. Otherwise, its contribution is usually neglected.

10.2 Exchange current density and overpotential

At equilibrium, there is no net chemical reaction happening. However, the forward and backward reactions are still occurring, only their magnitude is exactly matched so that their effects cancel out.

In reaction kinetics, these rates are characterized by standard heterogeneous rate constant k^0. In electrochemistry, a more convenient term—the exchange current I_0 [A]—is introduced, which is proportional to k^0:

$$I_0 = FAk^0c \tag{10.3}$$

It is more convenient to present currents normalized with respect to electrode area A [cm^2]. After this normalization, the current I become the current density i [A cm^{-2}]:

$$i = I/A \tag{10.4}$$

$$i_0 = I_0/A = Fk^0c \tag{10.5}$$

Analogous to k^0, i_0 signifies how fast the kinetics of a particular reaction is. The smaller i_0 is, the larger "activation" is required in order to deliver desired rate of reaction. In electrochemistry, this "activation" is termed overpotential η [V]—the potential in excess of the equilibrium potential that is required to fulfill the

rate—while the rate of reaction is simply the net observed current density i. The overpotential is defined as:

$$\eta = E - E_{eq} \tag{10.6}$$

where E_{eq} [V] is the equilibrium potential. The amount of overpotential has two contributing factors. The first one is due to the actual reversibility of the particular reaction as described above; while the other one is due to the mechanism of nucleation, i.e., how easy it is for the first couple atoms to deposit on the electrode and form a starting nucleus/seed upon which new atoms will grow (crystallization overpotential). In this regard, the overpotential is also a function of the electrode material.

10.3 Limiting current

If purely reaction kinetics dictated the rate of electrochemical reaction, then the observed current (rate) could be made progressively higher and higher by simply applying larger overpotentials.

In reality, however, the reactant is usually quickly consumed at the electrode (especially in molten salts at elevated temperatures, where the electron transfer is rapid). In such a case the rate is limited by the mass transfer, which brings new reactants to the electrode. This constraint sets an upper limit on the maximum achievable current that can be sustained. It is termed the limiting current I_l [A].

The limiting current, and limiting current density i_l [A cm^{-2}], are calculated according to the following equations (30):

$$I_l = zFAmc \tag{10.7}$$

$$i_l = zFmc \tag{10.8}$$

where m [cm s^{-1}] is the mass transfer coefficient, which signifies how vigorously is the new reactant brought to the surface of the electrode. If diffusion is the only factor taken into account (as is often the case), the equation for i_l becomes:

$$i_l = \frac{zFcD^{1/2}}{\pi^{1/2}t^{1/2}} \tag{10.9}$$

10.4 Current-overpotential relationship

The relationship between i and η, which incorporates i_0 is known as the Butler-Volmer equation (30):

$$i = i_0[exp(\frac{-\alpha zF\eta}{RT}) - exp(\frac{(1-\alpha)zF\eta}{RT})] \tag{10.10}$$

where α is the transfer coefficient (a measure of the symmetry of the potential barrier). This simplified form of the current-overpotential equation is valid when the electrode reaction is limited by reaction kinetics alone (small overpotentials), and not by mass transfer. Under these conditions, the current-overpotential curve is represented by the blue curve in Figure 10.1.

When mass transfer conditions cannot be neglected (larger overpotentials), the following equation is used (30):

$$i = \frac{exp(\frac{-\alpha zF\eta}{RT}) - exp(\frac{(1-\alpha)zF\eta}{RT})}{\frac{1}{i_0} + \frac{exp(\frac{-\alpha zF\eta}{RT}) - exp(\frac{(1-\alpha)zF\eta}{RT})}{i_l}} \tag{10.11}$$

The above equation assumes equal anodic and cathodic limiting currents. The resulting curve is represented by the red curve in Figure 10.1.

The actual recording of the current-overpotential relationship is also termed polarization curve. Usually, only one direction from the equilibrium is investigated (i.e., for deposition, only the cathodic branch of negative overpotentials is plotted), and thus only one quadrant of the plot is shown. Polarization curves are used to estimate i_l, and to specify regions of different rate limiting steps (activation/reaction kinetics control, mass transfer control, or mixed control).

10.5 Tafel plots

Instead of a simple current density, one can plot an absolute value of the logarithm of i. Then the plot in Figure 10.1 transforms into one called the Tafel plot—see Figure 10.2.

The convenience of the Tafel plot lies in the observation that: (a) the intercept of the extrapolated linear segment gives the value of i_0; while (b) the value of α can

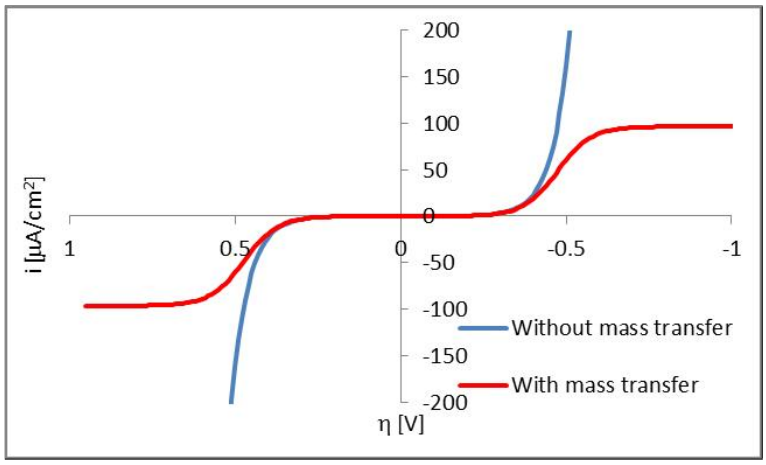

Figure 10.1. Computed current density vs. overpotential curves with and without mass transfer effects ($n = 1$, $i_0 = 9.6 \times 10^{-3}$ μA cm^{-2}, $\alpha = 0.5$, $m = 1.0\times 10^{-3}$ cm s^{-1}, $c = 1.0\times 10^{-6}$ mol cm^{-3}).

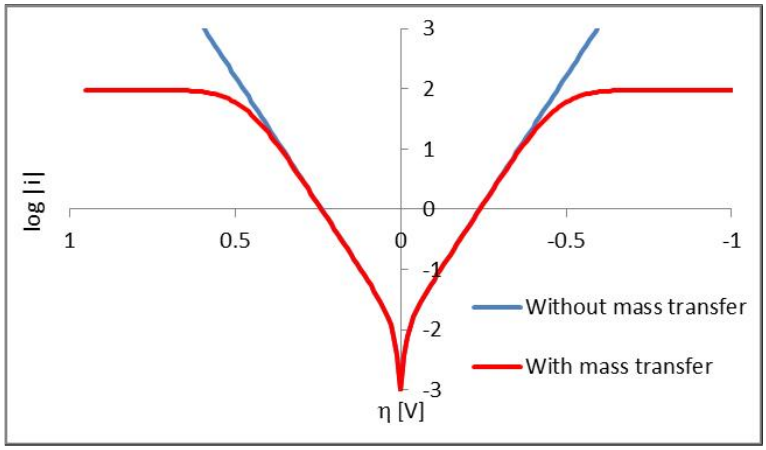

Figure 10.2. Computed Tafel plots with and without mass transfer effects ($n = 1$, $i_0 = 9.6 \times 10^{-3}$ μA cm^{-2}, $\alpha = 0.5$, $m = 1.0\times 10^{-3}$ cm s^{-1}, $c = 1.0\times 10^{-6}$ mol cm^{-3}).

be calculated from the slope of the linear segment. The transformation of Equation 10.10 into a logarithmic form yields:

$$\log|i| = \log i_0 - \frac{\alpha z F \eta}{RT} - \frac{(1-\alpha) z F \eta}{RT} \tag{10.12}$$

The section closest to the equilibrium potential in Figure 10.2 ($-0.1 < \eta < 0.1$) takes into account both the forward and the backward reactions (both exponential terms in Equation 10.10).

The "middle" section ($-0.3 < \eta < -0.1$ or $0.1 < \eta < 0.3$) is the linear segment—

here only one direction of the reaction is considered, the contribution from the opposite one is negligible. Thus, one term is eliminated and the Equation 10.12 assumes a linear form of $y = a + bx$. Here the intercept a is $\log i_0$, and the slope b is either $[-\alpha zF/2.3RT]$ or $[(1-\alpha)zF/2.3RT]$.

The last section ($\eta < -0.3$ or $\eta > 0.3$) is influenced by mass transfer and thus again deviates from linearity.

10.6 Morphology of electrodeposits

10.6.1 Microscopic considerations

Crystallography of the individual elements of interest (thorium, uranium, zirconium) and that of the substrate (stainless steel, nickel) plays a role in the initial formation of the new phase. Whether the cell lattice parameters are similar or dissimilar influences how the newly formed thin film grows.

Thorium exists in two crystallographic solid phases. Below 1360 °C the α phase is stable (76). The crystal structure of α-thorium is cubic close packed (space group: $Fm\bar{3}m$), with cell parameters (77): $a = b = c = 508.4$ pm.

Uranium exists in three crystallographic solid phases. The α phase is stable up to 668 °C. Since electrodeposition is conducted at 500 °C, the parameters of alpha phase are used. The crystal structure of α-uranium is orthorhombic (space group: $Cmcm$), with cell parameters (78): $a = 285.4$ pm, $b = 587$ pm, $c = 495.5$ pm.

The highly asymmetric orthorhombic structure makes it difficult for atoms of alloying metals to substitute for uranium atoms or to occupy spaces between uranium atoms in the crystal lattice. Only molybdenum and niobium have been observed to form solid-solution alloys with uranium (79).

Zirconium exists in two crystallographic solid phases. Below 863 °CC the α phase is stable (80). The crystal structure of α-zirconium is hexagonal close packed (space group: $P6_3/mmc$), with cell parameters (81): $a = b = 323.2$ pm, $c = 514.7$ pm.

Stainless steel is an alloy, essentially a polycrystalline electrode. Its metallographic surface features of the crystalline structures are on the order of 10–100 µm. Deposits are likely to preferentially deposit on certain alloy phases/crystalline orientations. If the desired thickness of the deposit is smaller than the diameter of the polycrystalline

features, then the thickness uniformity of the deposit—as well as good coverage of the surface by such deposit—is difficult to achieve.

Nickel exhibits cubic close packed crystal structure (space group: $Fm\bar{3}m$), with cell parameters (82): $a = b = c = 352.4$ pm.

The cell parameters of the elements of interest are summarized in Table 10.1.

Depending on deposit/substrate affinity and environmental conditions, the growth process is carried by in one of three modes: (a) Frank-van der Merwe (FM), (b) Volmer-Weber (VW), or (c) Stranski-Krastanov (SK) (83).

In FM mode the adatoms are very compatible with the substrate and prefer to attach directly to it, forming a layer-by-layer growth. In VW mode the opposite is the case—the interaction between the adatoms is stronger than the interactions between the adatom and the substrate. Consequently, three-dimensional (3D) islands are formed. The SK mode is the intermediate mix of FM and VW; the growth initially follows the FM pattern, until the film reaches a critical thickness, and switches to VW (83).

As can be seen from Table 10.1, the lattice parameters of the substrate (Ni) and those of the film (Th, U, Zr) are markedly different. This mismatch predicts that the VW growth mode is likely to be encountered.

10.6.2 Macroscopic considerations

There are generally three possible types of (macro) deposit formed by electrolysis:

- Compact.
- Dendritic.
- Spongy/granular.

The main factors that decide which type of deposit is obtained are the value of exchange current density i_0, and the magnitude of overpotential η (74).

Processes with low or medium i_0 will yield compact deposits at low overpotentials, while dendritic or spongy deposits are obtained at larger η. Processes characterized by large i_0 will yield spongy/granular deposits at low overpotentials, while dendritic deposits are obtained at large η.

Table 10.1. Unit cell parameters of the elements of interest.

Parameter	Th	U	Zr	Ni
Structure	ccp	ortho	hcp	ccp
Space group	$Fm\bar{3}m$	$Cmcm$	$P6_3/mmc$	$Fm\bar{3}m$
a [pm]	508.4	285.4	323.2	352.4
b [pm]	508.4	587.0	323.2	352.4
c [pm]	508.4	495.5	514.7	352.4
α, β [°]	90	90	90	90
γ [°]	90	90	120	90

In electrorefining and electrowinning, electrolytes are usually of medium exchange current densities and overpotentials are selected close to the end of Tafel linearity (see Figure 10.2). Powdery deposits are obtained at current densities considerably larger than diffusional i_l (74).

The morphology can be changed substantially by the presence of additives (74). That is not a possibility in the case of the UNF electrorefiner, since it is not desirable to put any additives into the radioactive molten salt, especially not organic additives.

Another option for improving the quality of electrodeposits is to carry out the electrodeposition at a periodically changing rate (84), as will be discussed in Sections 10.9.1 and 10.9.2 below.

10.7 Chronopotentiometry

Chronopotentiometry (CP) is a controlled-current technique, where electrode potential is the dependent variable. It is mostly used as a constant-current technique, either for determination of diffusion coefficient (or concentration), or for electrolysis.

In the first manner, a suitable cathodic current value is selected and the resulting potential vs. time curve is analyzed. Initially, the potential of the electrode moves to a value characteristic of the studied couple. As the oxidized form is being consumed and the reduced form increases its concentration, the potential gradually shifts in the cathodic direction. Finally, when the oxidized form is exhausted, some other couple

has to accommodate the steady supply of electrons crossing the electrode/solution interface—a potential suddenly jumps to a different (more cathodic) value characteristic for the new couple.

The time it took to reach this transition is called the transition time τ [s]. It is directly related to concentration and diffusion coefficient. One can therefore be determined, if the other is known (typically the concentration is known and the diffusion coefficient is being determined). The relationship is called Sand's equation (85):

$$i\tau^{1/2} = 0.5zFAcD^{1/2}\pi^{1/2} \tag{10.13}$$

In the second manner—electrolysis—a component of the salt can be reduced (deposited) onto the electrode by applying current to the cell. Conversely, the material of the electrode can be oxidized (corroded) into the solution. The magnitude of these processes is influenced by the amount of current one passes through the cell.

CP electrolysis is frequently used in industry, where large processing rates necessitate large throughput of material. Arbitrarily high currents can be delivered to the electrochemical cell to expedite the process (increase the rate), as long as busbars that carry the current to the cell are properly dimensioned (among other factors). In the laboratory settings, in contrast, other methods are often given preference over CP electrolysis, due to its drawbacks discussed below.

The convenience of the method lies in a simple transformation of the current and elapsed time into the amount of charge passed (Q). If all of the charge is used up in the desired chemical reaction, then the relationship is straightforward:

$$Q = it \tag{10.14}$$

The drawback of the deposition is that once the desired depositing ion cannot fully satisfy the prescribed current (flow of charge), then some other ion has to codeposit with it to make up the difference. This is usually detrimental.

The situation is further complicated since the desired ion might initially satisfy the prescribed current, but later on it does not. This is because its concentration keeps diminishing due to mass transfer limitation.

Unless vigorous mixing of the solution is established (to promote large mass transfer) or low current is selected, this method is susceptible to codeposition of other components from the solution.

10.8 Chronoamperometry

CA is a controlled-potential technique, where current is the dependent variable. Its use in electrodeposition is in some aspects more convenient than the use of CP. By precisely selecting the applied potential, any unwanted codeposition (of some more cathodic species) is eliminated.

The method produces a current response described by Cottrell's equation (37):

$$i = \frac{zFAcD^{1/2}}{\pi^{1/2}t^{1/2}} \tag{10.15}$$

One drawback of this method is its less straightforward (in comparison to CP) conversion of current and elapsed time into charge:

$$Q = \int_0^t i(t)dt \tag{10.16}$$

Since current fluctuates and never absolutely matches the prescribed Cottrell equation, one can estimate the time needed for passing a certain amount of charge with only limited accuracy (in CP, the current, and consequently the charge is known with great accuracy). Fortunately, modern instruments can keep track of the total charge and automatically stop the process when the desired charge is accumulated.

Another drawback of the method is its relative slowness. No matter how large the overpotential, the current will quickly decay ($t^{-1/2}$) to small values due to mass transfer limitations (depletion of a diffusion layer) if no stirring is provided.

10.9 Advanced deposition techniques

To improve the quality of the deposit as well as to shorten the deposition time, more sophisticated methods are in use, where the electrodeposition happens at a periodically changing rate. Examples of these methods include: reversing current (also called periodic reversal (86) or bipolar current-pulse (87)), pulsating current, alternating current superimposed on direct current (74, 84), and repeating chronoam-

perometry (also called potentiostatic pulse deposition (88)). The first and the last one are described below.

10.9.1 Reversing current

Reversing current waveform is schematically represented in Figure 10.3. Periods of cathodic current density i_c are alternated by periods of anodic current density i_a. The anodic current is either of shorter duration ($t_a < t_c$), smaller magnitude, or both, so that net deposition is achieved.

The overall (average) current density i_{avg} is calculated according to the following equation:

$$i_{avg} = \frac{i_c t_c - i_a t_a}{t_c + t_a} \tag{10.17}$$

10.9.2 Repeating chronoamperometry

Repeating chronoamperometry (RCA) is the controlled-potential analogy of reversing current described in previous section.

It alternates between two set potentials. The first potential is very cathodic and has a short duration, hence called pulse E_{pulse}. The second potential is set to open-circuit potential or slightly anodic, and the duration is longer, hence called relaxation E_{relax}. The resulting waveform is depicted in Figure 10.4.

In theory (74), this ensures that only the very stable portion of the deposit remains in place, since the less stable portion (like dendritic formation) is dissolved during the relaxation period.

The deposition time is also shortened compared to a simple CA. The reason is that in RCA some average current density is established (similar to Equation 10.17). This i_{avg} is relatively high, in comparison to the current density in a simple CA, which quickly ($\propto t^{-1/2}$) decays due to mass transfer limitations.

A plot of accumulated charge vs. time is shown in Figure 10.5. Sharp slopes of cathodic direction corresponding to pulses are alternated by longer, more gradual slopes of anodic direction corresponding to relaxations. A saw-toothed pattern is obtained.

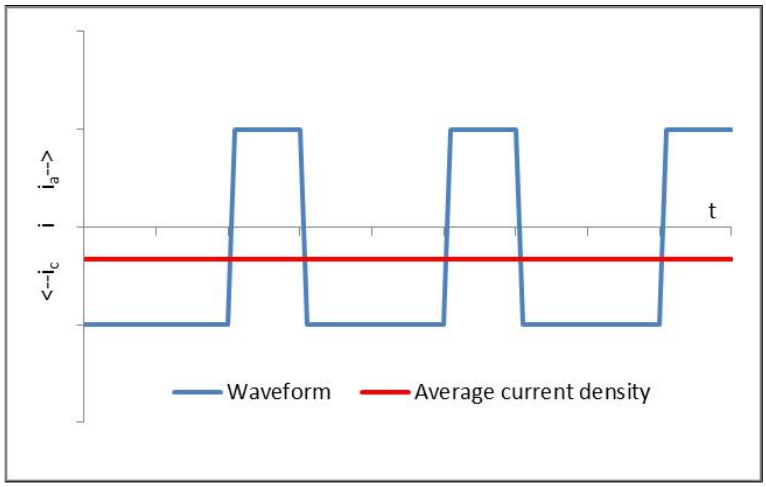

Figure 10.3. Computed waveform of the reversing current with the average current density shown.

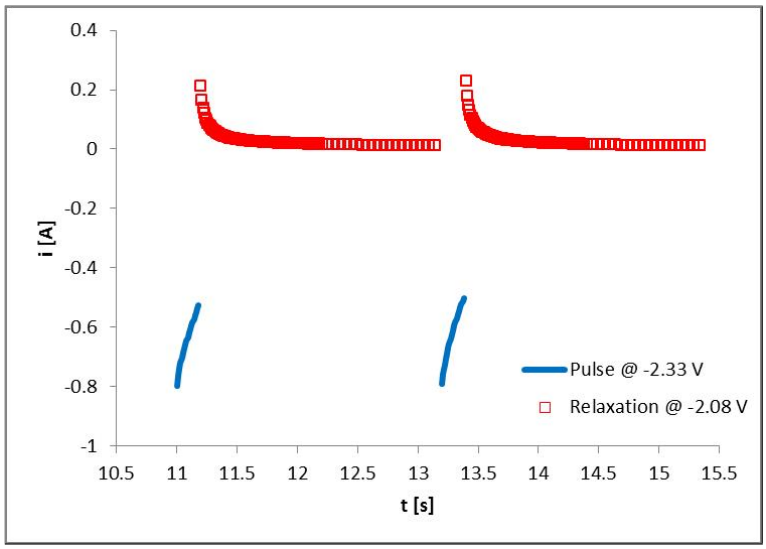

Figure 10.4. Section of the RCA current transient of thorium on nickel ($A = 4$ cm^2, $T = 773$ K, $c(ThCl_4) = 1.5$ wt%).

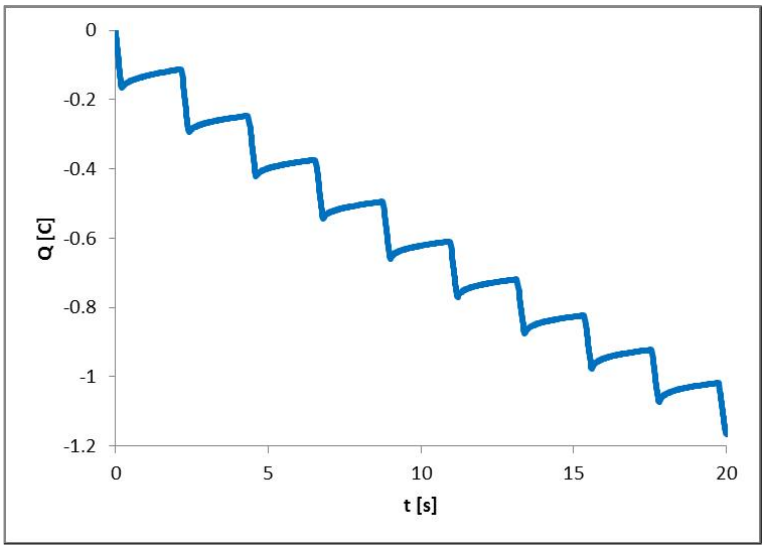

Figure 10.5. Section of the RCA deposition evolution with time of thorium on nickel (E_{pulse} = -2.33 V, E_{relax} = -2.10 V, $A = 4$ cm^2, $T = 773$ K, $c(ThCl_4) = 1.5$ wt%).

10.10 Alpha spectroscopy

Alpha spectroscopy is an analytical technique for measuring alpha particle energies. Alpha particles are energetic, doubly charged helium nuclei He^{2+} emitted by the heaviest elements (traditionally of $Z > 82$, although some lighter exceptions exist) as part of their radioactive decay.

This on one hand considerably limits the scope of the technique (only several elements can be identified), while on the other hand it makes the technique very suitable for special applications where only heavy, radioactive elements are of interest (typically nuclear applications).

Each alpha-emitting radioisotope has a characteristic signature spectrum of one or several alphas of particular, well defined energy. Often times, these energies are sufficiently different from each other. Consequently, very little overlap of the signal is typically encountered and a sample of several alpha-emitting species can be resolved without particular difficulty.

A sample spectrogram of four radioisotopes is displayed in Figure 10.6. The peak energy of the alpha particle is characteristic to the individual radioisotope, while the intensity (or the peak area) can be quantified into concentration.

The main drawback of the technique, and a reason why it is not widely employed

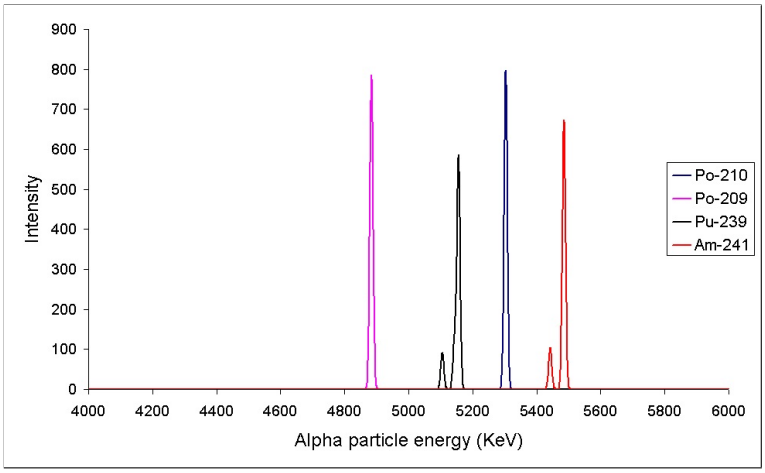

Figure 10.6. Computed alpha particle spectrogram of four radioisotopes. [user "Cadmium" at Wikipedia, public domain]

in the industry (in contrast to gamma spectroscopy, which relies on essentially the same principles), is the need of tedious sample preparation. This is brought about by the nature of alpha particles: although very energetic from the absolute point of view (their energies are in the range of MeV, while those of gamma rays are typically in the range of keV), they lack the ability to penetrate even thin layers of material (e.g. a piece of paper). This necessitates extremely close distances between the emitter and the detector—something that is usually quite impractical.

Typically, liquid samples for alpha spectroscopy are either (a) evaporated to a metal disk and measured by a gas proportional counter, (b) co-precipitated with barium-radium sulfate and measured by a plastic scintillator, or (c) evaporated and redissolved in a liquid scintillation cocktail and measured by a liquid scintillator (70).

In the UNF electrorefiner setup explored in this thesis, an in-situ alpha detector is envisioned. The advantages and drawbacks of this selection have been mentioned previously (Chapter 9).

Here, one particular limitation that needs to be realized is reiterated: a simple immersion without preconcentration of alpha emitting actinides onto the detector would most likely produce unusable output. Alpha particles would lose energy in collisions with the salt prior to reaching the sensor, which would create poorly defined, broad peaks.

Concentrating the actinides on the sensor's surface improves the shape of the resulting spectrum (narrower peaks), particularly by increasing the probability that a full-energy particle is registered (one where 100 % of the particle's kinetic energy was deposited inside detector's sensitive volume, implying no energy was lost to collisions before reaching the detector). Such events create a valuable full-energy peak which energy is characteristic for each particular radioisotope.

Concentrating the actinides onto the surface also effectively increases the detection volume by several orders of magnitude, which translates into higher encountered intensities.

10.11 Scanning electron microscopy

In order to evaluate which deposition method is comparatively better than other, a surface morphology of the deposit is sought. Scanning electron microscopy (SEM) can provide such information.

Traditional optical microscopes rely on detecting photons of visible electromagnetic spectrum (wavelengths of 390–700 nm) reflected from the target surface. SEM, in contrast, relies on detecting electrons reflected from such surface.

Due to quantum-mechanical nature of subatomic particles, the electron, too, can be ascribed a wavelength. This wavelength depends on its kinetic energy—accelerating electrons in the SEM by a sufficient voltage (E_{acc} [kV]) produces electrons of wavelengths orders of magnitude smaller than photons of visible electromagnetic spectrum. Consequently, objects orders of magnitude smaller (than in optical microscopes) can be detected.

Once electrons hit the target, some fraction is reflected away (backscattered), while another fraction disrupts bonds of the electrons present in the target, expelling secondary electrons (and X-rays) away. Both the backscattered and the secondary electrons are detected, and an image is reconstructed based on the intensity seen by any particular region of the detector.

Since electrons hit the target normal to its plane, no information about the depth of the displayed features (deposits, ridges, valleys) can be obtained from such geometry. However, modern instruments feature a tilt of the target plane, which

enables the electrons to hit the target under an angle. Therefore, an approximate depth (thickness) information can be acquired. Deposit thickness is one of the crucial parameters sought to be optimized, since it has immense influence on alpha spectroscopy measurement.

Energy dispersive X-ray spectroscopy (EDS) probe is often coupled to the SEM. It allows chemical identification by collecting and analyzing characteristic X-rays produced by the interaction of the electron beam and the target. It also offers quantitative analysis based on the intensity of the characteristic X-rays, albeit the reliability of such analysis is limited if lighter elements ($Z < 11$) and/or small amounts (less than 5 at%) are encountered.

The coupling of SEM with EDS has one more advantage, in that an approximate thickness of the deposit can be estimated (even without tilt). This approximate thickness is called "analytical area" (z_{max} [µm]) and is calculated using Castaing's formula (89):

$$z_{max} = 0.033(E_{acc}^{1.7} - E_{em}^{1.7})\frac{M}{\rho Z} \tag{10.18}$$

where E_{em} [keV] is the emission energy of the characteristic X-ray, M is atomic mass, ρ [kg m^{-3}] is density, and Z is atomic number.

10.12 Hypothesis of the proposed analytical technique

10.12.1 Qualitative considerations

The newly proposed hyphenated analytical technique aims to provide concentration information for two actinide elements simultaneously present in a salt.

The aim is to estimate actinide concentrations in the UNF electrorefiner. Thus the solvent is the LiCl-KCl eutectic salt and the temperature is 773 K (500 °C) which correspond to the operating conditions of the electrorefiner.

The elements of interest are thorium and uranium in this study; in theory it could be any other pair of actinides, as long as they are amenable to electrodeposition onto detector surface.

The advantage of this method is the ability to resolve two actinide elements, which is problematic in voltammetry—the current preferred analytical technique (reasons have been described previously in Chapters 6, and 9). The way to overcome this

shortcoming of voltammetry is to rely on alpha spectroscopy as the detection method instead.

However, in order for the detector to collect useful spectra, the actinides need to be preconcentrated/separated from the salt onto the detector surface. This preconcentration is achieved by electrodeposition, a prerequisite objective necessary to fulfill the main goal. Thus, the technique is considered a hybrid/hyphenated one, since it features a separation step (facilitated by electrodeposition technique) followed by a detection step (facilitated by alpha spectroscopy technique).

Since the actual detector is simultaneously being developed as well (at the Ohio State University), a surrogate material onto which the deposition is carried out is selected. A metal coupon of the same material as the detector surface and approximately the same dimensions is chosen.

Different elements deposit with uneven rates (generally due to their different redox potentials, and valences). Unless exhaustive electrodeposition is realized (where the entirety of both analytes is deposited), the amounts of individual elements in the deposit may not directly correspond to their amounts in the salt. Exhaustive electrodeposition is time consuming and possibly detrimental to alpha spectroscopy output if the deposit is too thick, therefore, this option is not pursued.

Due to the reason stated above, data from alpha spectroscopy alone is not sufficient to reconstruct the image of concentrations in the salt—it merely gives the ratio of the elements in the deposit.

Because of this complication, another piece of information—besides the ratio given by alpha spectroscopy—is needed to reconstruct the salt concentrations. Such information is furnished by knowing the deposition amount and elapsed time. It is desirable to always deposit the same amount of material to approach the idea of constant deposit thickness for each measurement (a condition important to alpha spectroscopy). If the deposited amount is constant, then the deposition time becomes the variable of interest.

One can infer the "combined" concentration of species based on the deposition time required to deposit constant amount of material. The hypothesis assumes that higher "combined" concentrations will have short deposition time, while lower

concentrations will have longer deposition time. Alpha spectroscopy then resolves the ratio of those species.

In other words, electrodeposition delivers the time t it took to deposit the (constant) amount of charge Q_{tot}, while alpha spectroscopy delivers the molar ratio X_1/X_2 of the two elements. By combining these two pieces of information together, concentration is obtained, as schematically depicted in Figure 10.7. The exact mathematical treatment required to arrive to the concentration determination is demonstrated in the next section.

The logical course of action for successful concentration prediction follows:

1. Establish reliable deposition method that works for one element.
2. Verify this method works for the other element as well.
3. Perform tests with variable concentrations in single-analyte salt to obtain correlation of deposition time vs. concentration.
4. Repeat these tests with the other single-analyte salt.
5. Combine both analytes into a two-analyte salt and perform experiments with many different salt compositions.
6. Analyze the matrix effects.
7. Produce a correlation of the "combined" concentration and deposition time.
8. Compare this method to a benchmark (voltammetry).

It was decided that the alpha spectroscopy measurements will be substituted with SEM-EDS ones for this early stage of development. The original plan was to send each sample coupon for alpha spectroscopy analysis (to resolve the ratio of elements, and to provide some training set for the detector development) to the Ohio State University. This was found impractical and excessive. Samples would need to be shipped regularly to the Ohio State University where researchers would have to spend excessive amounts of time analyzing them.

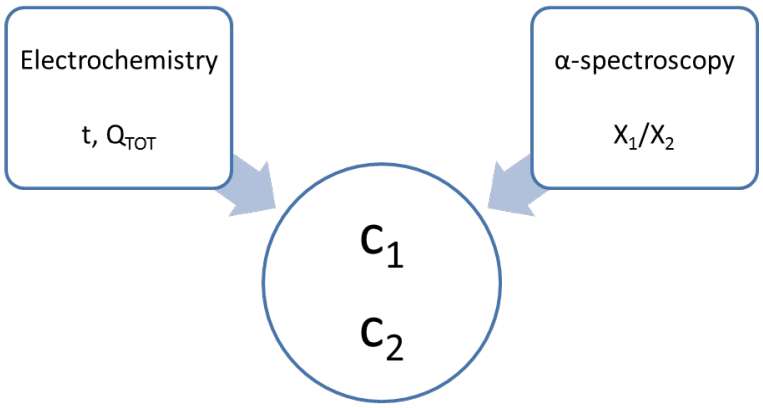

Figure 10.7. A schematic representation of the new method. Concentration is obtained by combining the input from two techniques.

Moreover, many experiments involved only one element, the two-analyte testing started much later. Because each sample was already being analyzed at the University of Utah by SEM-EDS for the quality of the deposit, it was decided that the resolution of the EDS probe for estimating the ratios is sufficient.

Thus, the SEM-EDS effectively replaced the alpha spectroscopy in this early development phase. In real-life application, this would not be the case, since the deposition would occur directly onto the detector itself inside the electrorefiner; no removable metal coupons would exist.

10.12.2 Quantitative considerations

The deposition rate i (i.e., current density) is in general a function of applied potential, salt concentration and time:

$$i = f(E, c, t) \tag{10.19}$$

In order to establish proportionality between the deposited amount of analyte and its concentration in the salt, the dependence on applied potential needs to be eliminated. This is done by conducting the deposition under mass-transfer (diffusion) limited regime. There is no agitation (except natural convection) provided, thus by applying sufficiently large overpotential η, the current density i reaches its diffusion-limited value i_d described by Equation 10.15.

If a proportionality constant k is introduced, which encompasses all terms other than concentration, the result for controlled potential environment yields:

$$i_d = \frac{zFD^{1/2}c}{\pi^{1/2}t^{1/2}} = kc \tag{10.20}$$

Under these conditions the deposition rate (current density) is only a function of analyte concentration and time. For a two-analyte system (Th and U), the partial, diffusional current densities $i_{Th,d}$, $i_{U,d}$ are proportional to concentrations c_{Th}, c_U, respectively:

$$i_{Th,d} = k_{Th}c_{Th} \tag{10.21}$$

$$i_{U,d} = k_U c_U \tag{10.22}$$

The total observed current density i_{tot} is the sum of these partial current densities:

$$i_{tot} = i_{Th,d} + i_{U,d} \tag{10.23}$$

The amount of charge Q passed over time in a controlled potential environment is a time integral of current density as described by Equation 10.16. In this case:

$$Q_{Th} = \int_0^t i_{Th,d}(t)dt \tag{10.24}$$

$$Q_U = \int_0^t i_{U,d}(t)dt \tag{10.25}$$

In analogy with Equation 10.23, the total charge Q_{tot} is the sum of partial charges:

$$Q_{tot} = Q_{Th} + Q_U \tag{10.26}$$

By expanding Equation 10.26 further, the following relationships are obtained:

$$Q_{tot} = Q_{Th} + (\frac{Q_U}{Q_{Th}})Q_{Th} \tag{10.27}$$

$$Q_{tot} = Q_{Th}(1 + \frac{Q_U}{Q_{Th}}) \tag{10.28}$$

Equation 10.28 contains three unknowns (Q_{tot}, Q_{Th}, and Q_U). The software controlling the electrodeposition provides Q_{tot}, while alpha spectroscopy provides

mole fractions X_U and X_{Th}. These can be transformed into Q_U/Q_{Th} using Faraday's law ($Q = nzF$) (90):

$$\frac{Q_U}{Q_{Th}} = \frac{n_U z_U}{n_{Th} z_{Th}} = \frac{X_U}{X_{Th}} \frac{z_U}{z_{Th}} \tag{10.29}$$

Now both Q_{tot} and the ratio of Q_U/Q_{Th} are known, thus Equation 10.28 can be solved for Q_{Th}:

$$Q_{Th} = \frac{Q_{tot}}{(1 + \frac{Q_U}{Q_{Th}})} \tag{10.30}$$

Once Q_{Th} is determined, the desired unknown concentrations are obtained by expanding Equation 10.24 using 10.21 and rearranging:

$$Q_{Th} = \int_0^t i_{Th,d} dt = \int_0^t k_{Th} c_{Th} dt = c_{Th} \int_0^t k_{Th} dt \tag{10.31}$$

$$c_{Th} = \frac{Q_{Th}}{\int_0^t k_{Th} dt} \tag{10.32}$$

And similarly for the other analyte:

$$c_U = \frac{Q_U}{\int_0^t k_U dt} = \frac{Q_{Tot} - Q_{Th}}{\int_0^t k_U dt} \tag{10.33}$$

CHAPTER 11

EXPERIMENTAL SETUP

This section describes the setup arrangement for chloride experiments. Experiment scheduling, as well as a note on analyte salt synthesis, is also included.

11.1 Inert atmosphere glovebox

All electrochemical experiments were performed in an inert argon atmosphere glovebox described earlier in Chapter 5.

11.2 Furnace

Initially, a top-loading electric resistance furnace (Kerr Auto Electro-Melt) was used to heat the salt up to 773 K (500 °C)—the same furnace used in *Part I* (see Figure 5.2). The interior of the furnace consists of a graphite liner and a point heating element. A 50 mm diameter hole was drilled into the furnace lid to permit the passage of the electrodes.

Later in the project, a new front-door muffle furnace with a better controller was introduced (Thermo Scientific Thermolyne)—see Figure 11.1. This furnace was modified before use: the wall-embedded heating elements were repositioned to allow top-loading, and the electric leads were spliced to reach the connection ports. Next, a 50 mm diameter hole was drilled into the top of the furnace metal frame and through the top layer of insulation to permit the passage of the electrodes. This furnace did not contain a liner, instead a larger alumina crucible was used to contain any spills.

11.3 Potentiostat

The potentiostat was described earlier in Chapter 5. For the chloride salt work, different methods were used as described here.

For predeposition electrochemical tests the CV method was used, with scan rates

Figure 11.1. Photograph of the furnace (Thermo Scientific Thermolyne) used in later runs.

typically in the range of 0.025–0.3 V s^{-1}. The CA method was sometimes briefly used for electrochemically cleaning the electrode surface. For deposition, either CP, CA, or RCA methods were used (see appropriate sections in Chapter 10).

The RCA method saw a limitation in the potentiostat circuitry that made the data collection (and analysis) more cumbersome. Ideally, the output of the RCA is displayed in real-time on the monitor and a provision is made to stop the process once a particular amount of charge has been reached. This was not possible, however, since the time resolution required by the RCA (1 ms) prevented the instrument from displaying the data in real-time.

Instead, a number of deposition/relaxation cycles was specified prior to the run, then the instrument would perform the run, and display the results after the measurement has finished. The amount of charge was noted by the operator and a new run parameters were entered, with the number of cycles such as to approximately reach the desired amount of charge. This resulted in situations where the total charge was typically overshot, rather than precisely reached.

Another consequence of this instrument limitation was the need of performing several consecutive RCA runs instead of one continuous run. The disadvantage of performing consecutive runs lies in the fact that transient effects are encountered at the beginning of the next run. These effects are manifested by distorted cottrellian curves for the first couple deposition/stripping cycles before steady-state conditions are reached.

Particularly, (a) the momentary relaxation of the electrochemical system in-between the runs causes disruption of the established pulsation of the diffusion layer; and (b) the starting potential (at which the potentiostat will stabilize for a couple of seconds before performing the prescribed cycles) degrades the deposit quality.

Regarding (b), this starting potential (same or more anodic than E_{relax}) will disturb the accumulated deposit by partially oxidizing it for the duration of several seconds. This oxidized deposit is then promptly reduced back onto the electrode when the first couple cathodic pulses are applied, creating unusually large currents in the process. The first couple relaxation periods are affected as well, and display net cathodic currents instead of anodic ones. This has detrimental effect on the deposit morphology, since no (beneficial) oxidation takes place during these periods.

11.4 Chemicals

The base salt was LiCl−KCl eutectic (58-42 mol%, 44-56 wt%) (SAFC Hitech, 99.99 %, anhydrous)—the same salt used in an electrorefiner. The analyte salts were $ThCl_4$ (IBI-Labs, 99 %) and UCl_3 (99 %). AgCl (Alfa Aesar, 99.997 %) was used in RE preparation.

Later on, the commercial source for analyte salts became unreliable and an in-house synthesis of these salts was established (see subsection Analyte salt synthesis).

11.5 Electrochemical cell

11.5.1 Crucible and lid

Alumina (Al_2O_3) crucibles (AdValue Technology) inside the furnace were used to contain chloride salts.

Furnaces feature an opening at the top (see Section 11.2), which must be covered

by a lid. The lid serves to prevent heat loss as well as to align the electrodes. A non-conductive, four-hole macor (machinable glass-ceramic) custom manufactured lid was used—see Figure 11.2. The macor lid sat directly on the crucible lip.

A three-electrode setup was employed for both predeposition electrochemical tests, and for actual depositions. Two large circular openings in the lid (see Figure 11.2 were occupied by RE and CE, both sheathed by alumina tubes. The slit-shaped opening hosted the WE assembly used during deposition. The small circular opening was either used by a rod WE in predeposition electrochemical tests, or by a K-type thermocouple for temperature control (precision of ±2 K).

11.5.2 Counter electrode

The CE was a 12.7 mm diameter Zr rod (Alfa Aesar, 99.2 %) which was resting against the bottom of the crucible. The reason was the need to achieve very large surface area, that would surpass the surface area of the working electrode (4 cm^2, see Section 11.5.4), so that the deposition is not limited by the CE reactions. A typical salt depth of 30 mm brings the CE surface area to about 12 cm^2.

An alternative large surface solution is a coiled wire. However, the wire might become brittle as material is gradually lost from the electrode. Thus, a rod of large thickness was selected.

A reactive CE was sought to eliminate the generation of Cl_2(g) during electrodeposition, which would have occurred if inert CE was used. Instead, soluble $ZrCl_4$ was produced. By design, the half-cell reactions are as follows:

$$\text{At cathode: } ThCl_4 + 4e^- \rightleftarrows Th + 4Cl^- \tag{11.1}$$

$$\text{At anode: } Zr + 4Cl^- \rightleftarrows ZrCl_4 + 4e^- \tag{11.2}$$

Zirconium was selected based on several considerations:

- Its close standard reduction potential compared to thorium and uranium (91).
- Its chemical compatibility—the oxidized form $ZrCl_4$ is soluble in the salt.
- Expected presence in a real electrorefiner (Zr is a common fission product).

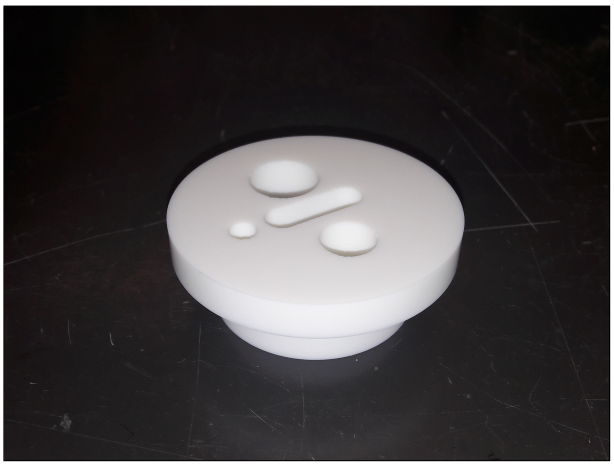

Figure 11.2. Photograph of the macor custom manufactured lid.

Excessive zirconium co-deposition is detrimental, as it would reduce the amount of deposited analytes (thorium and uranium) due to fixed amount of charge being passed at each deposition run. This would in turn produce inferior alpha spectra.

Complete elimination of zirconium co-deposition is unavoidable, since it reduces before either thorium or uranium (91). Some small amounts of zirconium always exist in the salt and consequently in the deposit.

However, zirconium co-deposition can be minimized by using fresh salts once zirconium content starts to show up in significant amounts in the deposit (implying its accumulation in the salt from the oxidation process is no longer negligible). Consequently, fresh salts were used every time a zirconium content of the previously run deposition test turned out to be more than a few atomic percent.

11.5.3 Reference electrode

The RE was immersed about 20 mm into the salt by the virtue of a viton ring that prevented it from slipping through the alumina sheath. The RE was a [Ag/AgCl(100 %)] type, consisting of a mullite tube filled with about 1 g of pure AgCl in contact with Ag wire (Alfa Aesar, 99.9 %). The top of the tube was terminated by a rubber stopper perforated to allow the passage of Ag wire.

The reason for selecting pure AgCl instead of the more ubiquitous solution of 1 % AgCl in LiCl-KCl was in the perceived superior stability of the electrode potential. The internal solution would easily buffer small concentration perturbations that inad-

vertently happen over the lifetime of the electrode (e.g., evaporation, decomposition) in comparison to the 1 % AgCl one, where any small concentration change of the internal solution results in deviation from the prescribed fraction which manifests itself as a potential drift.

11.5.4 Working electrodes and coupon holder

The WE used for predeposition electrochemical tests was either a 2 mm diameter tungsten rod (Alfa Aesar, 99.95 %), or a 2 mm diameter nickel rod (Goodfellow, 99 %). The immersion was controlled by a vertical translator (see next section for more details).

The WE used for deposition was a 0.5 mm thick rectangular coupon of either stainless steel (304, later 316), or low-carbon nickel-201 (Special Metals). Molybdenum and tungsten were also considered due to their resistance to corrosion. Molybdenum was not selected based on cost and the potential to form alloys. Tungsten was not selected (for coupons) due to difficulties in machining caused and associated costs.

The coupons were polished by a polishing tool to remove surface oxidation, and were immersed approximately 10 mm into the salt. Their width was also 10 mm, which brings the total geometric area of the immersed portion of a single coupon to 200 mm^2 (10 mm $\times$ 10 mm $\times$ 2 sides).

Usually there were two coupons immersed—one for the University of Utah post-experimental analysis, and one for the Ohio State University researchers.

The coupons were attached to a stainless steel coupon holder by means of micro setscrews. The immersion depth was varied by a positioner located on the holder. The positioner could slide up or down the shaft of the holder and lock in specific position by means of an adjusting screw. This positioner would rest against the lid, thus delimiting the distance between the holder and the crucible (i.e., immersion depth).

The whole three electrode assembly with the lid is depicted in Figure 11.3, and the detail of the steel holder with coupons and positioner is displayed in Figure 11.4.

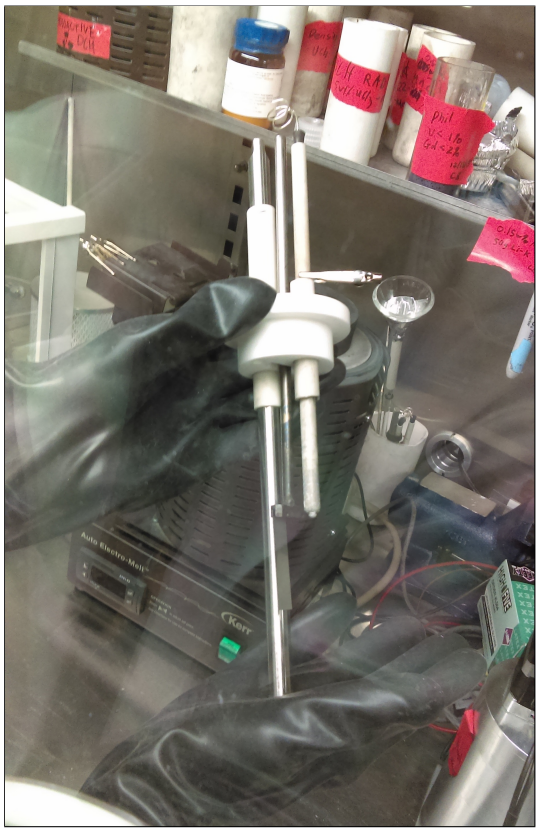

Figure 11.3. Photograph of the three electrode assembly seated in the lid. CE: leftmost one, WE: middle one (only one coupon attached to the holder), RE: rightmost one.

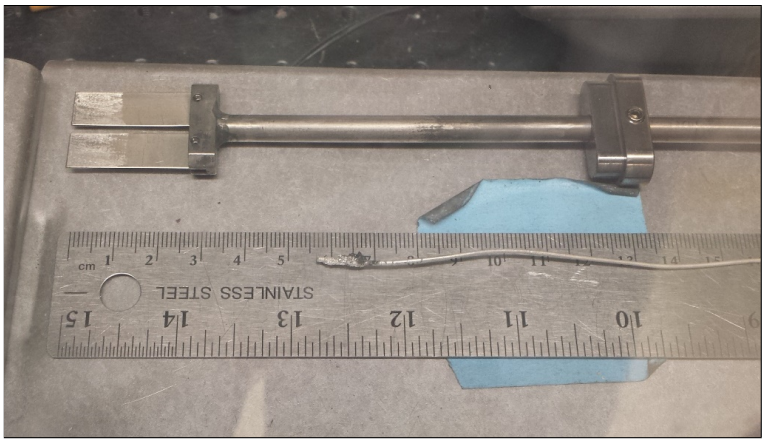

Figure 11.4. Photograph of the coupon attachment. Top: detail of the attachment of two coupons (polished immersion side) to the holder, positioner on the right. Bottom: autopsy of failed RE—the silver wire with silver dendrite accumulation.

An issue with salt creeping up the coupons was encountered in the early stages. The initial immersion depth displayed by the (frozen) salt on the coupon is not the highest point the salt eventually reaches. It has been observed that the salt creeps up the coupon a few additional millimeters and creates a thin film there.

This has presented a problem since the first batch of coupons was cut very short (about 10 × 15 mm). The salt wetted the entirety of the coupon and entered the screw cavities, which prevented the screws from liberating the coupon once the salt solidified.

Magnetic fastening was under investigation as a possible alternative, employing the idea of having a strong magnet in-between the holder and the coupon. Eventually the solution was found in simply using longer coupons (initially 10 × 50 mm, then 10 × 32 mm). The longer coupons showing deposit and some salt creep are shown in Figure 11.5.

The analysis of the immersion depth becomes less straightforward due to this phenomenon, since there are two values for a single physical immersion—the initial value and the final value. Since only a thin film is created, the initial values are taken as more accurate.

11.6 Vertical translator

A significant improvement in the analysis of the electrochemical signal can be gained if the electrode area is known with good accuracy. A vertical translator enables this by providing accurate immersion reading, far superior to a simple dip of the electrode and subsequent frozen salt length measurement (which was used in the fluoride experiments).

The translator (Velmex XN10-0012-M02-71) consists of an electric motor and a vertical slide on which an arm carrying the electrode is mounted. This arm can be lowered/raised by very small increments (0.005 mm). The vertical translator is shown in Figure 11.6.

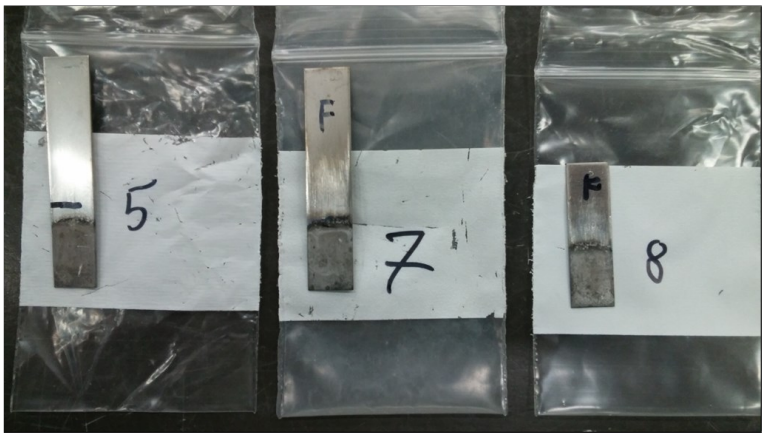

Figure 11.5. Photograph of coupons from Runs #5, #7 (304 stainless steel, 50 mm length), and #8 (316 stainless steel, 32 mm length) with visible regions of deposit. The salt marks are several mm above the initial immersion of 10 mm, signifying a salt creep has occurred.

Figure 11.6. Photograph of the vertical translator (Velmex XN10-0012-M02-71) with aluminum arms for holding the WE.

By recording electrochemical signal (e.g., peak height in CV) at several different immersions, one can obtain a linear trend ($y = ax + b$) which will carry the original immersion depth of the first measurement as its intercept (b). An arbitrary immersion can then be selected based on that analysis, with great accuracy.

It is worth noting that other techniques for gaining accurate immersion depth exist as well—one of them was performed in the same laboratory by Rappleye, who developed a glass-sealed working electrode (GSWE) (92).

11.7 Salt analysis

Analyte concentration from samples was determined using ICP-AES (Spectro Genesis FES). The salt was sampled while molten using a stainless steel threaded rod. The solidified sample was then shaken off the rod, crushed in a mortar and pestle, weighed and dissolved in 15 mL of 10 % HCl.

Custom standards (Inorganic Ventures) in 10 % HCl ensured that the matrix of samples and standards was matched.

11.8 Coupon analysis

11.8.1 Deposition

SEM-EDS was used for analysis of deposits on the coupons. The instrument is shown in Figure 11.7. Micrographs by SEM (Hitachi S-4800) were taken with sufficient magnification to distinguish newly deposited structures from the substrate. A tilt of the stage was sometimes used to assess the depth and therefore the thickness of such structures.

Next, candidate micrographs were scanned by the EDS (Oxford EDS) and a color map of individual elements was created, together with the approximate composition of the mapped region. These maps formed the basis for understanding the patterns with which thorium and uranium deposit, and in what proportion to each other (with respect to their proportion in the salt).

The success of a particular deposition run was judged by the uniformity with which the deposit was present, as well as whether excessive co-deposition of trace elements (particularly Zr) took place or not.

Figure 11.7. Photograph of the SEM (Hitachi S-4800) with Oxford EDS probe.

11.8.2 Stripping

The fabrication of a novel wide-band gap semiconductor detector is expensive. It is imperative that such a detector is able to deliver many hundreds, if not thousands, of measurements before it degrades.

Thus, the detector needs to be reusable, which implies the necessity of removing the deposit after the measurement on it has been completed, in such a matter that the detector surface is not appreciably altered. This stripping also needs to be quantitative, so that there is no (alpha radiation) background buildup over time that would contribute to noise.

SEM-EDS analysis outlined above was performed on coupons that have experienced several deposition and stripping cycles, in order to determine the possible reusability. The success of a particular stripping run was judged by the degree to which the stripping removed the actinide elements, as well as whether excessive surface alteration occurred as a result of the stripping.

11.9 Experiment scheduling

The first step was to source the required chemicals and design the electrochemical cell—select the materials of the crucible and electrodes, design the lid and the

electrode holder, and make modifications to the furnace.

Once the cell was ready for experiments, a suitable deposition technique had to be selected—one that would be reasonably fast to deposit the required amount of material onto a coupon, yet without excessive dendritic formations or other features which would negatively impact adhesion. This selection of technique was done primarily with thorium analyte, since it was less expensive.

A change in coupon material also occurred at this point—a switch from stainless steel to nickel was made (driven by suggestion from Ohio State University researchers). A verification of feasibility of deposition onto this new material was made.

After the technique was semioptimized for thorium, uranium was studied to verify that this technique could be successfully used for uranium deposition as well.

Next, a full concentration spectrum (about 0.5–5 wt%) for uranium-only salt was covered, with salt samples and coupons collected and analyzed at each particular concentration point. A correlation of deposition time and concentration was done. The same was done for thorium-only salt.

Finally, several mixed salts containing both thorium and uranium with varying concentrations were prepared to provide insights into how one element might influence the deposition (particularly deposition time) of another. The experimental space (i.e. ranges of concentrations considered) is depicted in Figure 11.8, with intended collection of data points indicated.

Each shade of blue indicates a new set of experimental runs with progressively increasing concentrations in the direction of the arrows. A total of three sets with some 24 data points was envisioned to cover the experimental space.

11.10 Analyte salt synthesis

11.10.1 UCl_3 synthesis

Due to unavailability of commercial source of UCl_3, it was decided to produce it in the laboratory.

According to thermodynamic data (43), the reaction of uranium metal with either zinc chloride or iron chloride should produce uranium chloride:

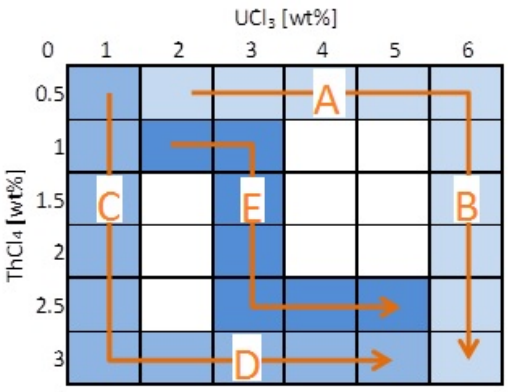

Figure 11.8. Experimental space with a three-stage collection of data points.

$$2U + 3ZnCl_2 \rightleftharpoons 2UCl_3 + 3Zn \qquad \Delta G_f(773\,K) = -242.8\,[kJ\,mol\,U^{-1}] \quad (11.3)$$

$$2U + 3FeCl_2 \rightleftharpoons 2UCl_3 + 3Fe \qquad \Delta G_f(773\,K) = -333.1\,[kJ\,mol\,U^{-1}] \quad (11.4)$$

The reaction with $ZnCl_2$ offers the advantage that Zn is molten at 500 °C (773 K), but solidifies around 420 °C (693 K). The desirable course of action therefore involves running the reaction at 500 °C, then lowering the temperature to around 400 °C and pouring the liquid salt out of the crucible while leaving behind the solidified Zn metal.

The reaction with $FeCl_2$ offers the advantage of achieving higher level of completion, and the possibility of easily separating iron if using a steel crucible and a magnet.

Both routes have been successfully explored in the laboratory and salts of approximately 20 wt % UCl_3 in LiCl-KCl eutectic were produced and used in later runs.

11.10.2 $ThCl_4$ synthesis

Due to unacceptable quality of commercial source of $ThCl_4$ (excessive moisture content), it was decided to produce it in the laboratory.

Similarly to the above case, the reaction of thorium metal with either zinc chloride or iron chloride should produce thorium chloride:

$$Th + 2ZnCl_2 \rightleftharpoons ThCl_4 + 2Zn \qquad \Delta G_f(773\,K) = -350.0\,[kJ\,mol\,Th^{-1}] \quad (11.5)$$

$$Th + 2FeCl_2 \rightleftharpoons ThCl_4 + 2Fe \qquad \Delta G_f(773\,K) = -470.3\,[kJ\,mol\,Th^{-1}] \quad (11.6)$$

The reaction with $FeCl_2$ was attempted first. Steel crucible was resting on top of a magnet, which was supposed to draw the newly resulting iron out of the salt. Thorium chips were added in a steel basket, which was rotated to promote mass transfer. After letting the reaction go overnight, the salt was poured out and analyzed. The $ThCl_4$ content was slightly lower than the desired value (18 instead of 20 wt%), however, the residual $FeCl_2$ content was high (1.6 wt%), signifying the reaction did not go to completion.

The amount of residual $FeCl_2$ caused significant corrosion of zirconium counter electrode in the subsequent run, demonstrating that the residual amount was unacceptably high.

A possible reason behind it was the blockage of thorium reactant by the developed sponge of iron that grew on and inside the basket as the reaction proceeded. Consequently, it was progressively harder for the $FeCl_2$ to diffuse to thorium and react, leaving some fraction of reactants unreacted. Not much iron was captured by the magnet, the vast majority was attached to the basket in the form of a large, low-density sponge.

The reaction with $ZnCl_2$ was attempted next, to remedy the shortcomings of the iron route. Powdered zinc metal was added to the mixture as well, to create a pool at the bottom where liquid zinc droplets would collect. Then, thorium was added in two fashions. First, nearly-stoichiometric amount of thorium was tossed freely into the alumina crucible to promote completion and to avoid any mass transfer limitation imposed by the steel basket. Then, similar amount of thorium was added in the basket (reaching the total of 2x stoichiometric amount) to ensure the remaining fraction of the $ZnCl_2$ was consumed as well. Then the temperature was lowered to 390 °C to achieve zinc solidification.

However, it was discovered that the salt was partially solidified as well (the 20 wt% $ThCl_4$ content apparently raises the original melting point of LiCl−KCl by more than 40 °C). Thus, the temperature was raised to 400 °C. At this temperature, both the salt and the zinc pool were liquid. Thorium content from the free toss likely ended up in the zinc pool, apparently lowering the melting point of Zn by more than 20 °C. It was decided to pour everything out, as zinc would easily separate out. The

analysis showed that the $ThCl_4$ content was slightly lower than the desired value (17 instead of 20 wt%).

The residual $ZnCl_2$ content was much lower than in the iron case (0.5 wt% vs. 1.6 wt%), but still somewhat higher than expected, given the excess of thorium metal available. Surprisingly, it was again noted that the basket was covered by a metallic sponge (zinc should have been liquid at those temperatures), which might have prevented thorium from completely reacting.

CHAPTER 12

RESULTS AND DISCUSSION

12.1 Deposition considerations

12.1.1 Analyte Concentrations

Similar to *Part I*, the *expected* and *measured* analyte concentrations are distinguished. The *expected concentration* is simply the prediction based on weighed amounts of added salts, whereas the *measured concentration* is the one determined by sampling the salt after the experiment and analyzing by ICP-AES.

The same moisture-related mechanism as explained in *Part I*, Section 6.1 is believed to be the reason behind considerable discrepancy between the *expected* and the *measured* concentration.

12.1.2 Deposition objectives

The analysis aims to provide near-real time results. This puts some constraint on the total time needed for the deposition step (as well as for the alpha particle counting step). The deposition should be reasonably fast, perhaps not lasting more than several minutes.

Analysis using SRIM (Stopping and Range of Ions in Matter) (93) was used to determine optimum deposit thickness for alpha spectroscopy measurements. A compromise between spectral broadening (which worsens with thicker deposit) and signal intensity (which improves with thicker deposit) had to be found—see Table 12.1.

The optimum thickness was found to be about 1 µm, which became the target thickness for all runs. At 1 µm, the spectral broadening is around 250 keV. This amount of broadening still permits the resolution of major thorium and uranium peaks, since differences in their energies are around those magnitudes or larger.

Assuming uniform coverage and theoretical density, by using Faraday's law ($Q =$

Table 12.1. Analysis using SRIM to determine optimum deposit thickness.

Thickness	Spectral broadening [keV]	Activity [Bq]
50 nm	8.0E+00	1.38E–01
500 nm	1.0E+02	1.38E+00
1 µm	2.5E+02	2.77E+00
5 µm	1.7E+03	1.38E+01

nzF) (90) the required amount of charge to reach target thickness is about 7 C for thorium and 9 C for uranium.

Uranium is well known to form dendrites on cathodes when electrorefined in molten salt (94, 95). Large dendritic structures would interfere with the alpha particle counting (they would shield alpha particles from reaching the detector, thus reducing the signal intensity and broadening the spectrum in comparison to uniformly layered deposit).

Thus, one of the objectives was to develop a deposition regime that minimizes dendritic formations and achieves a uniform layer instead. When morphology considerations outlined in Section 10.6.2 are compared with the requirement of depositing at large overpotential (to achieve diffusional currents, see Section 10.12.2), the prospect of avoiding dendrites is not very favorable, as outlined in (74): "Processes with low or medium i_0 will yield compact deposits at low overpotentials, while dendritic or spongy deposits are obtained at larger η."

12.1.3 Coupon material

Initially, stainless steel was used as a coupon material due to it being readily available, cheap, and easily machinable. Redox potentials for its major components (Fe, Ni, Cr) are also sufficiently anodic (noble) so that they do not oxidize and enter the solution during the electrodeposition of actinides.

However, the final Schottky contact (detector surface) of the semiconductor detector needs to be from a material other than stainless steel. The Ohio State University researchers have decided (later in the project) that nickel is a suitable candidate.

Consequently, nickel coupons are more appropriate for developing the deposition process. Later sets of deposition runs were thus done on nickel (high-temperature suitable low carbon alloy Ni-201). The surface of the nickel coupon was polished by a polishing tool prior to immersion to remove the surface oxide layer.

Both thorium and uranium form alloys with nickel (96, 97). The investigation therefore focused on the stripping phase as well, since the alloy formation might potentially complicate the removal of the actinide from the nickel matrix.

12.1.4 Raw data corrections

The novel analytical method calls for two variables to be extracted from the electrodeposition measurement—the total charge Q_{tot} and the deposition time t (see Section 10.12). In theory, either constant total charge Q_{tot} can be selected and variable t is observed as concentration is varied, or constant deposition time t can be selected and variable Q_{tot} is observed as concentration is varied.

Both approaches were investigated, but the constant t approach was quickly discarded due to practical reasons. It would be detrimental for the subsequent alpha particle counting if the deposits were of variable thickness, which is the case when vastly different amounts of charge were deposited. Thus, constant total charge was selected and deposition time became the variable of interest.

Under constant Q_{tot}, the hypothesis expects deposition time to be a function of concentration of actinide in the salt. In order to obtain reliable deposition times from RCA runs (which were the dominant ones, as will be revealed below), several transformations of the raw data (Q, t, c) was performed.

12.1.4.1 Charge corrections

Regarding Q, there are three corrections that were made: (a) the amount needs to be normalized to the same area (immersion depth) across various runs, (b) a contribution of the double-layer charging current is evaluated, (c) a fraction representing zirconium contribution is subtracted from the total faradaic charge.

An illustration of the process is displayed in Figure 12.1 for thorium. The process for uranium and the combined salts is essentially the same, with minor variations in (c), as described in corresponding sections.

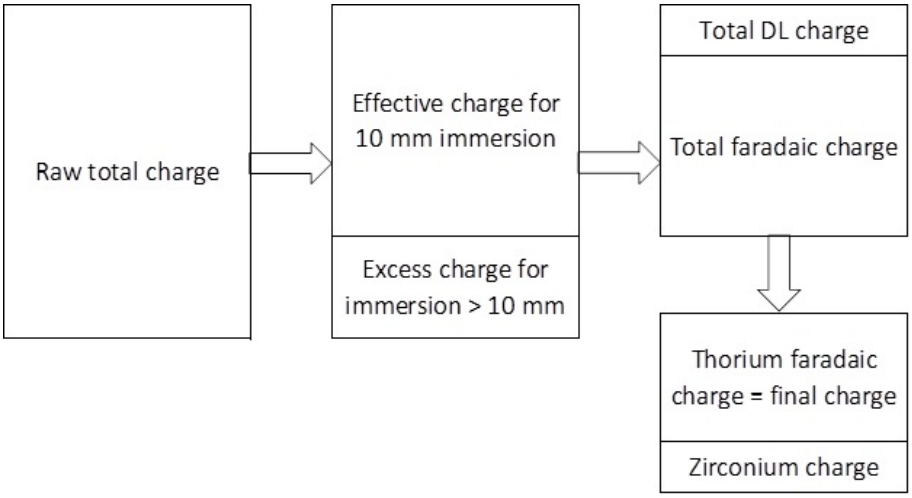

Figure 12.1. Process of obtaining the thorium charge from raw data.

(a) Although every effort is made to maintain constant (10 mm) immersion depth between runs, inadvertent variations of the immersion depth occasionally happen. To correct for this variation in cathode area, the raw charge (Q_{raw}) is multiplied by the ratio of the prescribed depth (h_{10mm}) and the actual depth (h_{actual}):

$$Q_{tot} = Q_{raw}\frac{h_{10mm}}{h_{actual}} \tag{12.1}$$

(b) The contribution of the double-layer charging current (which is generated during each potential step) can introduce error in the total amount of charge collected. The total charge is a sum of the charging current (i_c) and the faradaic current (i_f) (i.e. the current due to redox change of a chemical species), while only the faradaic current is of interest:

$$Q_{tot} = \int_0^t (i_c + i_f)dt \tag{12.2}$$

In order to estimate the contribution of i_c to the total amount, a comparison of the duration of the individual RCA segments (pulses and relaxations) and the duration of the double-layer charging is made. The double-layer charging is characterized by the cell time constant τ, where $t = 5\tau$ is the practical duration of the charging (see Section 10.1 for more details).

In the typical case ($\Delta E = 0.14$ V, $R_s = 0.5\ \Omega$, $C_d = 0.008$ F) the $5\tau \approx 20$ ms. In order to make this contribution negligible, the pulse/relaxation durations have to be at least an order of magnitude larger. Thus, the pulse duration is selected to be

200 ms. The relaxation duration is even longer (due to smaller overpotential applied, resulting in smaller driving force), typically one second. Under these conditions the double layer charging current contribution is negligible and no correction is applied.

(c) The last correction to charge is made based on the SEM-EDS analysis of the deposit. Analyte and zirconium weight percentages given by the EDS probe are converted into their atomic percentages using the inversed ratio of their respective molecular masses. Any difference in the number of electrons required for reduction is accounted for as well.

Thus, zirconium contribution to the total charge is estimated and can be subtracted from the total. The result is a fraction of the total charge attributable solely to the analyte. The specific equations for each case are given in the appropriate sections below.

12.1.4.2 Deposition time corrections

Regarding t, there are two corrections that were made: (a) normalizing the deposition time for exactly 9 C deposition; and (b) averaging the results of multiple runs to arrive at a single value of deposition time for a particular concentration.

(a) The normalization is achieved by multiplying the raw deposition time t_{raw} by the ratio of the prescribed total charge (9 C) and actual total charge specific to thorium $Q_{tot,Th}$:

$$t = t_{raw} \frac{Q_{tot}}{Q_{tot,Th}} \tag{12.3}$$

(b) Typically there are two deposition runs per concentration. A weighted average is used, based on how well the deposition followed the idealized RCA pathway. The idealized pathway is defined as follows.

Each RCA segment should show between 20 and 65 % stripping. If all segments (usually there are about 4 segments) fulfill this criteria, then the run is considered *successful*. If one segment deviates from this criteria (typically the first one shows less than 20 % stripping) but the rest is acceptable, then the run is considered *satisfactory*. When more than one segment deviates appreciably, the run is considered *sub-optimal*.

Consequently, when two *successful* runs (or two *satisfactory* runs) are encountered, a simple average is used. If one *successful* and one *satisfactory* run are encountered,

a 60/40 weight is assigned. When one *successful* and one *sub-optimal* run are encountered, a 80/20 weight is typically assigned. Runs where only *sub-optimal* results were gained are excluded.

12.1.4.3 Concentration corrections

Expected concentrations (predictions based on weighed amounts added, see Section 6.1) proved to be grossly off in virtually all cases when compared to the measured concentrations determined by ICP-AES.

Consequently, expected concentrations were never used in calculations and were always replaced by measured ones. These amounts determined by ICP-AES were consistent when multiple samples of the same salt were collected, and can be regarded as sufficiently accurate.

12.2 Thorium

12.2.1 Cyclic voltammetry on coupons

In the large-area coupon setting encountered here (in contrast to thin rod setting treated later), the CV serves primarily a diagnostic function. It is used prior to the actual deposition and tests several parameters:

- The reference electrode stability (invariance of peak potential with time).
- Immersion depth verification (peak current in the expected range).
- Electrochemical equilibrium (invariance of peak current with time).

CV is also used to guide the selection of deposition parameters (see the next section).

The reduction/oxidation behavior of thorium was investigated on both stainless steel and nickel coupons. According to literature (24, 98–101), the reduction should be a one-step, four electron transfer [Th^{4+}/Th]. The CV for both materials is displayed in Figure 12.2.

The thorium reduction peak on stainless steel is close to -2.4 V (vs. [Ag/100% AgCl]). The anodic limit for this electrode is the onset of iron oxidation around -1.5 V. Single prominent reduction and oxidation peaks occur on stainless steel, with some indication of minor overlapping peaks.

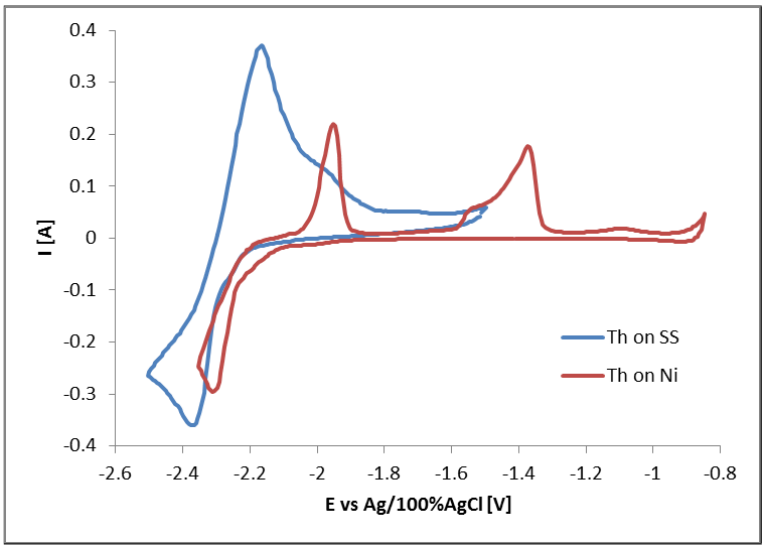

Figure 12.2. CV of $ThCl_4$ in LiCl−KCl on large surface electrodes. $A = 4$ cm^2, $T =$ 773 K, $\nu = 50$ mV s^{-1}, $c(ThCl_4) = 1.5$ wt%. WE: SS or Ni, CE: Zr, RE: [Ag/AgCl].

The nickel substrate shows some alloying tendencies. The thorium reduction peak is shifted anodically to about -2.3 V, and there are two major peaks during the oxidation part of the cycle. The Ni/Th binary phase diagram confirms the possibility of intermetallic formation between thorium and nickel (96). The anodic limit for this electrode is the onset of nickel oxidation around -0.9 V. This increase in range of the electrochemical window is useful to ensure that all deposited thorium can be anodically stripped, as shown in the stripping section (see Section 12.2.4.4).

12.2.2 Chronoamperometry

Initial deposition runs on stainless steel were conducted using standard CA, i.e., constant potential deposition. Results from these runs are summarized in Table 12.2. CV was used to identify the on-set potential for deposition (around -2.20 V). Then, deposition under constant overpotentials in a range between -2.28 V and -2.70 V was realized. Deposits from individual runs were analyzed using SEM-EDS after being rinsed in deionized water to dissolve the solidified salt residue. Below is the summary of the experience:

Samples generated from large overpotentials ($E <$ -2.40 V) showed excessive dendritic formations and/or poor adherence of the deposit to substrate. This is in

Table 12.2. Results of CA runs of thorium on stainless steel.

Run #	Applied potential [V]	Comment
1	-2.40	Deposit flaked off during rinsing
2	-2.70	Deposit flaked off during rinsing
3	-2.70	Current spikes during deposition, dep. flaked off
4	-2.28	Deposit located in scarce regions, deposition time ≈10 min
5	-2.28, -2.32	Deposit covers most of surface, deposition time ≈20 min
7	-2.28, -2.33	Deposit covers most of surface, dendrites, deposition time ≈23 min
8	-2.28, -2.32	Deposit covers most of surface, deposition time ≈7 min

agreement with the theory as discussed previously in Sections 10.6.2 and 12.1.2.

A composite two-step deposition with two different overpotentials (initially E = -2.28 V, then switch to E = -2.32 V) was attempted to diminish the amount of dendrites and to shorten the deposition time—see Figure 12.3. Dendrite growth was suppressed, however, they still existed—see Figure 12.4.

Except for Run #8 (see Table 12.2), the samples took more than 10 min to collect the required amount of material, effectively rendering the method too slow for strictly real-time analysis. Nevertheless, the suppression of dendrites and generally good surface coverage by thorium globules of about 1 µm thickness (target thickness) yielded overall satisfactory results in the later runs.

Figure 12.5 displays SEM picture of one such run that shows no dendrites. Brighter, globular formations 1–2 µm large (often interconnected) are thorium deposits, whereas a darker bare spot on the right side reveals the iron substrate—rendering thorium distribution non-uniform with multiple regions bare of thorium content.

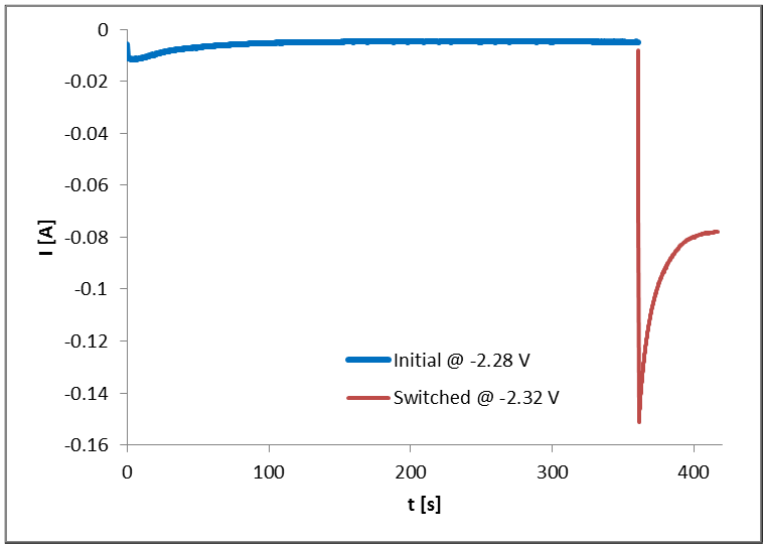

Figure 12.3. CA of thorium deposition on stainless steel (Run #8). Current transient occurred after the potential was switched. The current remained unusually high at this potential. Initial 2 C deposited at -2.28 V, additional 5.2 C deposited at -2.32 V. $T = 773$ K, $c(ThCl_4) = 2.2$ wt%.

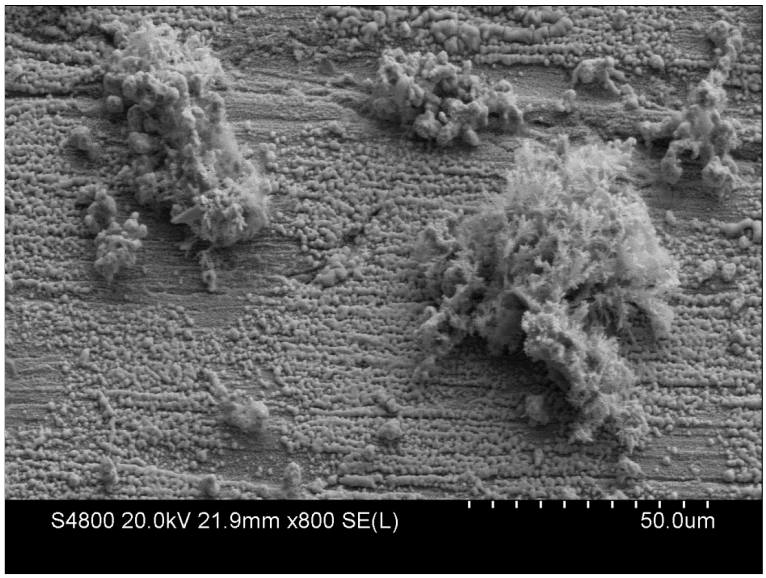

Figure 12.4. SEM picture of thorium deposit on stainless steel using CA. Dendritic formations of enormous sizes relative to the rest of the deposit were frequently encountered. Initial 2 C deposited at -2.28 V, additional 6 C deposited at -2.33 V. $T = 773$ K, $c(ThCl_4) = 2.2$ wt%.

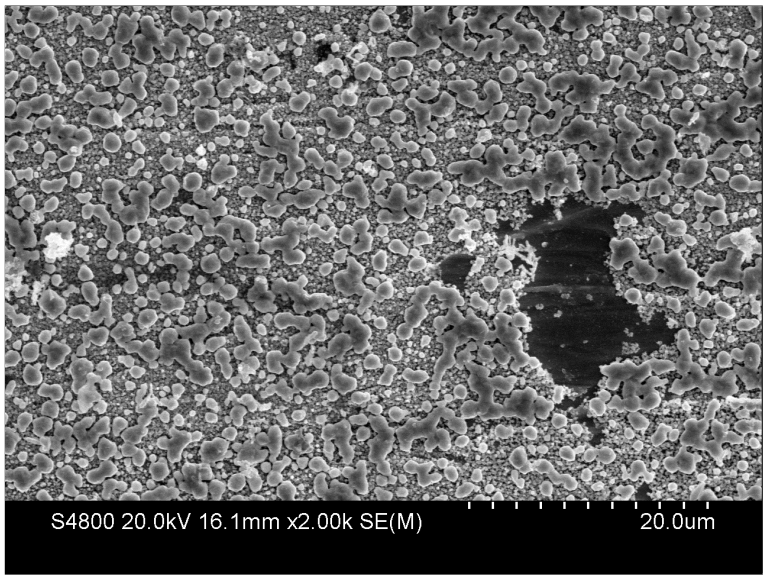

Figure 12.5. SEM picture of thorium deposit on stainless steel using CA. Initial 2 C deposited at -2.28 V, additional 5 C deposited at -2.32 V. $T = 773$ K, $c(ThCl_4) = 2.2$ wt%.

The trend is evidenced further on a different SEM picture from the same run, displayed in Figure 12.6. It shows EDS map overlay with individual elemental maps. Iron intensity is larger in portions where the absence of thorium deposit does not shield the iron signal. Still in thorium regions the iron signal is not completely lost. This signifies that the deposit is thin enough to permit some fraction of the electron beam to reach the iron underneath it.

This becomes important in the elemental composition reading—a large amount of substrate signal is always present, even if there is a complete (yet reasonably thin) coverage of the surface. Figure 12.7 contains a plot of such composition.

It is noted that each picture was selected to contain some contrasting information (bare spot, dendrite, another abnormality), while significant portions of the surface were covered without distinct abnormalities.

Zirconium content was nearing the detection limit of EDS in the layered regions of the deposit. It was highly localized to dendritic regions, where it accounted for about 12 at%. A possible explanation revolves around the fact that electric fields are concentrated around sharp curvatures, causing these regions to experience higher current densities. $ZrCl_4$ content in the salt was below detection limit of ICP-AES.

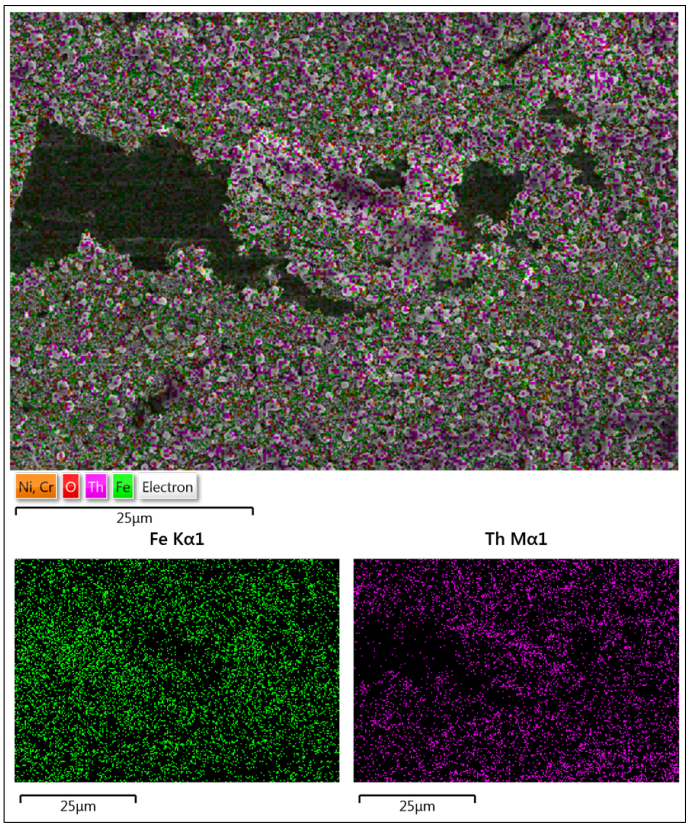

Figure 12.6. EDS map of thorium deposit on stainless steel using CA. Initial 2 C deposited at -2.28 V, additional 5 C deposited at -2.32 V. $T = 773$ K, $c(ThCl_4) = 2.2$ wt%.

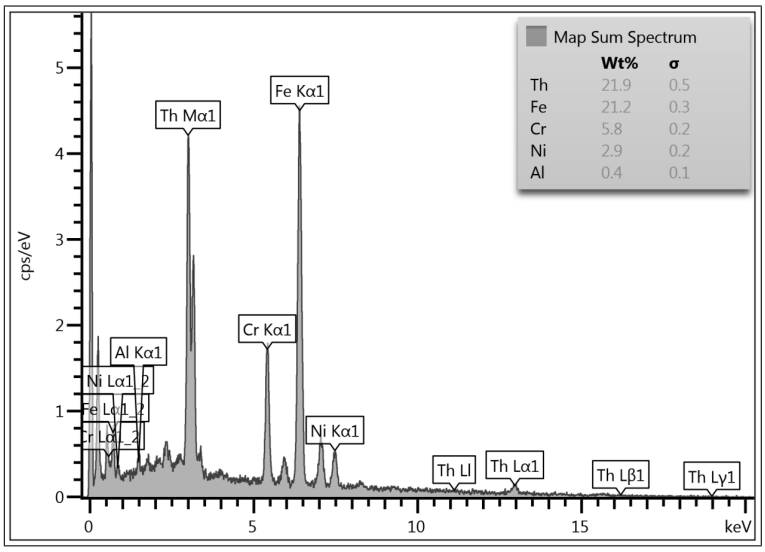

Figure 12.7. EDS map spectrum of Figure 12.6. Iron, chromium, and nickel are compounds of stainless steel substrate.

12.2.3 Chronopotentiometry

The constant current deposition regime was investigated due to the allure of shorter duration of the deposition, and easier handling of the resulting CPs.

An initial run was performed, where the current was selected sufficiently low (to promote compact deposit formation and suppress dendrites), while achieving the duration of the deposition comparable to CA. The progress of the run is shown in Figure 12.8, while the summary is given in Table 12.3.

The run (Run #6) proved to be unsuccessful. Although the potential remained at about -2.29 V (expected value for thorium only deposition) all the time, the deposit was very poor, with very scarce regions of actual thorium deposits. Since this was the initial run and quite small current was applied—so that (if successful) larger currents would be attempted in later runs—it became clear that there is little reason to continue in this direction. Larger currents would only bring more challenges. They would promote dendritic growth or even trigger lithium codeposition (if thorium alone could not accommodate the flow of charge).

Consequently, the CP method was abandoned and focus was put to improve the CA method (Runs #7, #8). Simultaneously, literature was consulted to find an alternative superior in performance to a simple CA.

12.2.4 Repeating chronoamperometry

The alternative superior in performance to a simple CA was found in RCA. RCA alternates between two set potentials with rapid succession. The first potential (E_{pulse}) is cathodic and promotes deposition, while the second potential (E_{relax}) is anodic and promotes deposit dissolution. The partial dissolution ensures that only the stable portion of deposit remains in place. More information about RCA is found in Section 10.9.2.

Of interest is also the fact that the deposition time was significantly shortened compared to the other techniques. Usually less than 2 min are required to deposit given amount of material. Table 12.4 summarizes the typical parameters used in RCA for both stainless steel and nickel coupons.

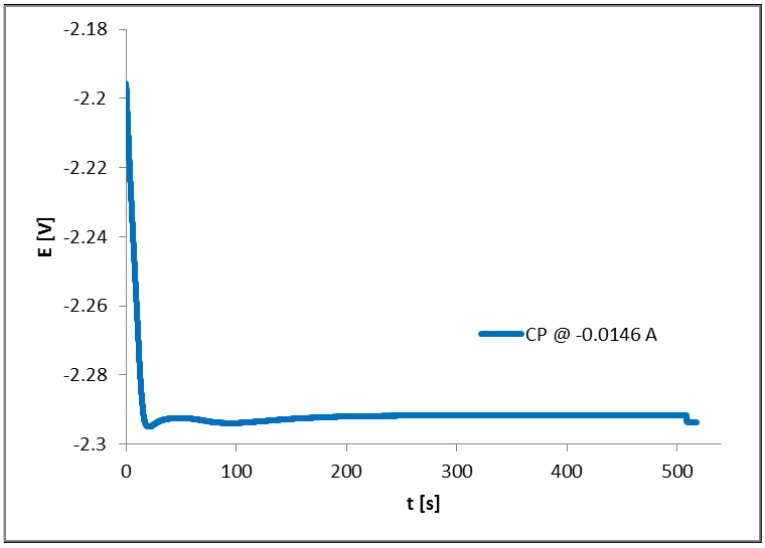

Figure 12.8. CP of thorium deposition on stainless steel (Run #6). I = -0.0146 A, T = 773 K, $c(ThCl_4)$ = 2.2 wt%

Table 12.3. Results of CP runs of thorium on stainless steel.

Run #	Applied current [A]	Comment
6	-0.0146	Deposit located in scarce regions, deposition time ≈9 min

Table 12.4. Typical parameters of RCA runs for deposition of thorium on stainless steel and nickel.

Parameter	Stainless steel Runs 10-14	Nickel Runs 15-17	Nickel Runs 43-61
E_{pulse} [V]	-2.38	-2.24 to -2.33	-2.40
E_{relax} [V]	-2.26 to -2.28	-2.10	-2.08 to -2.15
t_{pulse} [s]	0.2	0.2	0.2
t_{relax} [s]	2.0	2.0	1.0

12.2.4.1 Nucleation mode

The validity of using RCA depends on the nucleation mode. A characteristic three-region nucleation response using CA is a diagnostic tool for determining the nucleation mode (102–104). For unknown reasons this behavior was not replicated in the setup used here even when setup described in literature was followed.

Many different overpotentials were selected along with two different cathode materials (2 mm diameter Ni or W rods), however the result was always a simple cottrellian decay of current with no maximum due to nucleation—see Figure 12.9.

The only relevant literature available is the work of Cassayre (100) which determined progressive nucleation of thorium on tungsten. However, tungsten is inert as opposed to the reactive nickel electrode which was used. Furthermore, the concentration of thorium was very small (0.2 wt% $ThCl_4$), whereas concentration in this setup was at minimum 1 wt% $ThCl_4$. The validity of this reference is therefore very limited.

Since the experiment with nucleation on tungsten followed closely the one reported (100), the only difference being the higher thorium concentration, a conclusion is drawn that the nucleation at such a high concentration is a fast process that cannot be captured. This is translated to the (reactive) nickel electrode, where no literature is available to compare to.

Furthermore, the nucleation mode can be estimated from the SEM micrographs. Figures 12.5 (stainless steel) and 12.17 (nickel) show a uniform size of the nuclei. This hints at instantaneous nucleation, where all the nuclei are created at once and belong to the same generation, therefore being uniform in size.

12.2.4.2 Stainless steel coupons

Based on CV results, the cathodic potential was selected to be at least the peak potential of the analyte. This assures that the deposition happens under diffusion-limited conditions. The anodic potential was selected around the onset of analyte reduction current in CV plot. This makes a considerable fraction of the deposit (optimum was found around 40 wt%) dissolve back into solution in each step.

The first 30 s of a representative current transient for the stainless steel coupon

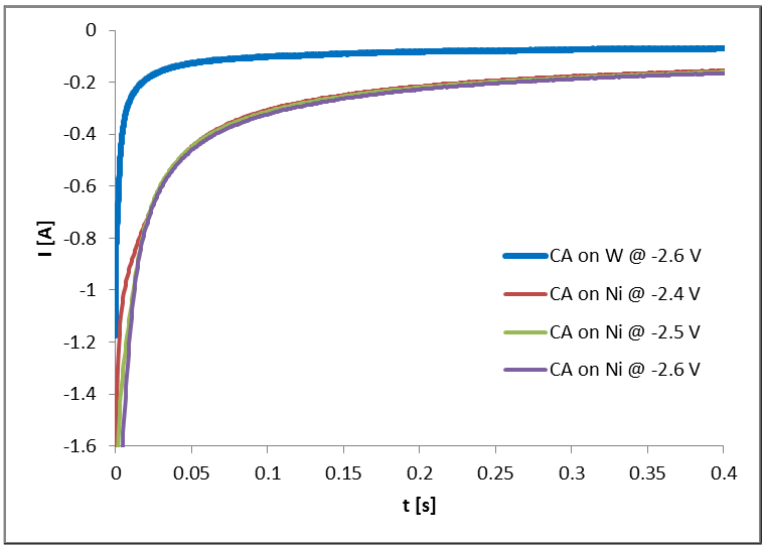

Figure 12.9. CAs of thorium deposition on tungsten and nickel with no nucleation regions visible. $T = 773$ K, W: $c(ThCl_4) = 1.35$ wt%, Ni: $c(ThCl_4) = 2.22$ wt%

is shown in Figure 12.10. An accompanying evolution of charge in time is shown in Figure 12.11.

SEM-EDS pictures of deposits created with this method demonstrated usually excellent uniformity and minimal dendritic formations. For the stainless steel coupon, a run with the following parameters is presented: E_{pulse} = -2.38 V, E_{relax} = -2.28 V, $c(ThCl_4) = 1.5$ wt%. Figure 12.12 shows the SEM picture, Figure 12.13 shows the EDS map overlay of the same picture, and Figure 12.14 gives the elemental composition measured via EDS.

The SEM picture (Figure 12.12) displays completely interconnected rows of globules (about 1 µm thick if spherical), which is the thorium deposit as confirmed by the EDS. There are no significant dendrite structures. The underlying iron substrate is only scarcely seen on the SEM due to good deposit coverage.

The EDS map (Figure 12.13) serves as a reminder that the deposit is fairly thin, since signal from the iron is still able to penetrate through the thorium layer and show up. According to Castaing's formula (see Equation 10.18 in Section 10.11), the maximum depth from which the chemical information is gathered is approximately:

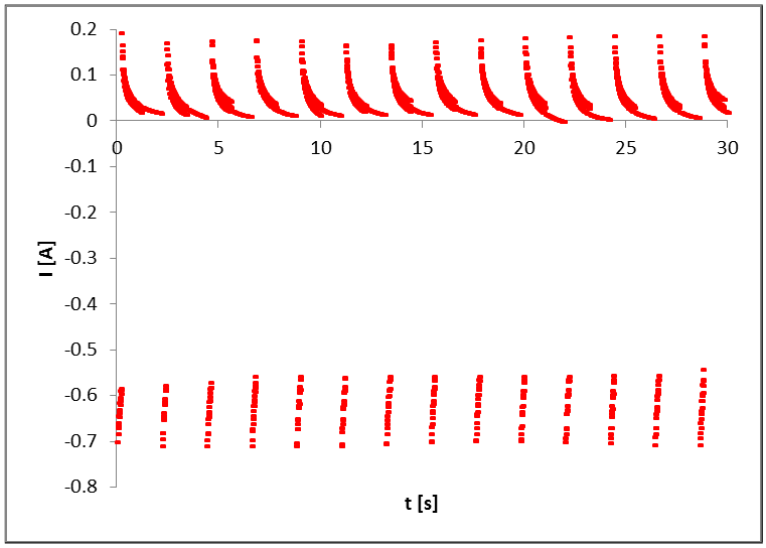

Figure 12.10. Section of the RCA current transient for thorium on stainless steel. E_{pulse} = -2.38 V, E_{relax} = -2.26 V, $A = 4$ cm^2, $T = 773$ K, $c(ThCl_4) = 1.5$ wt%.

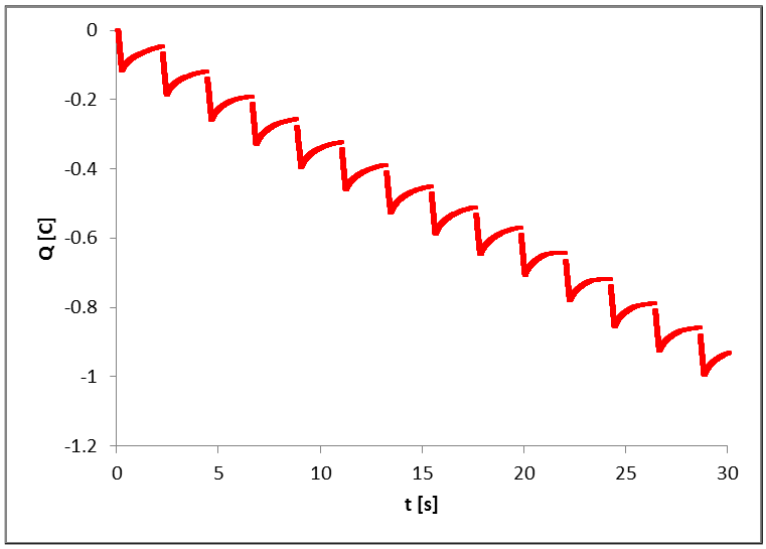

Figure 12.11. Section of the RCA deposition evolution with time for thorium on stainless steel. E_{pulse} = -2.38 V, E_{relax} = -2.26 V, $A = 4$ cm^2, $T = 773$ K, $c(ThCl_4) = 1.5$ wt%.

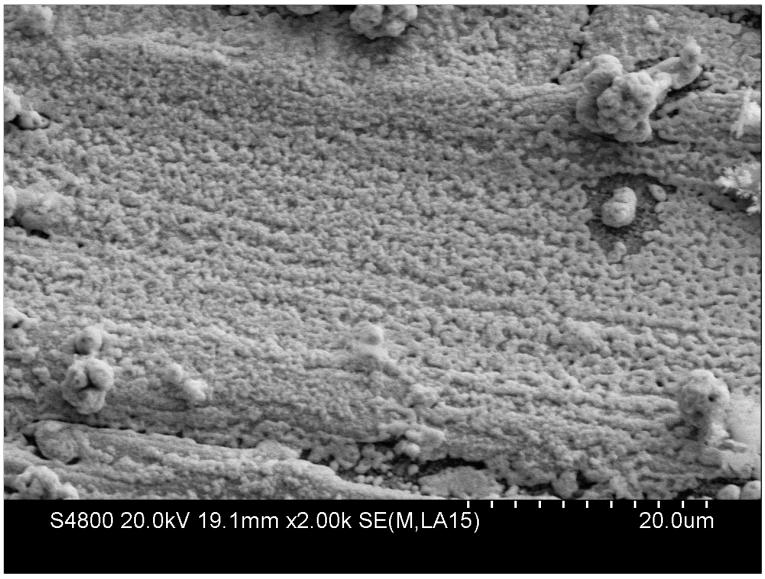

Figure 12.12. SEM picture of thorium deposit on stainless steel using RCA. E_{pulse} = -2.38 V, E_{relax} = -2.28 V, T = 773 K, $c(ThCl_4)$ = 1.5 wt%.

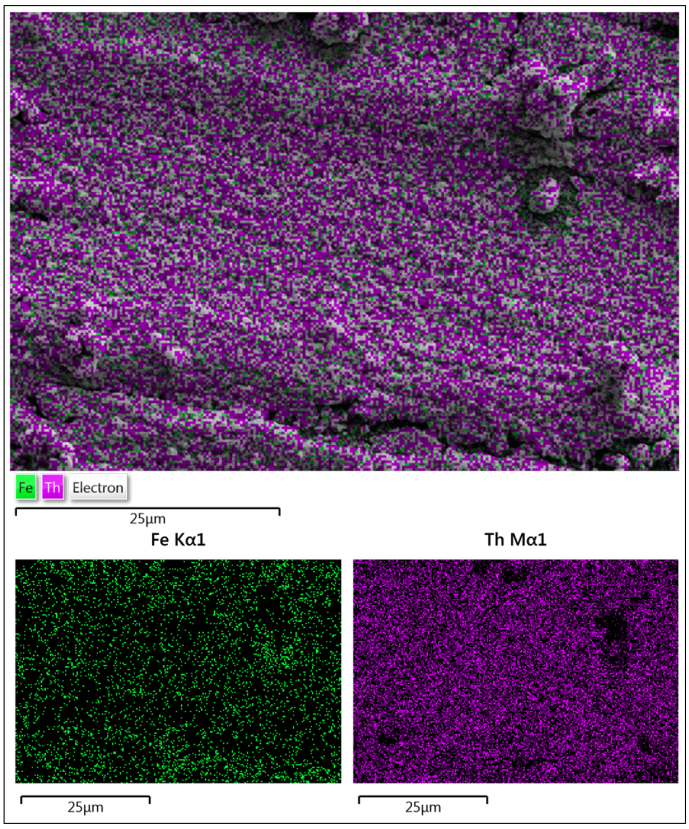

Figure 12.13. EDS map of Figure 12.12. E_{pulse} = -2.38 V, E_{relax} = -2.28 V, T = 773 K, $c(ThCl_4)$ = 1.5 wt%.

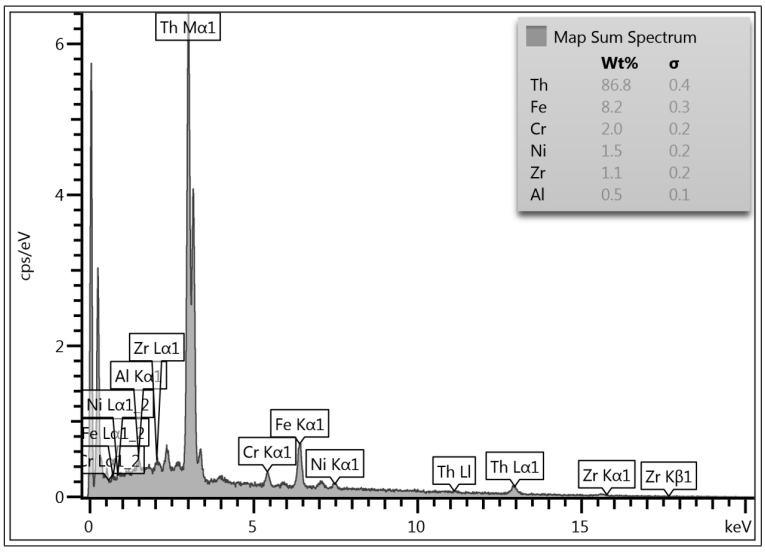

Figure 12.14. EDS map spectrum of Figure 12.13. E_{pulse} = -2.38 V, E_{relax} = -2.28 V, T = 773 K, $c(ThCl_4)$ = 1.5 wt%.

$$z_{max} = 0.033(E_{acc}^{1.7} - E_{em}^{1.7})\frac{M}{\rho Z} \tag{12.4}$$

$$z_{max} = 0.033(20^{1.7} - 2.991^{1.7})\frac{232}{11 \times 90} = 1.2\,[\mu m] \tag{12.5}$$

which suggests the thorium layer is not thicker than 1.2 µm.

The elemental composition (Figure 12.14) reveals—besides the thorium deposit—the usual composition of stainless steel plus some minor amount of zirconium.

12.2.4.3 Nickel coupons

The first 30 s of a representative current transient for the nickel coupon is shown in Figure 12.15. An accompanying evolution in time is shown in Figure 12.16.

Figure 12.17 displays a typical SEM picture obtained from a run of the following parameters: E_{pulse} = -2.24 V, E_{relax} = -2.10 V, $c(ThCl_4)$ = 1.5 wt%. Interconnected globules of thorium cover most of the surface. Figure 12.18 shows another picture from the same run with EDS map overlay. In this figure, the thorium signal is not exclusively restricted to globular formations, which suggests an alloy formation in addition to pure thorium-deposit regions. Figure 12.19 shows the approximate elemental composition measured via EDS, some minor amount of zirconium is codeposited.

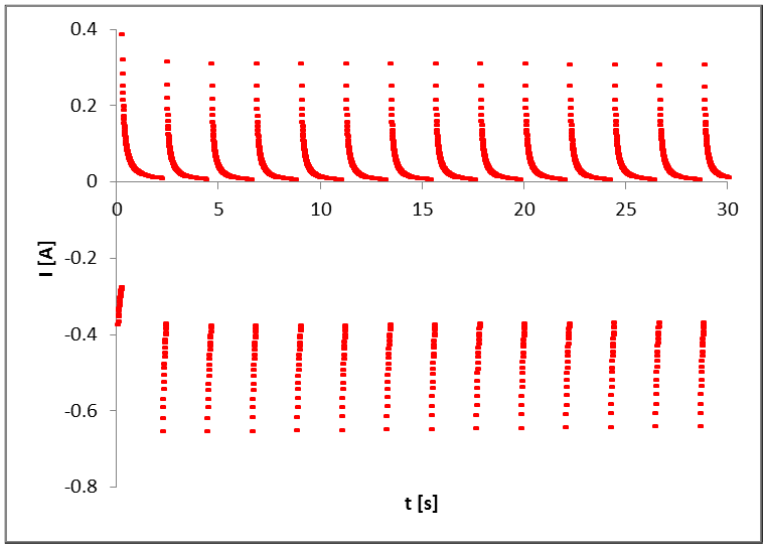

Figure 12.15. Section of the RCA current transient for thorium on nickel. E_{pulse} = -2.24 V, E_{relax} = -2.10 V, $A = 4$ cm^2, $T = 773$ K, $c(ThCl_4) = 1.5$ wt%.

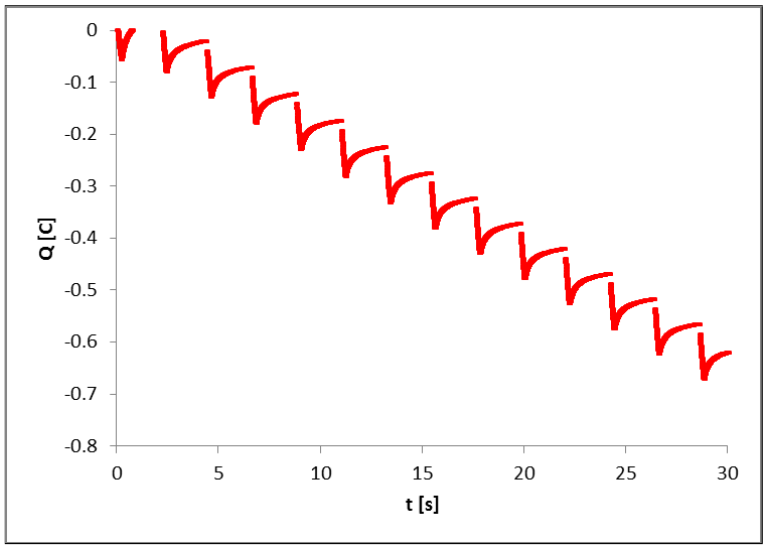

Figure 12.16. Section of the RCA deposition evolution with time for thorium on nickel. E_{pulse} = -2.24 V, E_{relax} = -2.10 V, $A = 4$ cm^2, $T = 773$ K, $c(ThCl_4) = 1.5$ wt%.

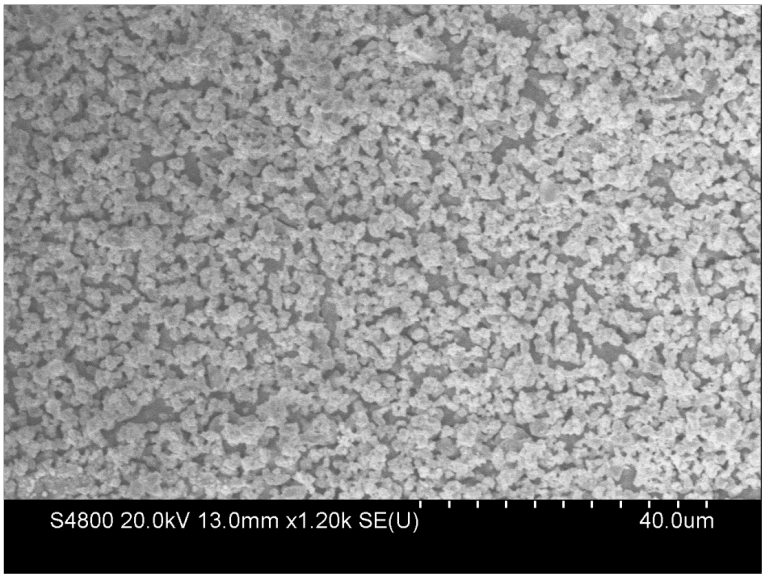

Figure 12.17. SEM picture of thorium deposit on nickel using RCA. E_{pulse} = -2.24 V, E_{relax} = -2.10 V, T = 773 K, $c(ThCl_4)$ = 1.5 wt%.

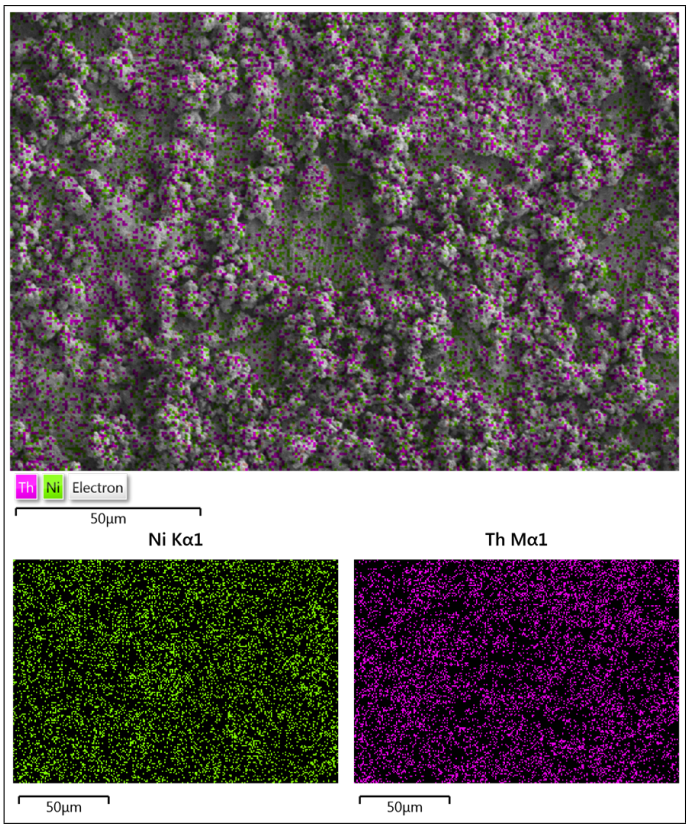

Figure 12.18. EDS map of Figure 12.17. E_{pulse} = -2.24 V, E_{relax} = -2.10 V, T = 773 K, $c(ThCl_4)$ = 1.5 wt%.

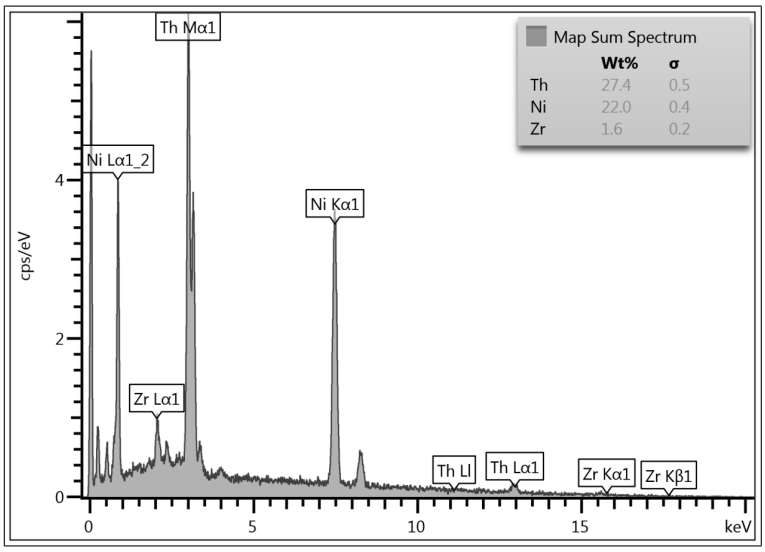

Figure 12.19. EDS map spectrum of Figure 12.18. E_{pulse} = -2.24 V, E_{relax} = -2.10 V, $T = 773$ K, $c(ThCl_4) = 1.5$ wt%.

An estimate of the deposit thickness—based on the observation that nickel signal is not lost below thorium deposit—can again be made using Castaing's formula. By using the same parameters like in Equation 12.5, the formula suggests the deposit is again not thicker than 1.2 µm. However, due to thorium being partially alloyed with nickel the accuracy of such estimate is limited.

12.2.4.4 Stripping

Due to concerns about the reactive nature of nickel substrate, stripping of the deposit was perform to investigate possible difficulties with reusability of the detector surface. The surface is required to not alter appreciably during stripping, while all deposit must be stripped off to eliminate alpha particle background (see Section 11.8.2 for more details).

Stripping was done under CA conditions, initially at -1.00 V, then -0.88 V, then -0.78 V; until equivalent amount of charge was passed to equal out the previously deposited amount (7 C). SEM-EDS analysis of the stripped coupon found no appreciable surface alterations—see Figure 12.20.

The most prominent features are parallel valleys and ridges, which are the characteristic result of initial polishing, and thus were there prior to deposition. Their

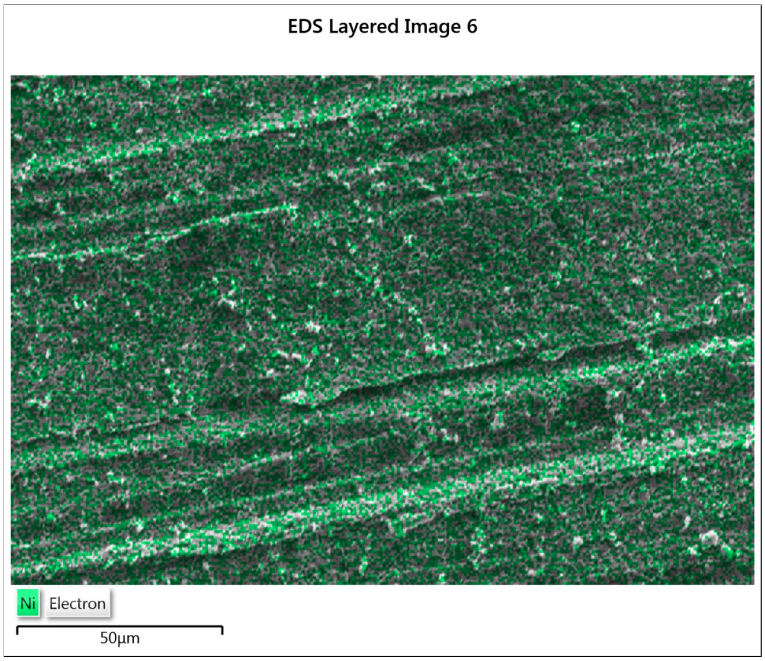

Figure 12.20. EDS map of nickel surface after thorium RCA deposition and subsequent stripping. E_{pulse} = -2.33 V, E_{relax} = -2.08 V, then dissolution using CA initially at -1.00 V, then -0.88 V, then -0.78 V until reaching 7 C total charge. $T = 773$ K, $c(ThCl_4) = 1.5$ wt%.

presence indicates that no significant surface alteration occurred as a result of the stripping procedure. The EDS elemental composition did not detect any thorium (or zirconium) residue.

12.2.4.5 Deposition time correlation

The transformation of the raw data (Q, t, c) outlined in Section 12.1.4 was performed. The charge Q was adjusted for immersion depth, and zirconium codeposition. The deposition time t was normalized for constant value of Q, and averaged over multiple runs when appropriate. The concentration c was determined by ICP-AES.

Regarding the correction to charge based on the SEM-EDS analysis of the deposit: thorium and zirconium weight percentages given by the EDS probe were converted into their atomic percentages using the inversed ratio of their respective molecular masses.

Since both thorium and zirconium reduction mechanism involves four electrons, zirconium atomic content directly translates into the amount of charge it used up.

This zirconium charge is therefore subtracted from the total to arrive at total charge specific to thorium:

$$Q_{tot,Th} = Q_{tot} - Q_{tot} \times (\text{Zr [at\%]}) \tag{12.6}$$

A correlation of the deposition time with concentration was constructed. Table 12.5 shows the data points, while Figure 12.21 plots those data points and adds the expected fit, which is of the power type $y = ax^b$.

12.3 Uranium

12.3.1 Cyclic voltammetry on coupons

Similar to thorium case, in the large-area coupon setting the CV served primarily a diagnostic function and was used to guide the selection of parameters for deposition.

The reduction/oxidation behavior of uranium was investigated on nickel coupon. According to literature (105–108), uranium has two stable oxidation states in the salt: 3+ and 4+. The reduction is a two-step process, exchanging one [U^{4+}/U^{3+}] and three [U^{3+}/U] electrons, respectively. A typical CV is displayed in Figure 12.22.

The first [U^{4+}/U^{3+}] reduction peak is overshadowed by the onset of nickel oxidation around -0.9 V (vs. [Ag/100%AgCl]), which is the anodic limit for this electrode. The second [U^{3+}/U] reduction peak occurs around -2.25 V. It is accompanied by a sharp stripping peak during the oxidation part of the cycle. The oxidation part shows two other peaks (around -1.4 V and -1.1 V), which might be the result of de-alloying. The Ni/U binary phase diagram confirms the possibility of intermetallic formation between uranium and nickel (97).

12.3.2 Repeating chronoamperometry

Since RCA has shown superior results compared to CP and CA during thorium runs, it was the only method pursued in the uranium runs that followed. Similarly, as stainless steel coupons have been replaced by nickel ones at the request of the Ohio State University researchers, only deposition on nickel was studied.

Table 12.6 summarizes the parameters used for uranium deposition on nickel. The relaxation period has been shortened from 2 s to 1 s in comparison to earlier thorium runs, in an effort to shorten the overall deposition time further.

Table 12.5. Deposition time vs. concentration correlation of thorium on nickel (normalized for 9 C deposition).

Run #	$c(ThCl_4)$ [wt%]	Deposition time [s]
56+57	0.46±0.01	307±1
44+45	1.45±0.05	118±2
58+59	1.89±0.01	98±1
46+47	2.01±0.06	110±8
48+49	2.13±0.03	100±20
50+51	2.54±0.04	95±8
60+61	2.68±0.05	91±8
52+53	3.17±0.01	80±9
54+55	3.31±0.06	75±22

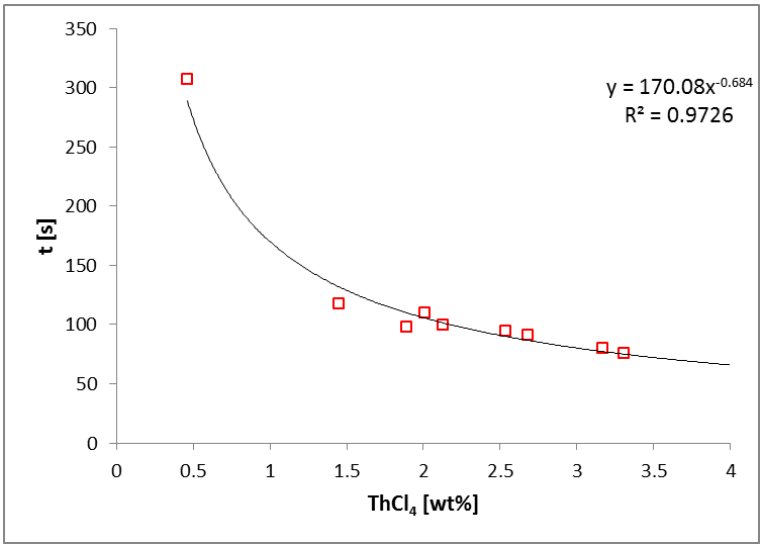

Figure 12.21. Deposition time vs. concentration correlation for thorium on nickel (normalized for 9 C deposition).

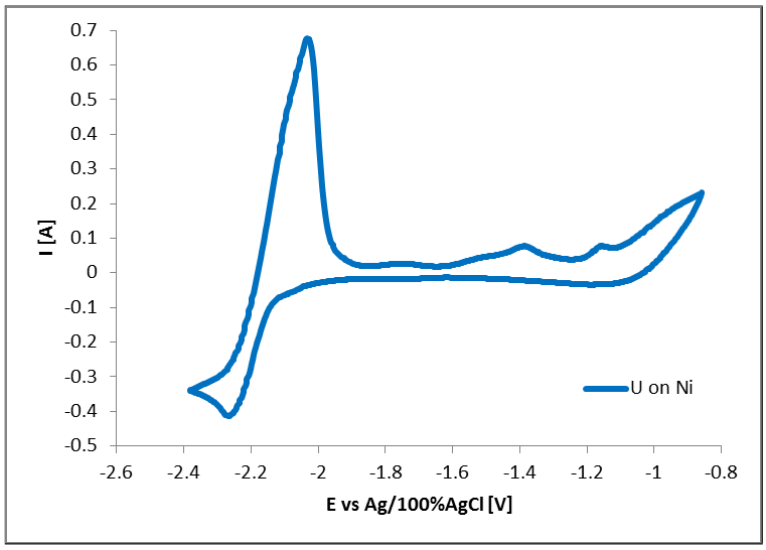

Figure 12.22. CV of UCl_3 in LiCl−KCl on large surface electrode. $A = 4$ cm^2, $T = 773$ K, $\nu = 200$ mV s^{-1}, $c(UCl_3) = 1.6$ wt%. WE: Ni, CE: Zr, RE: [Ag/AgCl].

Table 12.6. Typical parameters of RCA runs for deposition of uranium on nickel.

Parameter	Nickel
	Runs 18-41
E_{pulse} [V]	-2.33
E_{relax} [V]	-2.00 to -2.21
t_{pulse} [s]	0.2
t_{relax} [s]	1.0

12.3.2.1 Nucleation mode

As already mentioned in the thorium section (see Section 12.2.4.1), the validity of using RCA depends on the nucleation mode. A characteristic three-region nucleation response using CA was sought. Similar to the thorium case, for unknown reasons this behavior was not replicated in the setup used.

Many different overpotentials were selected along with two different cathode materials (2 mm diameter Ni or W rods), however the result was always a simple cottrellian decay of current with no maximum due to nucleation—see Figure 12.23.

The only relevant literature available is the work of Serrano (109) which deter-

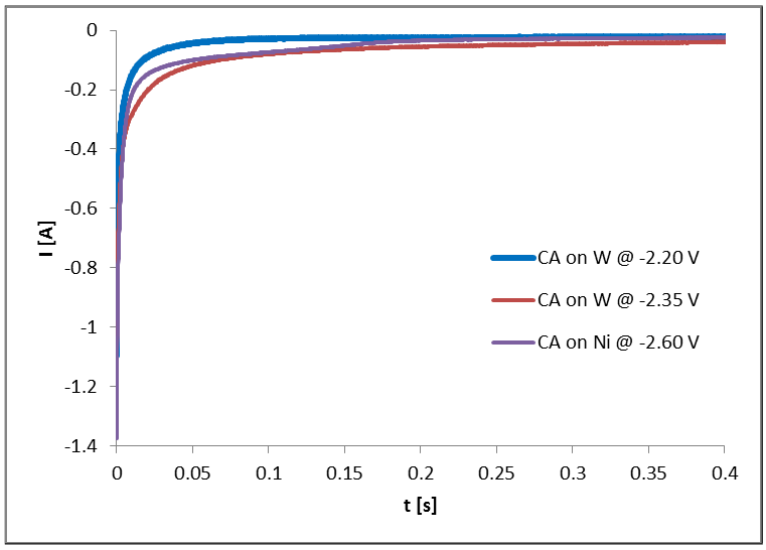

Figure 12.23. CAs of uranium deposition on tungsten and nickel with no nucleation regions visible. $T = 773$ K, $c(UCl_3) = 1.57$ wt%.

mined instantaneous nucleation of uranium in NaCl−KCl at 670 °C on glassy carbon.

Apart from a different solvent and temperature, the glassy carbon electrode is inert as opposed to the reactive nickel electrode used. Furthermore, the concentration of uranium was very small (0.4 wt% U), whereas concentration in this setup was at minimum 1.5 wt% UCl_3. The validity of this reference is therefore very limited.

The nucleation mode can also be estimated from the SEM micrographs as will be shown in the following section. A situation where uniform sizes of the nuclei are generated suggests instantaneous nucleation (all nuclei are created at once and belong to the same generation, thus being uniform in size).

However, as also discussed in the following chapter, surface features of uranium on nickel seen under SEM are often misleading and only after the EDS probe is applied the real picture emerges. Therefore, the estimation of nucleation mode via SEM is regarded as inconclusive.

12.3.2.2 Nickel coupons

Due to similar redox potentials of thorium and uranium, the uranium deposition on nickel was performed with relatively similar parameters. The first 30 s of a representative current transient for the nickel coupon is shown in Figure 12.24. An

accompanying evolution of charge in time is shown in Figure 12.25.

Figure 12.26 displays a typical SEM picture obtained from a run of the following parameters: E_{pulse} = -2.33 V, E_{relax} = -2.19 V, $c(UCl_3)$ = 0.9 wt%. Much different situation in comparison to thorium deposition is seen. It appears that uranium is deposited in isolated, stick-like formations with preferred crystallographic direction (instead of globular deposits seen in thorium case). The nucleation mode based on this picture suggests instantaneous nucleation, due to uniform size of apparent nuclei of uranium deposit. Some minor, flat dendritic formations can also be seen on careful examination. Nevertheless, it appears like most of the surface is not covered by the deposit, which would be a setback in comparison to thorium, which produced deposit with good coverage.

The situation changes when the EDS map overlay is displayed over the SEM picture, as is done in Figure 12.27. Uranium coverage is not limited to the stick-like formations, instead is rather uniform across the whole region. Nickel substrate is also uniformly distributed. This invalidates the nucleation mode assumption discussed in previous paragraph.

The conclusion drawn is that uranium strongly alloys with nickel and "sinks into" the nickel substrate. This would explain the uniformity of uranium coverage and the absence of surface structures that protrude away from the surface. Only later on, when many more atoms arrive to the surface, they start forming islands (or dendrites) of pure uranium deposits.

No information about the depth of the deposit can be gathered by tilting the SEM stage, since no major structures appear on top of the substrate. Even Castaing's formula for determining the maximum deposit thickness cannot be used, since uranium is not on top of nickel and does not shield its signal. The extent of uranium penetration into nickel could only be elucidated by sectioning the coupon and looking at the profile.

Based on Figure 12.28 which shows the approximate elemental composition of the previous picture measured via EDS, the magnitude of the uranium presence in the deposit can fully be appreciated. Substantial amounts of uranium are present, whereas the SEM-only (Figure 12.26) picture suggested otherwise.

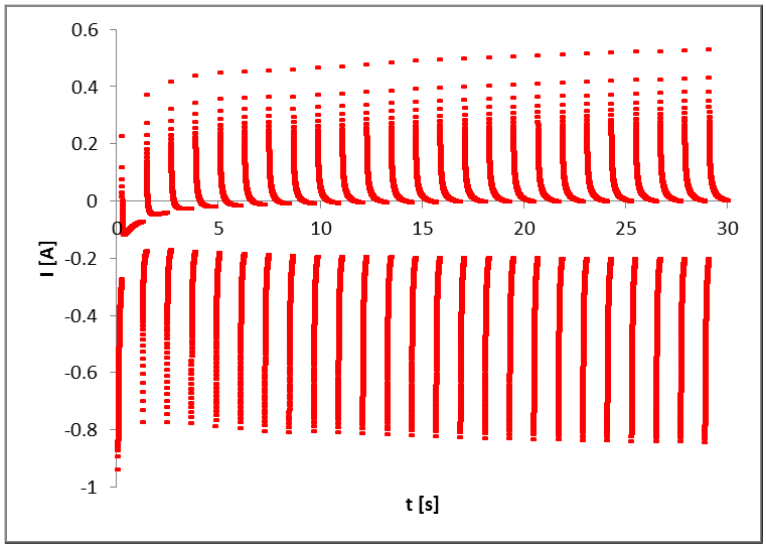

Figure 12.24. Section of the RCA current transient for uranium on nickel. E_{pulse} = -2.33 V, E_{relax} = -2.19 V, $A = 4$ cm^2, $T = 773$ K, $c(UCl_3) = 0.9$ wt%.

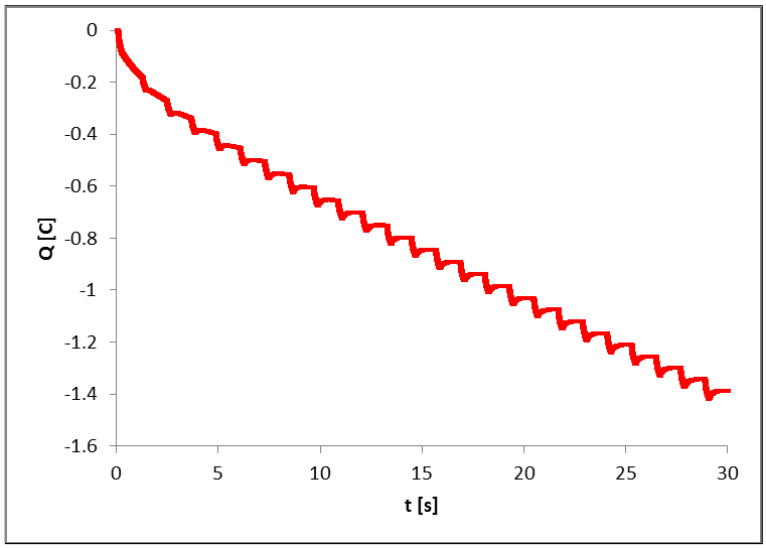

Figure 12.25. Section of the RCA deposition evolution with time for uranium on nickel. E_{pulse} = -2.33 V, E_{relax} = -2.19 V, $A = 4$ cm^2, $T = 773$ K, $c(UCl_3) = 0.9$ wt%.

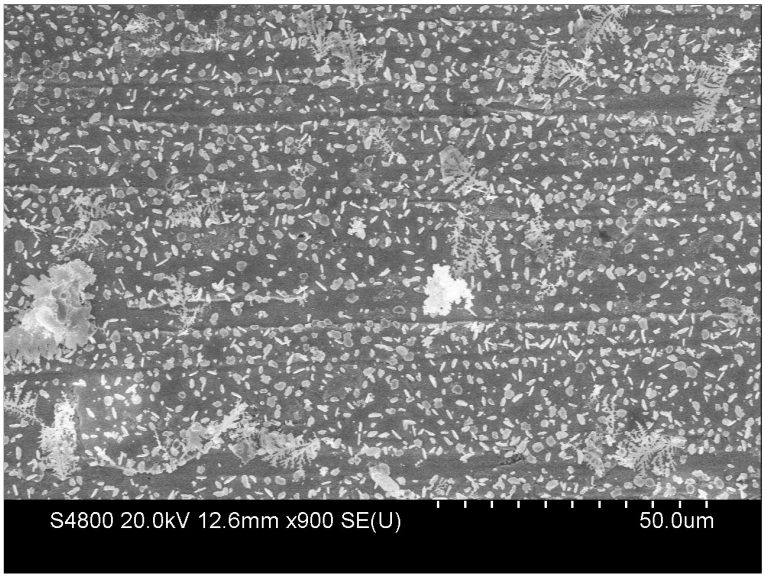

Figure 12.26. SEM picture of uranium deposit on nickel using RCA. E_{pulse} = -2.33 V, E_{relax} = -2.19 V, T = 773 K, $c(UCl_3)$ = 0.9 wt%.

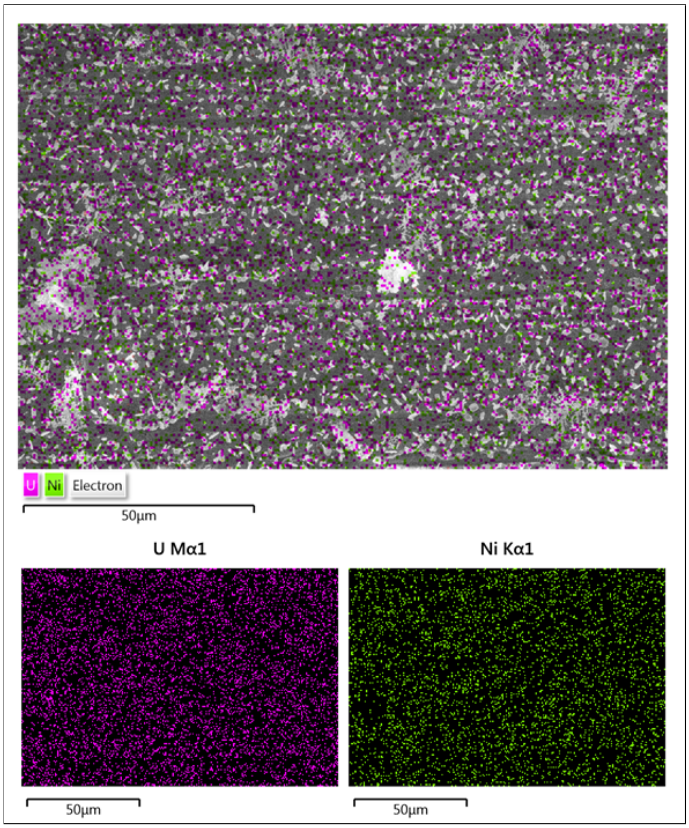

Figure 12.27. EDS map of Figure 12.26. E_{pulse} = -2.33 V, E_{relax} = -2.19 V, T = 773 K, $c(UCl_3)$ = 0.9 wt%.

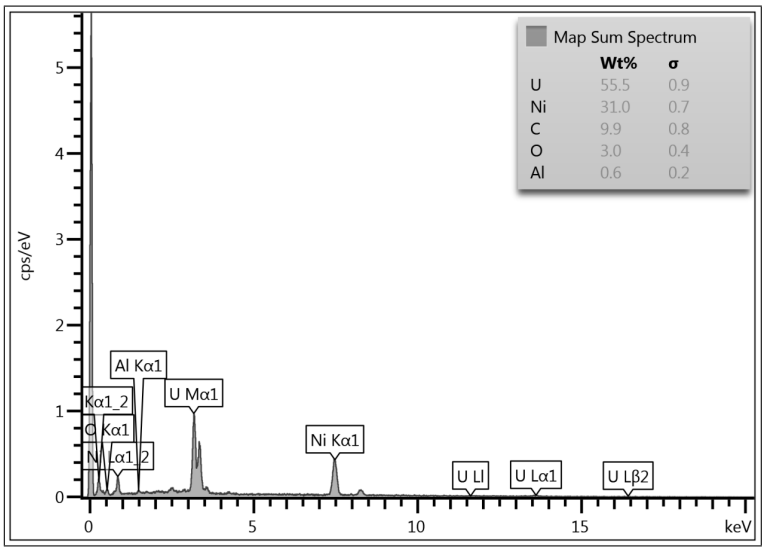

Figure 12.28. EDS map spectrum of Figure 12.27. E_{pulse} = -2.33 V, E_{relax} = -2.19 V, $T = 773$ K, $c(UCl_3) = 0.9$ wt%.

The EDS probe also reveals large amounts of carbon present. This is believed to be an artifact of sample preparation, where inadvertent contamination of the sample by organic molecules or carbon tape (used to secure the sample in place in the SEM machine) happened. The salt did not contain any carbonates or other components containing carbon. Consequently, carbon is not treated like a codeposited element (unlike zirconium), and no corrections regarding the amount of charge are made.

More figures are presented here featuring uranium and its peculiar interaction with nickel. Figure 12.29 shows the SEM picture which appears to have a bare spot on the left with otherwise good deposit coverage.

However, when the same figure is overlaid with the elemental map from the EDS, it displays uniform coverage for the whole surface (for both uranium and nickel), no bare spot can be distinguished—see Figure 12.30. The only regions where the uranium signal is missing are the valleys of the scratch marks caused by the polishing tool. Uranium is missing from those valleys, since these sites are energetically less favorable for nucleation compared to the rest of the surface.

The EDS map spectrum for the given picture is displayed in Figure 12.31. Again large amounts or uranium are present, confirming good coverage.

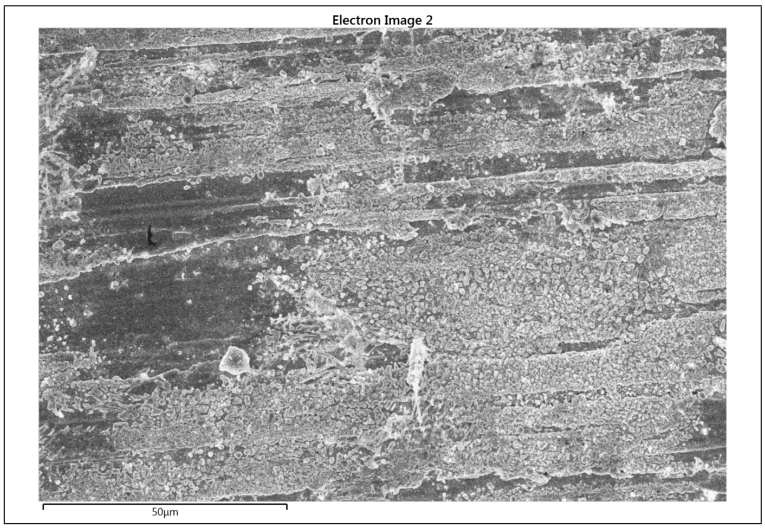

Figure 12.29. SEM picture of uranium deposit on nickel using RCA. E_{pulse} = -2.33 V, E_{relax} = -2.17 V, T = 773 K, $c(UCl_3)$ = 1.6 wt%.

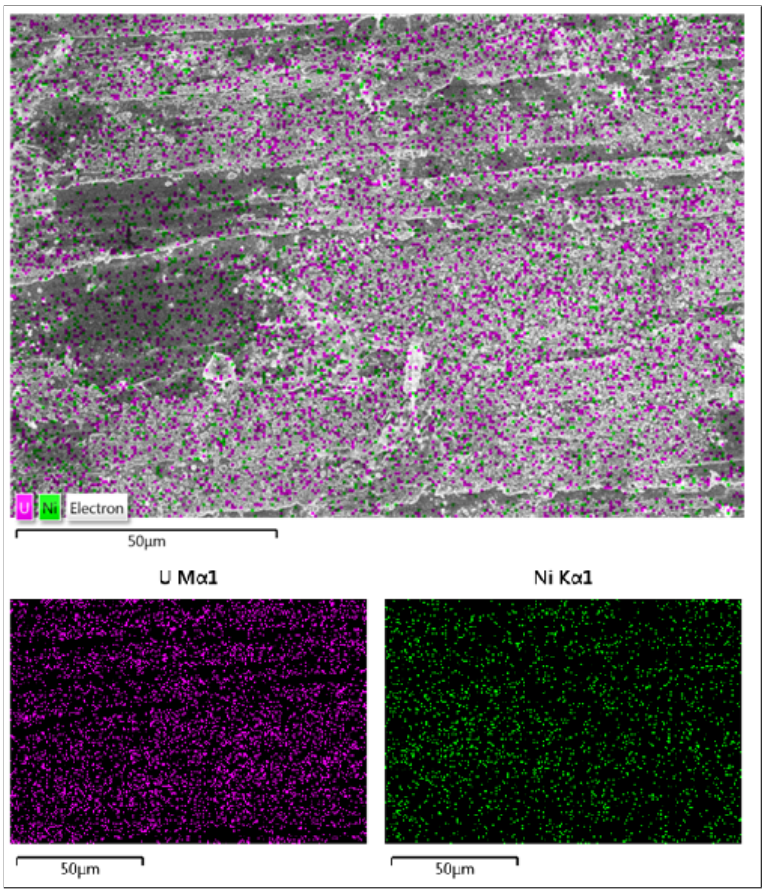

Figure 12.30. EDS map of Figure 12.29. E_{pulse} = -2.33 V, E_{relax} = -2.17 V, T = 773 K, $c(UCl_3)$ = 1.6 wt%.

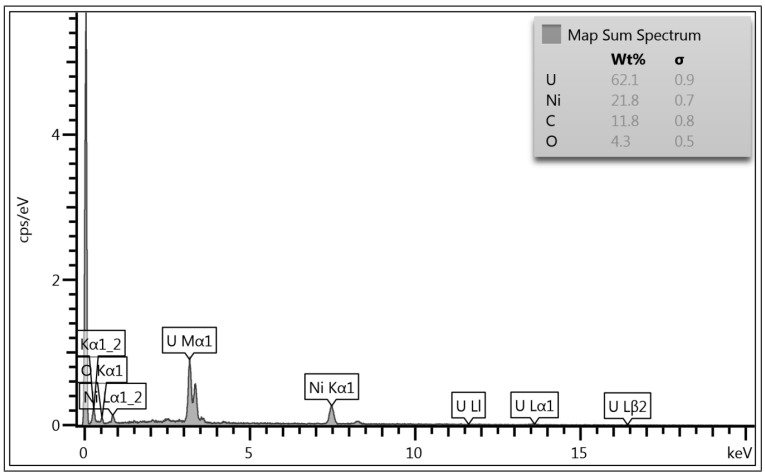

Figure 12.31. EDS map spectrum of Figure 12.30. E_{pulse} = -2.33 V, E_{relax} = -2.17 V, T = 773 K, $c(UCl_3)$ = 1.6 wt%.

Another SEM picture featuring uranium deposition is displayed in Figure 12.32. Lesser magnification is used here. Scratch marks caused by the polishing tool are clearly visible, with occasional globular formations on top.

Uniform uranium and nickel coverage are again observed under the EDS map overlay in Figure 12.33. Uranium follows the pattern of the scratch marks and is absent from valleys. EDS spectrum of the given picture is displayed in Figure 12.34, again featuring large amounts of uranium.

12.3.2.3 Stripping

Since the reactive nature of nickel was revealed to be much more pronounced in the case of uranium compared to thorium, the stripping was anticipated to be comparatively more difficult. To reiterate the objectives of stripping: (a) the surface should not be appreciably altered during stripping, while (b) all deposit must be stripped off to eliminate background for subsequent alpha spectroscopy measurements.

A set of three samples was designed to investigate the stripping of uranium. The first sample (33-0) was a benchmark—new, polished nickel coupon. Two other coupons were immersed in the salt and one standard RCA deposition cycle followed by stripping (using CA) was applied. One coupon was set aside and was designated as the second sample (33-1). The other coupon was immersed back and underwent another standard deposition/stripping cycle. This was the third sample (33-2).

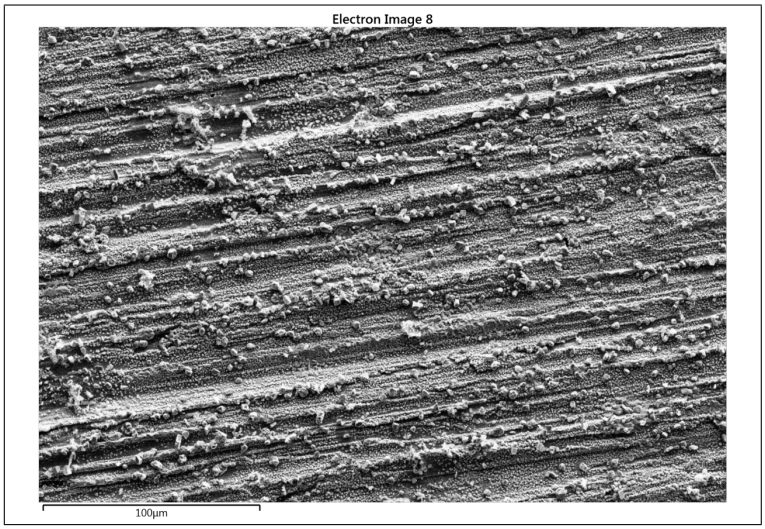

Figure 12.32. SEM picture of uranium deposit on nickel using RCA. E_{pulse} = -2.33 V, E_{relax} = -2.15 V, T = 773 K, $c(UCl_3)$ = 2.8 wt%.

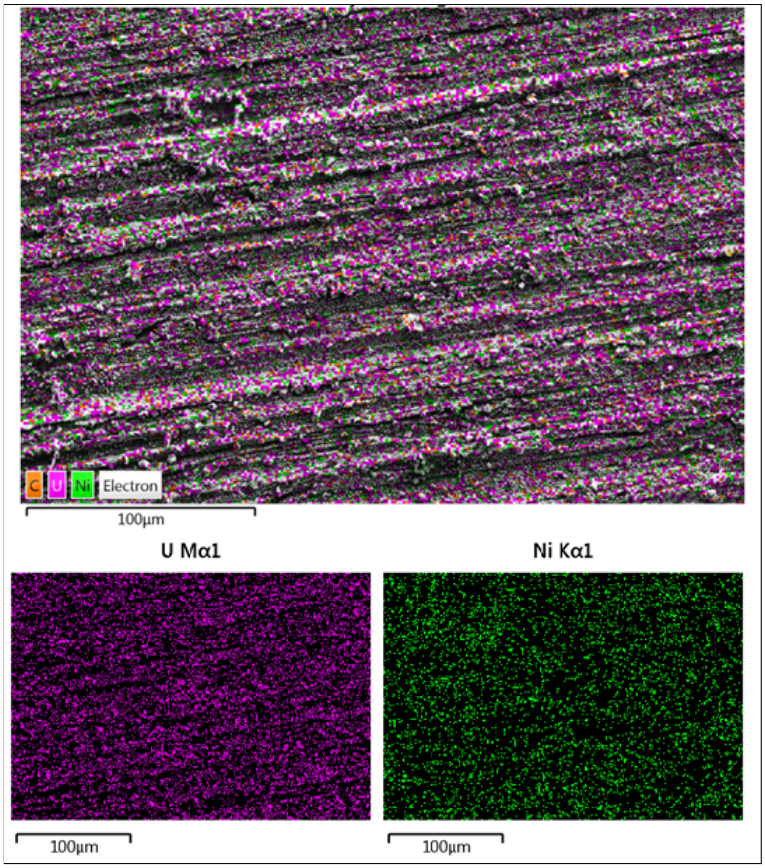

Figure 12.33. EDS map of Figure 12.32. E_{pulse} = -2.33 V, E_{relax} = -2.15 V, T = 773 K, $c(UCl_3)$ = 2.8 wt%.

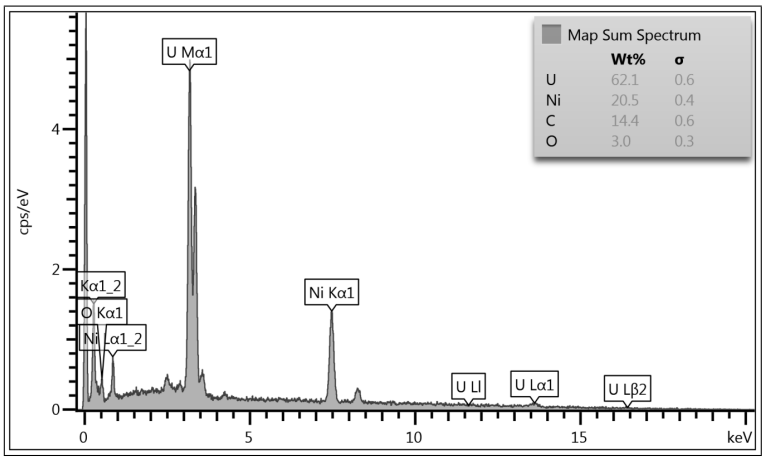

Figure 12.34. EDS map spectrum of Figure 12.33. E_{pulse} = -2.33 V, E_{relax} = -2.15 V, T = 773 K, $c(UCl_3)$ = 2.8 wt%.

Stripping was done under CA conditions, holding potential at -1.20 V, until equivalent amount of charge was passed to equal out the previously deposited amount.

SEM-EDS map overlay with attached elemental composition is the most illustrative way for interpreting the stripping experiment. Three composite pictures corresponding to the three samples are presented here: Figures 12.35, 12.36, 12.37.

Figure 12.35 is this benchmark nickel coupon. Polishing tool scratch marks are visible, and the composition is pure nickel.

Figure 12.36 is the sample 33-1 after one deposition/stripping cycle—the surface is not appreciably altered, however uranium concentration is reaching about 7 wt%. It is important to realize that 7 wt% translates to about 0.5 at% since uranium atom is relatively heavy compared to nickel.

Figure 12.37 is the sample 33-2 after two cycles. Here the stripping cycle did not reach full amount of coulombs expected, rather the anodic (stripping) current after several hundred seconds reached a plateau of about 2 mA. This was considered the end of useful stripping, since the current was indistinguishable from a background current which has the same magnitude.

Consequently, it was expected that the picture either shows (a) large amounts of uranium still present (if the stripping was incomplete), or (b) trace amounts of uranium like in the previous case (if the stripping was complete).

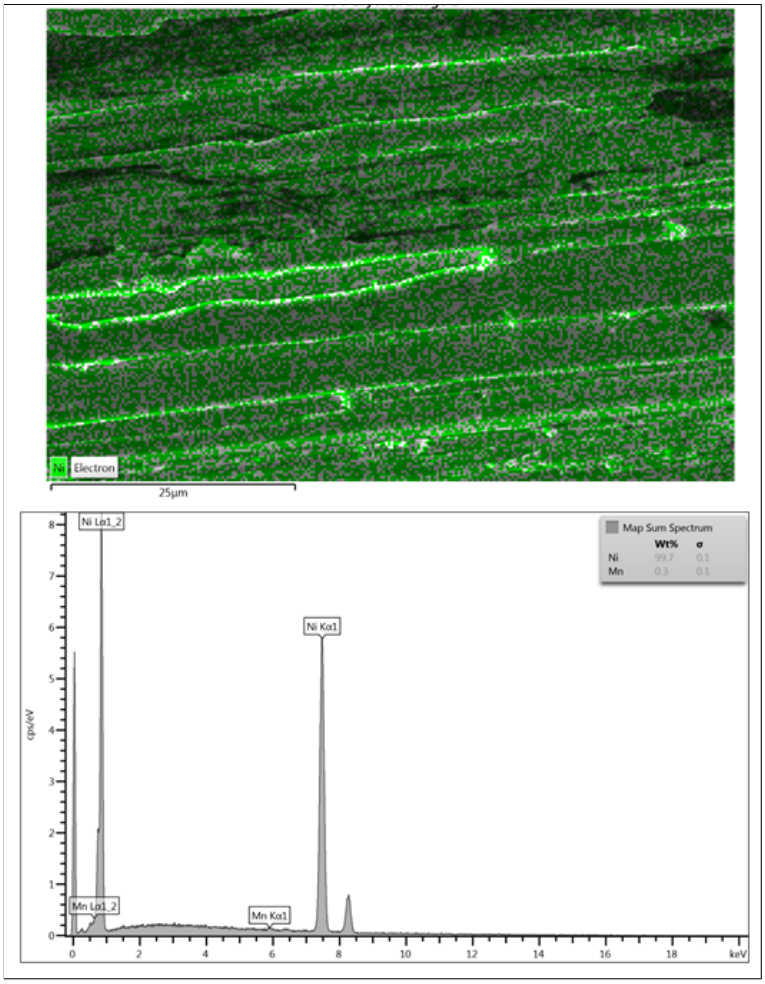

Figure 12.35. EDS map of polished nickel surface serving as a benchmark for stripping experiments.

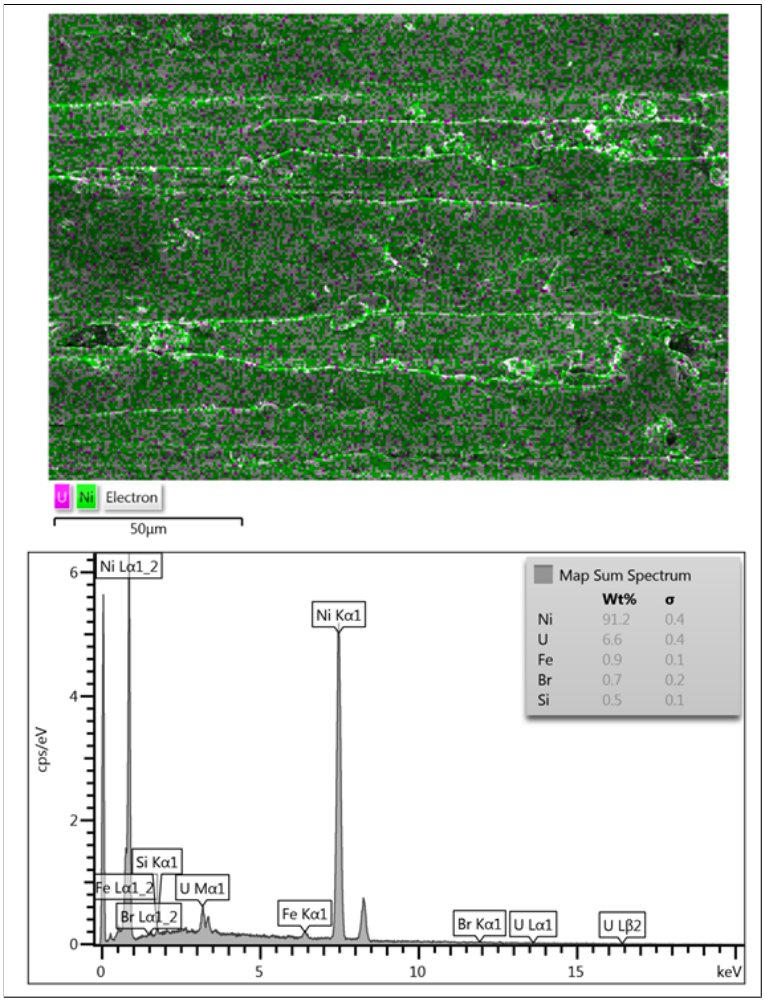

Figure 12.36. EDS map of nickel surface after uranium RCA deposition and subsequent stripping. E_{pulse} = -2.33 V, E_{relax} = -2.19 V, then dissolution using CA at E = -1.20 V. T = 773 K, $c(UCl_3)$ = 3.2 wt%.

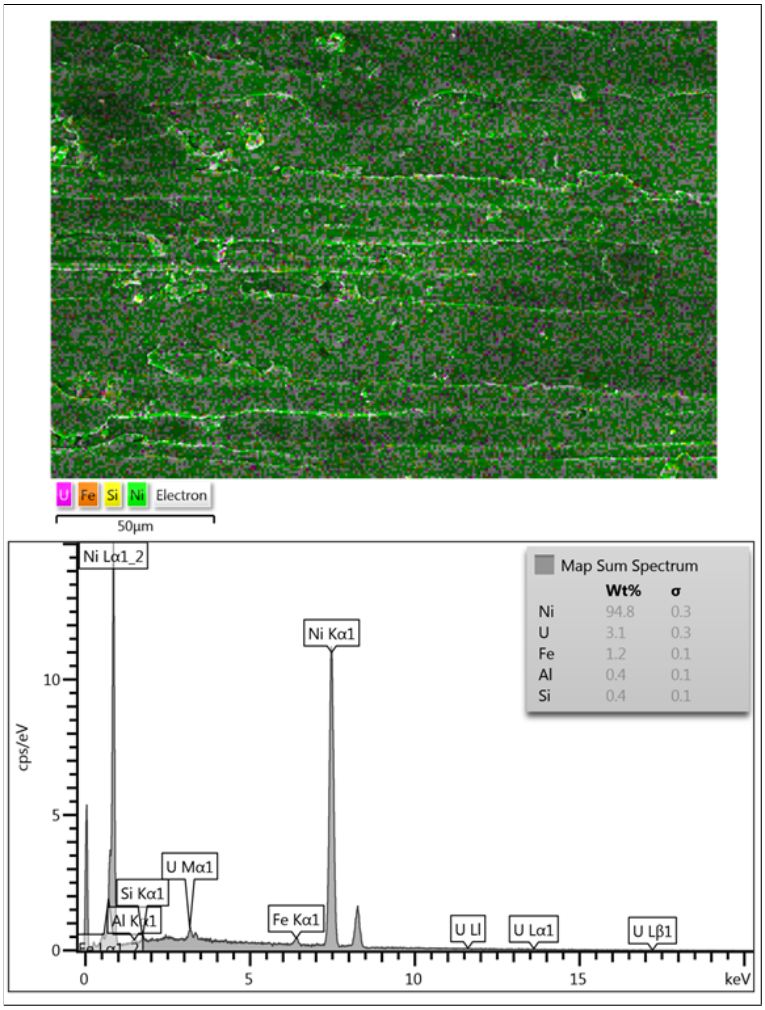

Figure 12.37. EDS map of nickel surface after two uranium RCA depositions and subsequent strippings. E_{pulse} = -2.33 V, E_{relax} = -2.08 V, then dissolution using CA at -1.20 V. $T = 773$ K, $c(UCl_3) = 3.2$ wt%.

The SEM-EDS picture (Figure 12.37) clearly indicates the latter option to be the case. No appreciable surface alterations and very little uranium residue (3 wt% translates into 0.2 at%) is encountered. Probable explanation as to why the stripping ended before the full amount of charge was reached revolves around a possibility of a large piece of uranium deposit (a dendrite?) being liberated from the electrode some time during the run.

Thus, just as in the case of thorium, the stripping of uranium proved to present no particular problem, and the reusability of the detector surface appears feasible.

12.3.2.4 Deposition time correlation

The same transformations of the raw data (Q, t, c) like in the case of thorium are taken (see Section 12.1.4). The charge Q is adjusted for immersion depth, and zirconium codeposition. The deposition time t is normalized for constant value of Q, and averaged over multiple runs when appropriate. The concentration c is determined by ICP-AES.

One difference to the thorium case is encountered, in that the uranium reduction mechanism features three electrons, while the zirconium (and thorium) reduction mechanism features four. Thus, the amount of zirconium content is calculated differently—a ration of 4/3 is inserted into the equation for total uranium charge (compare with Equation 12.6):

$$Q_{tot,U} = Q_{tot} - Q_{tot} \times \frac{4}{3}(\text{Zr [at\%]}) \tag{12.7}$$

A correlation of the deposition time with concentration was constructed. Table 12.7 shows the data points, while Figure 12.38 plots those data points and adds the expected fit, which is of the power type $y = ax^b$.

12.4 Thorium and uranium system

After correlations of deposition time vs. concentration were obtained for thorium and for uranium separately, these two analytes were combined together in a LiCl−KCl eutectic solvent: LiCl−KCl−$ThCl_4$−UCl_3. RCA method was applied to produce codeposits on nickel, and deposition parameters were extracted. Several matrix effects were encountered and are discussed in the following sections.

Table 12.7. Deposition time vs. concentration correlation for uranium on nickel (normalized for 9 C deposition).

Run #	$c(UCl_3)$ [wt%]	Deposition time [s]
24	0.74±0.07	200
26-29	1.49±0.03	114±17
39+40	1.57±0.01	112±23
35+36	3.36±0.01	88±27
30+32	3.90±0.73	80±5
37+38	6.07±0.13	69±34

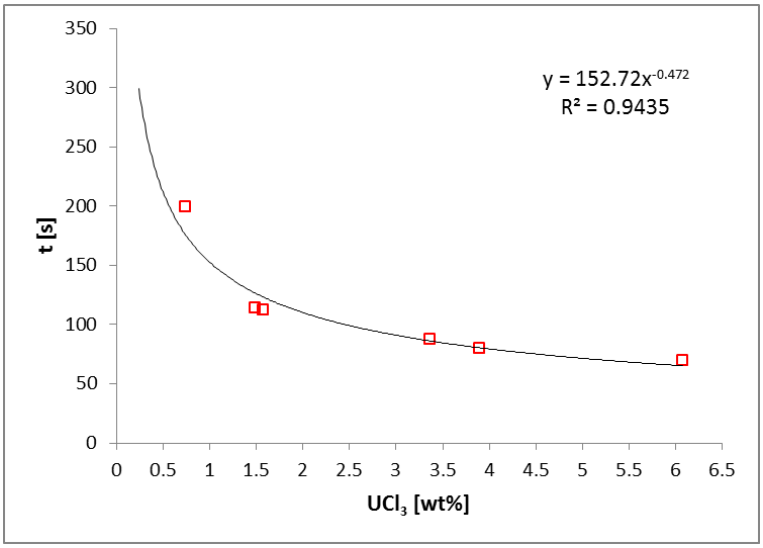

Figure 12.38. Deposition time vs. concentration correlation for uranium on nickel (normalized for 9 C deposition).

12.4.1 Experimental space

A set of experiments with varying concentrations was devised to investigate the effects of codeposition on deposition time. The experimental space (i.e., ranges of concentrations considered) was introduced previously in Figure 11.8 (Section 11.9), with intended collection of data points indicated.

Due to the unpredictability of the additions, where the amount of added analyte was diminished by a variable fraction due to moisture reaction (see Sections 6.1 and 12.1.1 for details), the actual collected data points deviated from the plan.

The actual collected data points are shown in Figure 12.39. The "low thorium" portion (A in Figure 11.8) was mostly followed as well as "low uranium" (C), and "high uranium" (B) portions. The "high thorium" (D) portion, and the intermediate thorium/uranium (E) portions proved to be exceptionally difficult to achieve. Table 12.8 displays individual concentrations (acquired by ICP-AES) of these data points.

The difficulty prompted the laboratory to synthesize the required chemicals (UCl_3, $ThCl_4$) in-house (see Section 11.10 for more details).

Several runs where variable concentrations of one analyte were met by relatively low concentrations of the second analyte were performed. To define "low" and "high" more precisely, a low concentration is considered to be below 1 wt% actinide chloride. High concentration is considered to be above 2 wt% in the case of thorium chloride, and above 4 wt% in the case of uranium chloride (uranium concentration is overall higher in the actual electrorefiner).

The hypothesis of the analytical method expects that the higher the combined concentration of the two analytes, the shorter the deposition time.

12.4.2 Repeating chronoamperometry

Since thorium was present in these runs, the pulse potential was pushed back to its original thorium value (E_{pulse} = -2.40 V) to ensure diffusion limited deposition of thorium. The parameters of the RCA are given in Table 12.9.

12.4.2.1 Nickel coupons

The first 30 s of a current transient for Run #76 (ID 5U-5T, see Table 12.8) is shown in Figure 12.40, with accompanying evolution of charge in time in Figure 12.41.

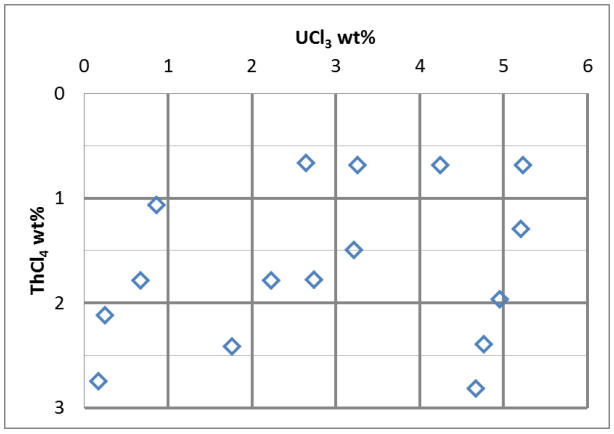

Figure 12.39. Experimental space with actual collected data points.

Table 12.8. Actual concentrations (acquired by ICP-AES) of various experimental data points from Figure 12.39.

Run #	ID	$c(ThCl_4)$ [wt%]	$c(UCl_3)$ [wt%]	Dep. time [s]
42	2U-1T	0.67±0.01	2.65±0.04	97
62+63	3U-1T	0.69±0.01	3.26±0.03	136±43
64+65	4U-1T	0.69±0.01	4.25±0.02	104±4
66+67	5U-1T	0.69±0.01	5.23±0.04	88±11
68+69	5U-2T	1.30±0.01	5.21±0.04	79±1
70-72	5U-3T	1.97±0.03	4.96±0.07	80±6
73+74	5U-4T	2.40±0.01	4.77±0.01	78±8
75+76	5U-5T	2.82±0.01	4.67±0.05	63±9
81-83	1U-1T	1.07±0.09	0.86±0.07	149±20
84-86	1U-2T	1.79±0.07	0.67±0.03	183±22
87+88	1U-3T	2.12±0.11	0.25±0.02	122±12
89+90	1U-4T	2.75±0.04	0.17±0.03	93±3
91+92	2U-4T	2.42±0.04	1.76±0.01	93±2
93+94	3U-4T	1.79±0.01	2.23±0.02	118±5
95+96	3U-3T	1.50±0.02	3.22±0.02	274±137
97+98	3U-2T	1.78±0.01	2.74±0.01	208±62

Table 12.9. Typical parameters of RCA runs for codeposition of thorium and uranium on nickel.

Parameter	Nickel
	Runs 42-76
E_{pulse} [V]	-2.40
E_{relax} [V]	-2.05 to -2.18
t_{pulse} [s]	0.2
t_{relax} [s]	1.0

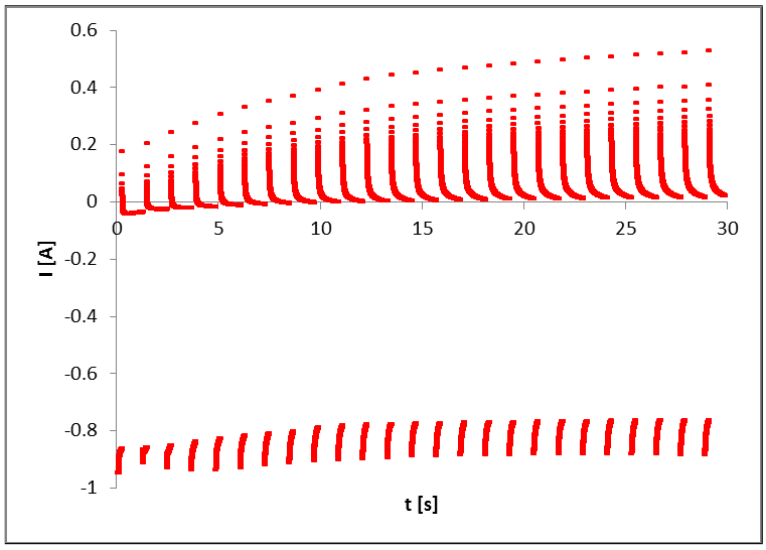

Figure 12.40. Section of the RCA current transient for thorium and uranium on nickel. E_{pulse} = -2.40 V, E_{relax} = -2.13 V, $A = 4$ cm^2, $T = 773$ K, $c(ThCl_4) = 2.8$ wt%, $c(UCl_3) = 4.7$ wt%.

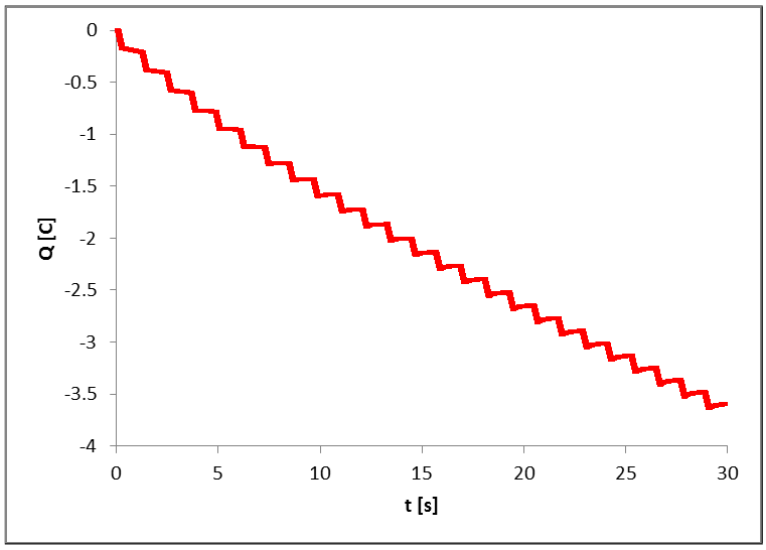

Figure 12.41. Section of the RCA deposition evolution with time for thorium and uranium on nickel. E_{pulse} = -2.40 V, E_{relax} = -2.13 V, $A = 4$ cm^2, $T = 773$ K, $c(ThCl_4) = 2.8$ wt%, $c(UCl_3) = 4.7$ wt%.

Figure 12.42 displays the SEM picture from the same run. No prominent surface features, nor sharp contrast between dark and bright regions is given. Without reference, one cannot tell whether the picture is dark (lower Z = nickel) or bright (higher Z = thorium/uranium); this leaves the interpretation to two possibilities: (a) either there is no deposit, or (b) there is uniform deposit everywhere so the dark substrate is obscured.

The EDS map overlay (Figure 12.43) reveals that (b) is the case. Both uranium and thorium coverage is uniform, except for valleys of the scratches caused by the polishing tool. Nickel signal is still visible and uniformly distributed, hinting that the deposit thickness is of uniform and relatively thin thickness. According to Castaing's formula (see Equation 10.18), the deposit is not thicker than approximately:

$$z_{max} = 0.5 \times 0.033[(20^{1.7} - 2.991^{1.7})\frac{232}{11 \times 90} + (20^{1.7} - 3.164^{1.7})\frac{238}{18.7 \times 92}] \quad (12.8)$$

$$z_{max} = 1.0\,[\mu m] \quad (12.9)$$

which suggests that the actinide layer—if it lies on top of nickel—is not thicker than 1.0 µm (a 1:1 uranium:thorium deposit was assumed).

EDS spectrum of the given picture is displayed in Figure 12.44. Both thorium and uranium are present in large quantities. The amount of thorium is larger, despite its smaller concentration in the salt ($c(ThCl_4)$ =2.8 wt% vs. $c(UCl_3)$ =4.7 wt%), and more cathodic redox potential.

SEM-EDS analysis of one more run is presented here. The SEM picture of Run #72 is displayed in Figure 12.45. Lower magnification was used to get a bigger picture of how the deposit covers the coupon surface. A bright deposit is seen on more than 90 % of the area, with one large darker spot indicating bare substrate surface and a couple smaller similar spots.

During uranium-only deposition, a caution in judging SEM pictures was developed, since even straightforward-looking pictures (like this one) could reveal surprising distribution of the deposit once EDS map was overlaid.

The EDS overlay is displayed in Figure 12.46. No abnormal distribution is found—thorium and uranium is present everywhere except the few circular regions, where their signal is completely missing. The nickel signal is much stronger there.

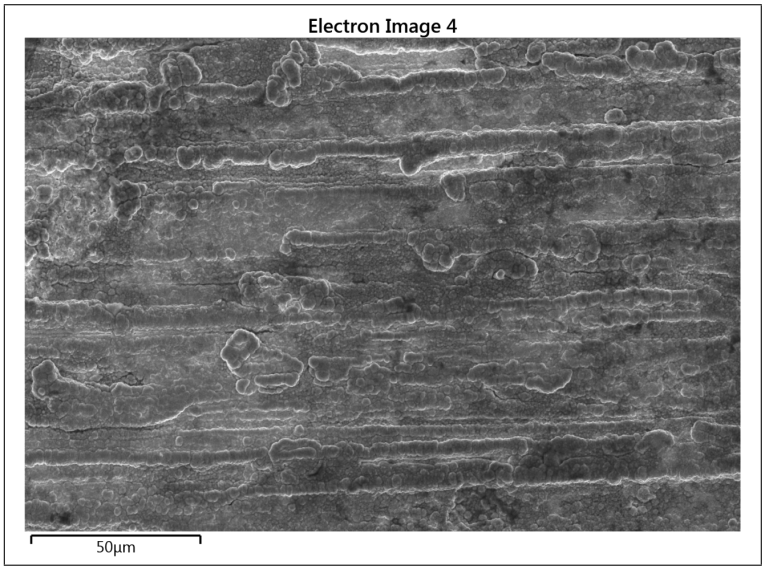

Figure 12.42. SEM picture of thorium and uranium deposit on nickel using RCA. E_{pulse} = -2.40 V, E_{relax} = -2.13 V, T =773 K, $c(ThCl_4) = 2.8$ wt%, $c(UCl_3) = 4.7$ wt%.

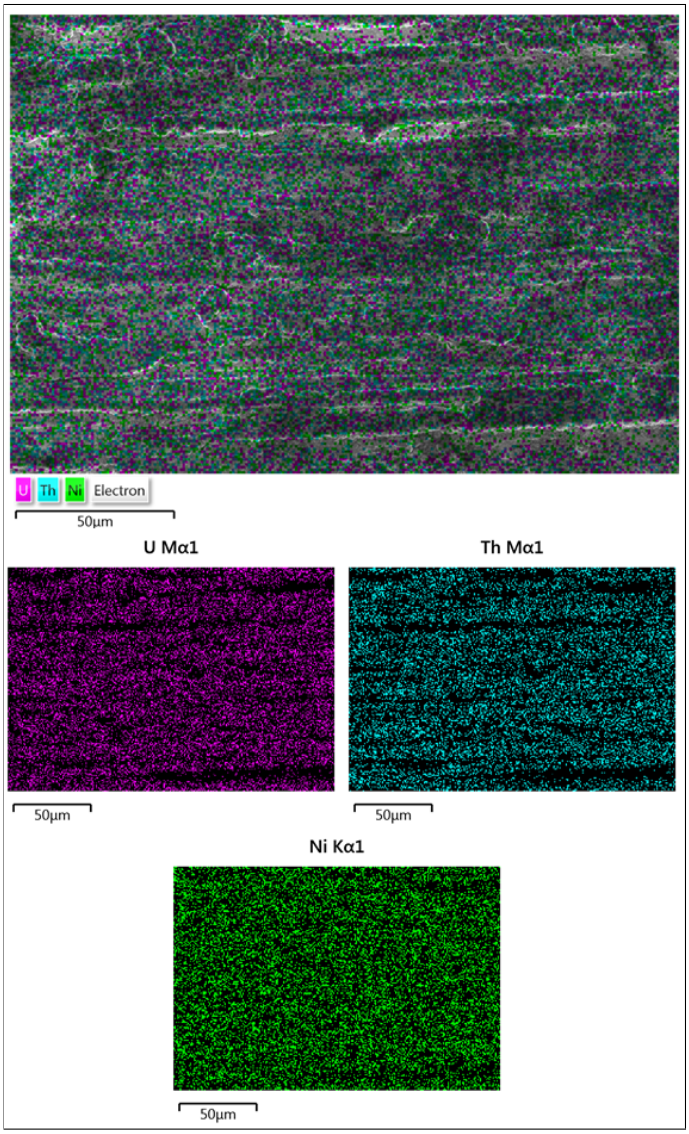

Figure 12.43. EDS map of Figure 12.42. E_{pulse} = -2.40 V, E_{relax} = -2.13 V, T = 773 K, $c(ThCl_4)$ = 2.8 wt%, $c(UCl_3)$ = 4.7 wt%.

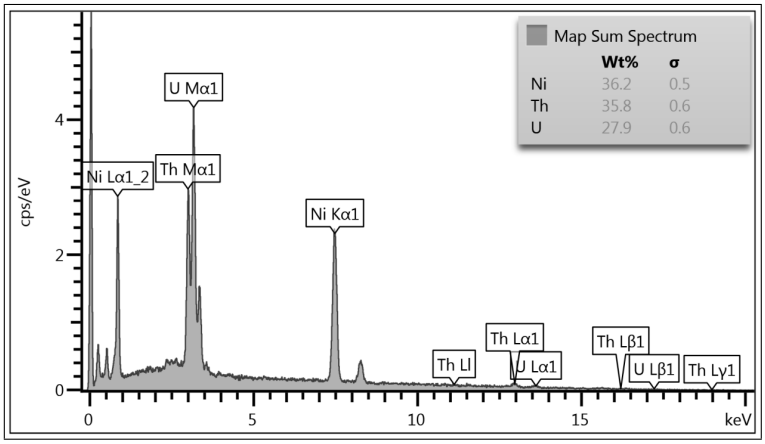

Figure 12.44. EDS map spectrum of Figure 12.43. E_{pulse} = -2.40 V, E_{relax} = -2.13 V, $T = 773$ K, $c(ThCl_4) = 2.8$ wt%, $c(UCl_3) = 4.7$ wt%.

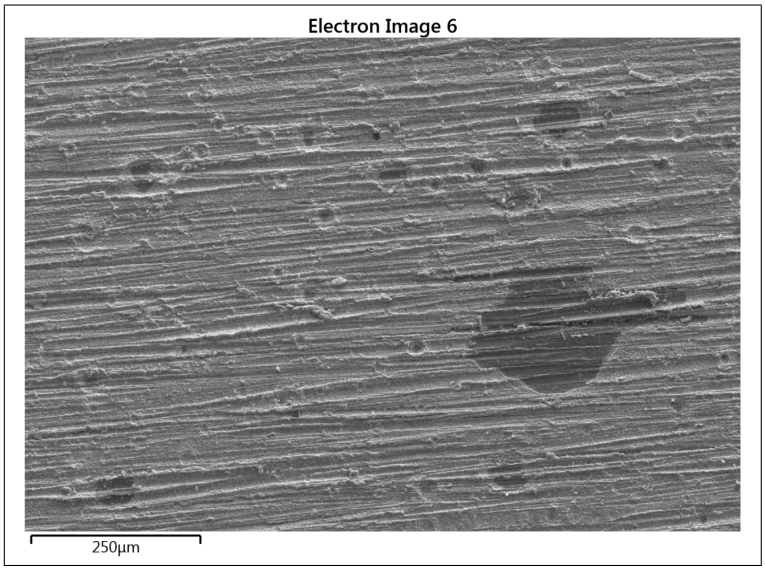

Figure 12.45. SEM picture of thorium and uranium deposit on nickel using RCA. E_{pulse} = -2.40 V, E_{relax} = -2.12 V, $T = 773$ K, $c(ThCl_4) = 2.0$ wt%, $c(UCl_3) = 5.0$ wt%.

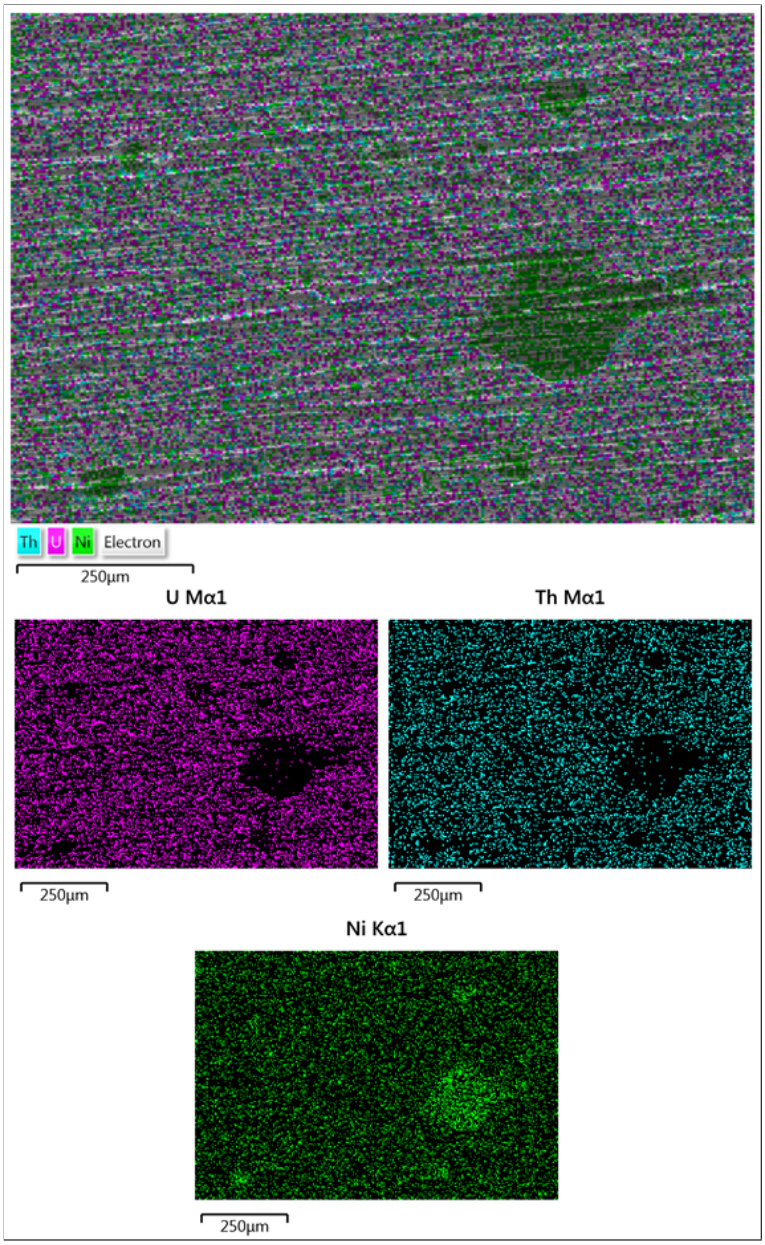

Figure 12.46. EDS map of Figure 12.45. E_{pulse} = -2.40 V, E_{relax} = -2.12 V, T = 773 K, $c(ThCl_4)$ = 2.0 wt%, $c(UCl_3)$ = 5.0 wt%.

The situation is ambiguous, since it was shown previously that uranium can alloy with nickel and distribute itself uniformly, but here it seems to form a layer on top of nickel (like thorium does). Furthermore, it strictly avoids a well defined area of (flat) substrate. Perhaps thorium presence renders uranium tendency to alloy with nickel less energetically favorable.

Since the overall coverage is satisfactory and there are no dendritic formations, the

run is considered successful if large amounts of thorium and uranium are found on the EDS. The EDS spectrum is shown in Figure 12.47. Large amounts of both thorium and uranium are indeed present. Moreover, there is no indication of zirconium codeposition.

These pictures illustrate that overall the codeposition of thorium and uranium on nickel substrate using RCA is successful, and often the deposit is of acceptable quality (little zirconium codeposition, little to no dendritic structures, large amounts of both elements present).

12.4.2.2 Deposition time correlation

Deposition parameters have been obtained by the same transformation of the raw data (Q, t, c) described in previous cases (see Section 12.1.4), with the exception of zirconium content determination.

Since both thorium and uranium were present in the deposits, zirconium content had to be subtracted from the total charge using modified equation:

$$Q_{tot,U+Th} = Q_{tot} - Q_{tot}\frac{4(\text{Zr [at\%]})}{4(\text{Zr [at\%]}) + 4(\text{Th [at\%]}) + 3(\text{U [at\%]})} \tag{12.10}$$

A plot showing both previously obtained correlations of deposition time with concentration of thorium or uranium alone is displayed in Figure 12.48.

Strictly speaking, the uranium deposition is somewhat faster, since its reduction requires one less electron than thorium reduction (3 vs. 4). Thus the number of reduced atoms in a fixed amount of charge passed (9 C) is greater. However, the method aims at achieving fixed deposit thickness (facilitated by fixed amount of charge passed) rather than reducing fixed amount of atoms. In this regard the deposition rate of thorium appears to be: (a) slower than the deposition rate of uranium below about 1.5 wt% actinide chloride, and (b) faster above about 1.5 wt% (see Figure 12.48).

When Figure 12.48 was populated with newly collected data points from the combined salt (their composition is displayed in Figure 12.39 or Table 12.8) a large discrepancy was observed—see Figure 12.49. The deposition time for these combined salt experiments appeared to be slower in all cases vs. the single-analyte salts correlations developed earlier.

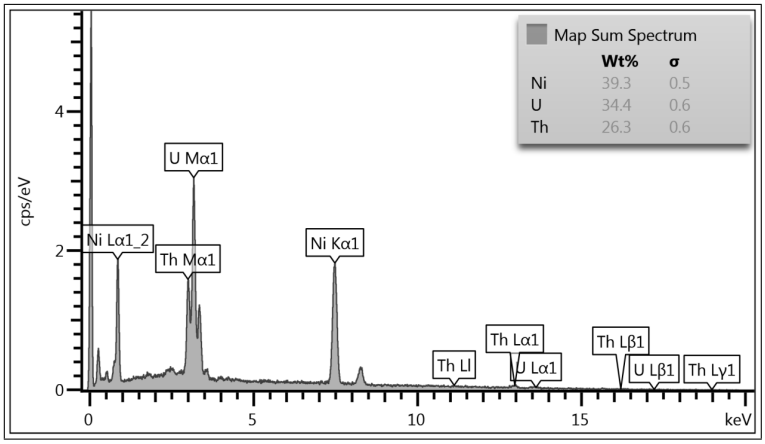

Figure 12.47. EDS map spectrum of Figure 12.46. E_{pulse} = -2.40 V, E_{relax} = -2.12 V, T = 773 K, $c(ThCl_4)$ = 2.0 wt%, $c(UCl_3)$ = 5.0 wt%.

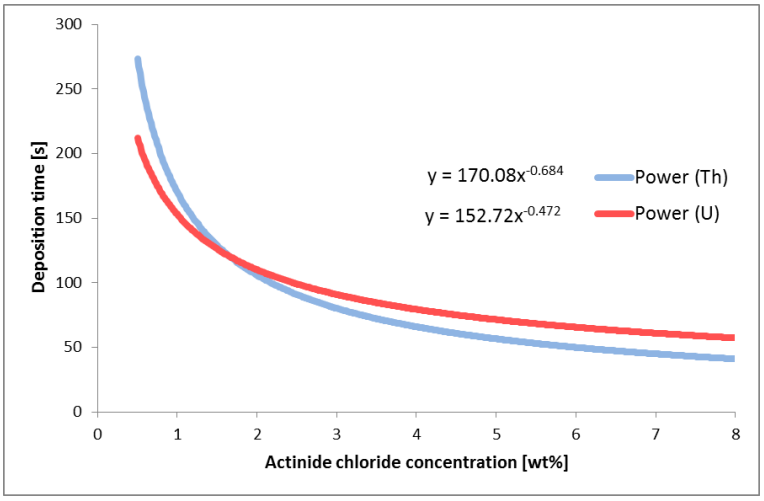

Figure 12.48. Deposition time vs. concentration for two separate analytes.

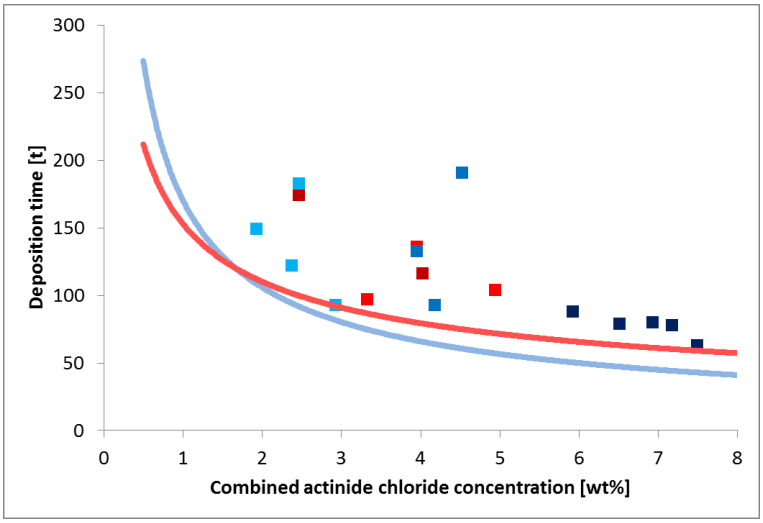

Figure 12.49. Deposition time vs. concentration for various two-analyte salt compositions (with single analyte results overlaid as two curves).

This unexpected result prompted an investigation into possible interactions between the two analytes that might play a role in the combined salt. These matrix effects are discussed below.

12.4.3 Matrix effects on deposition time

12.4.3.1 Method description

The method expected that the introduction of some amount of a second analyte into the salt would result in faster deposition as the two partial diffusional currents add up (see Section 10.12.2).

Since the experimental results showed a complete opposite—the combined salt deposition time was always longer than single-salt depositions for equivalent actinide concentration (see Figure 12.49)—the effect of one analyte concentration on the deposition time of the other analyte was investigated.

12.4.3.2 Low uranium content in thorium matrix

The case of low uranium content in a thorium matrix is treated first. The relevant runs are: IDs 1U-1T, 1U-2T, 1U-3T, 1U-4T. Uranium content ranged from 0.17 to 0.86 wt%, while thorium content was between 1.07 and 2.75 wt% (see Table 12.8).

Two plots of deposition time correlation with concentration are displayed—Figure

12.50 plots thorium content on the x-axis (treating uranium content as marginal), while Figure 12.51 plots the combined concentration (sum of the two analytes) on the x-axis. Both plots have the original thorium-only correlation displayed as well.

As evident from Figure 12.50, there is no decrease in deposition time—vs. thorium-only case—when thorium matrix is met with low uranium additions. The plot suggests that the deposition time is (surprisingly) somewhat increased, although more data point would be needed to reliably confirm this.

The 1U-2T data point (the one with the highest deviation from the thorium-only curve) suffers from excessive zirconium content, which artificially inflates the required deposition time. This data point should therefore be treated with reservation, if not outright discarded.

Figure 12.51 attempts to eliminate the error associated with neglecting the uranium content (which can be significant, especially in the 1U-1T case). All data points lie above the thorium-only case. No clear correlation is established by this correction if the 1U-2T data point remains in place.

12.4.3.3 Low thorium content in uranium matrix

The case of low thorium content in a uranium matrix is presented next. The relevant runs are: IDs 1U-1T, 2U-1T, 3U-1T, 4U-1T, 5U-1T. The thorium content ranged from 0.67 to 1.07 wt%, while the uranium content was between 0.86 and 5.23 wt% (see Table 12.8).

Again, two plots of deposition time correlation with concentration are displayed—Figure 12.52 plots uranium content on the x-axis (treating thorium content as marginal), while Figure 12.53 plots the combined concentration (sum of the two analytes) instead. Both plots have the original uranium-only correlation displayed as well.

Figure 12.52 shows (again) no decrease in deposition time—vs. uranium-only case—when uranium matrix is met with low thorium additions. It is more clearly visible (vs. Figure 12.50) that the deposition time is actually somewhat increased. Again, more data point would be needed to reliably confirm this.

The 2U-1T data point is somewhat problematic from the statistical point of view, since only one run at this concentration was performed.

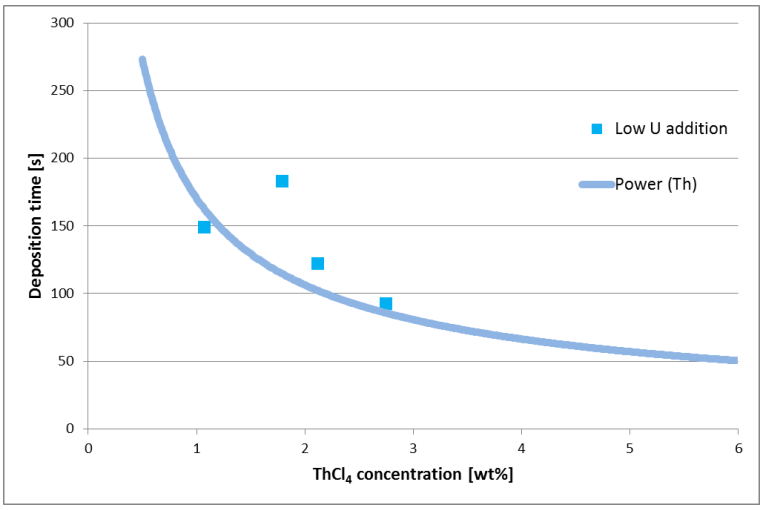

Figure 12.50. Deposition time vs. concentration for low uranium content in thorium matrix case.

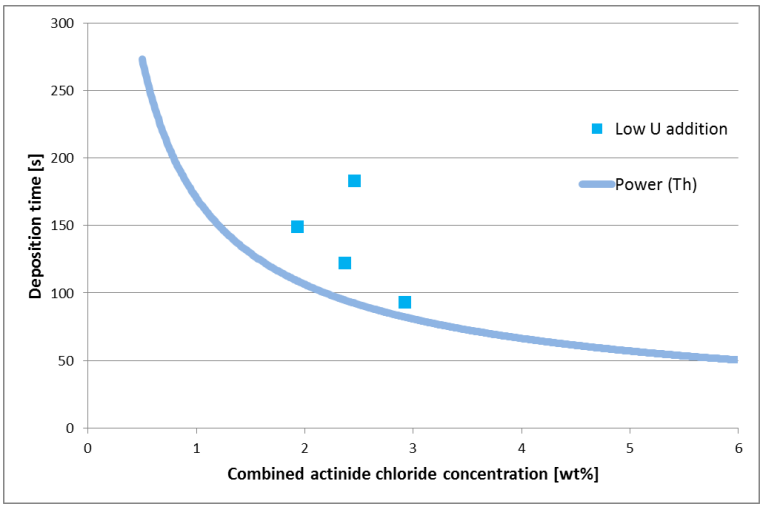

Figure 12.51. Deposition time vs. concentration for low uranium in thorium matrix case, with uranium and thorium concentrations combined.

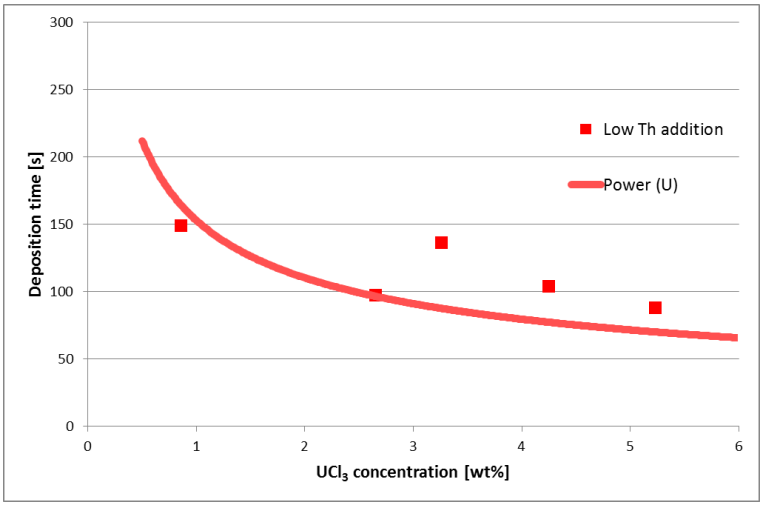

Figure 12.52. Deposition time vs. concentration for low thorium content in uranium matrix case.

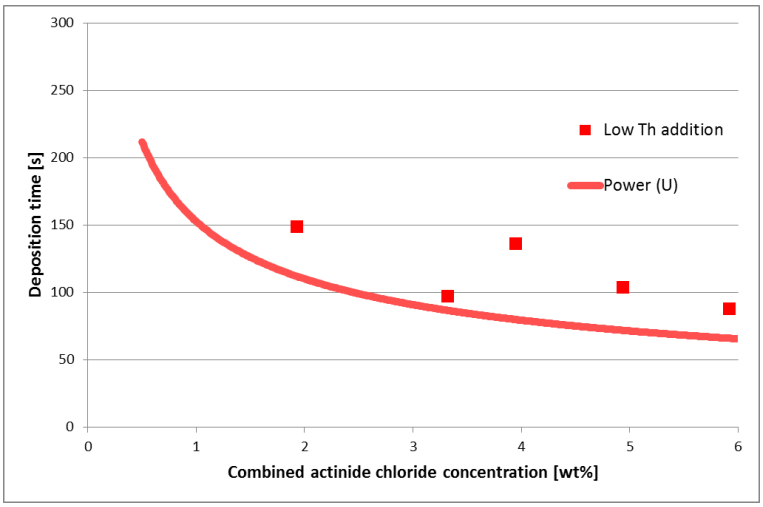

Figure 12.53. Deposition time vs. concentration for low thorium in uranium matrix case, with uranium and thorium concentrations combined.

Figure 12.53 attempts to eliminate the error associated with neglecting the thorium content (which can be significant, especially in the 1U-1T case). A retardation of the deposition is observed vs. the the uranium-only case. The 2U-1T data point should be treated with reservation.

12.4.3.4 High uranium content in thorium matrix

The case of high uranium content in a thorium matrix is treated next. The relevant runs are: IDs 5U-1T, 5U-2T, 5U-3T, 5U-4T, 5U-5T. The uranium content ranged from 4.67 to 5.23 wt%, while the thorium content was between 0.69 and 2.82 wt% (see Table 12.8).

Two plots of deposition time correlation with concentration are displayed—Figure 12.54 plots thorium content on the x-axis, while Figure 12.55 plots the combined concentration (sum of the two analytes) on the x-axis. Both plots have the original thorium-only correlation displayed as well.

Figure 12.54 shows some decrease in deposition time—vs. thorium-only case—when thorium matrix is met with high uranium additions. However, this plot is not very useful as it is the (much higher) uranium concentration that is driving down the deposition time.

In this case, the combined plot (Figure 12.55) is more appropriate. Again a surprising effect of deposition time retardation is seen, as all data points clearly lie above the thorium-only case.

An interesting finding which reveals that the deposition rate of uranium decreases if thorium is added. This conclusion in fact corroborates and expands the one made in "low thorium in uranium matrix" case (Section 12.4.3.3), where retardation of deposition with small additions of thorium was found.

Since this case saw thorium content vary between 0.69 and 2.82 wt% (practically full range of the experimental space), the conclusion is expanded in that the deposition rate of uranium is decreased by *any* thorium addition, whether small or large.

12.4.3.5 High thorium content in uranium matrix

The case of high thorium content in a uranium matrix is presented last. The relevant runs are: IDs 1U-3T, 2U-4T, 5U-5T, 5U-4T. The thorium content ranged

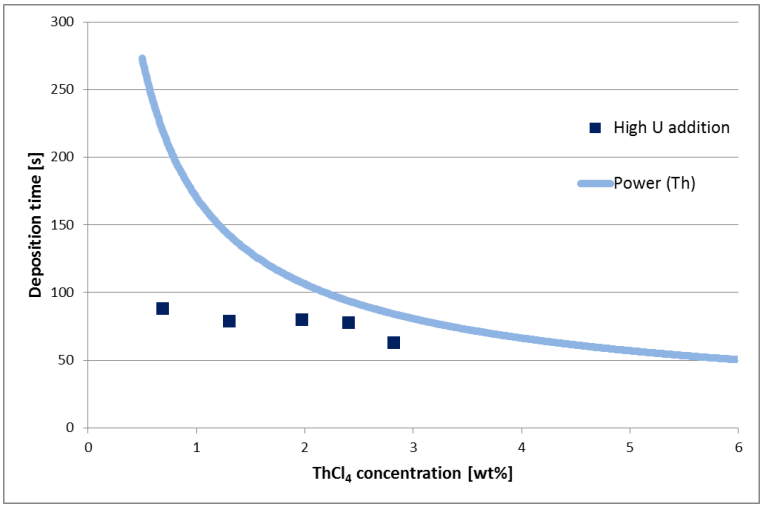

Figure 12.54. Deposition time vs. concentration for high uranium content in thorium matrix case.

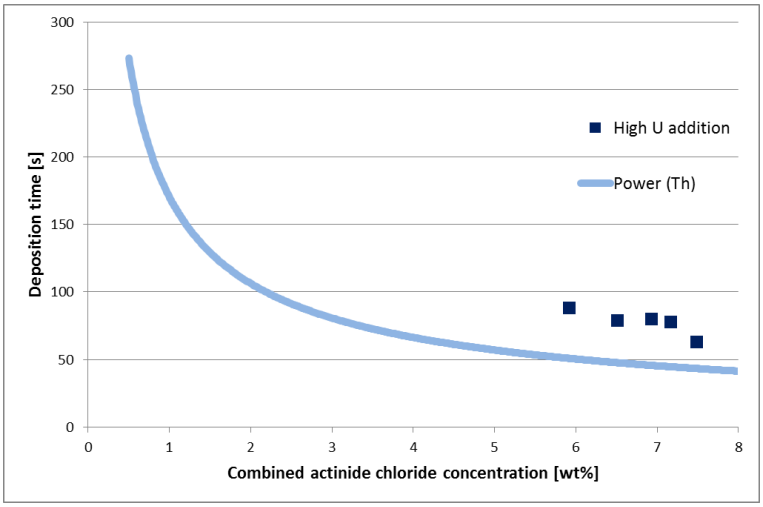

Figure 12.55. Deposition time vs. concentration for high uranium in thorium matrix case, with uranium and thorium concentrations combined.

from 2.12 to 2.82 wt%, while the uranium content was between 0.25 and 4.77 wt% (see Table 12.8).

Two plots of deposition time correlation with concentration are displayed—Figure 12.56 plots uranium content on the x-axis, while Figure 12.57 plots the combined concentration (sum of the two analytes) on the x-axis. Both plots have the original uranium-only correlation displayed as well.

As discussed in the previous case (see Section 12.4.3.4) Figure 12.56 is not very

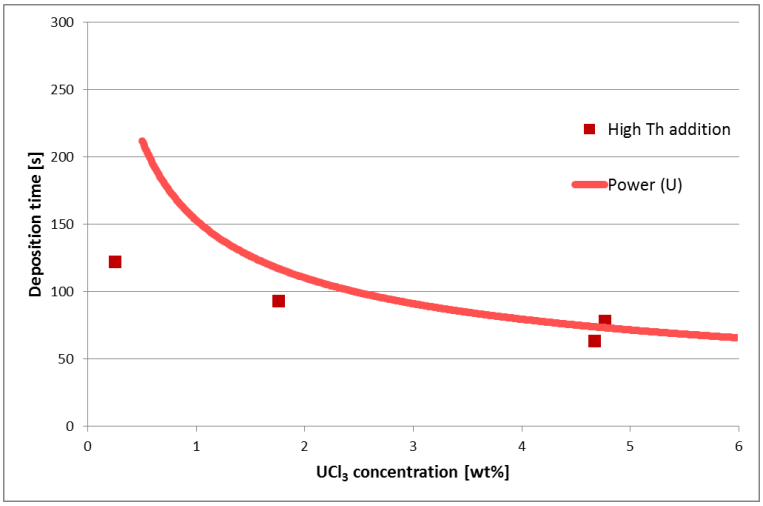

Figure 12.56. Deposition time vs. concentration for high thorium content in uranium matrix case.

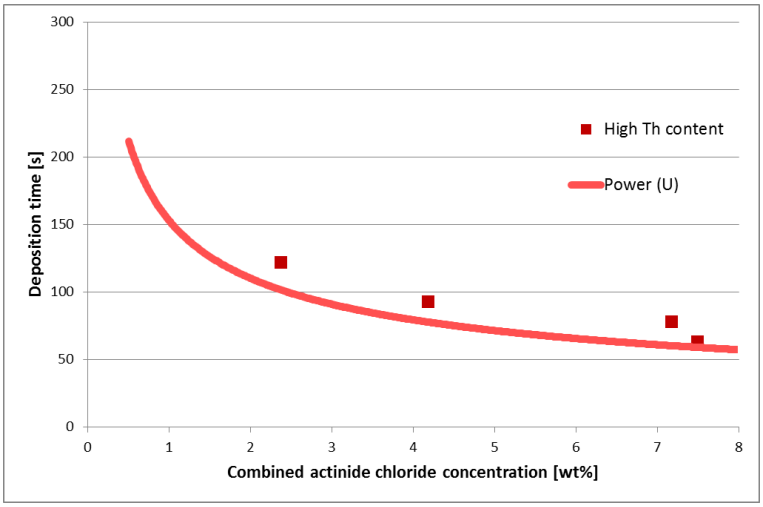

Figure 12.57. Deposition time vs. concentration for high thorium in uranium matrix case, with uranium and thorium concentrations combined.

useful and the combined plot (Figure 12.57) is more appropriate. The effect of deposition time retardation is seen again (although to a lesser degree), as all points lie above the uranium-only case.

This finding corroborates and expands the one made in "low uranium in thorium matrix" case (Section 12.4.3.2), where retardation of deposition with small additions of uranium was found. Since this case saw uranium content vary between 0.25 and 4.77 wt% (practically full range of the experimental space), the conclusion is expanded

in that the deposition rate of thorium is decreased by *any* uranium addition, whether small or large.

This conclusion is complementary to the one found in previous case: not only is the deposition rate of uranium decreased by any addition of thorium (see Section 12.4.3.4), but now it is seen that also the deposition rate of thorium is decreased by any addition of uranium.

It is emphasized that this complementary finding is not a trivial implication of the former—a possibility existed that uranium deposition rate is decreased by the addition of thorium, while thorium deposition rate is increased (or remains unchanged) by some uranium addition; however the experiment showed that this was not the case.

12.4.4 Matrix effects on deposit composition

It was shown in Section 12.4.3, that the deposition time correlation with salt composition (regardless of the actual deposit composition) cannot be easily obtained for the mixed system due to unforeseen matrix effects. Attention is now turned to this deposit composition, and investigation of possible matrix effects is conducted.

12.4.4.1 Method description

A factor in determining whether the new method is straightforward to implement is the proportionality of deposit composition with salt composition.

Ideally, it would be easiest if the deposit composition exactly matched the salt one. However this is almost impossible to achieve, since it would require: (a) the redox potentials of both analytes to be exactly the same, (b) their diffusion coefficients to be the same.

If the deposition is performed under the mass transfer limited regime (large applied overpotential), the condition of (a) is relaxed. However, the difference in (b) still prevents the composition of the salt and deposit to be held equal.

Instead, a proportionality is sought, as explained in Section 10.12.2, where the differences in diffusion coefficients (and valences) for thorium and uranium are grouped under constants k_{Th} and k_U, respectively. The partial diffusional current densities of thorium ($i_{Th,d}$) and uranium ($i_{U,d}$), which define the deposition rate, are proportional to their salt concentration (see Equations 10.21 and 10.22).

By combining together Equations 10.24, 10.25, 10.29, the proportionality between the ratio of elements in the salt and their prescribed ratio in the deposit is reached:

$$\frac{Q_{Th}}{Q_U} = \frac{X_{Th}}{X_U}\frac{z_{Th}}{z_U} = \frac{\int_0^t i_{Th,d}(t)dt}{\int_0^t i_{U,d}(t)dt} \tag{12.11}$$

$$\frac{X_{Th}}{X_U}\frac{z_{Th}}{z_U} = \frac{\int_0^t k_{Th}c_{Th}(t)dt}{\int_0^t k_U c_U(t)dt} = \frac{z_{Th}D_{Th}^{1/2}F\pi^{-1/2}\int_0^t t^{-1/2}dt}{z_U D_U^{1/2}F\pi^{-1/2}\int_0^t t^{-1/2}dt}\frac{c_{Th}}{c_U} \tag{12.12}$$

$$\frac{X_{Th}}{X_U} = \frac{D_{Th}^{1/2}}{D_U^{1/2}}\frac{c_{Th}}{c_U} \tag{12.13}$$

In theory the proportionality reduces to the ratio of square roots of respective diffusion coefficients. The elemental ratio X_{Th}/X_U in the deposit (left hand of Equation 12.13) is obtained by SEM-EDS, while the ratio in the salt c_{Th}/c_U is obtained by ICP-AES. The reason for not using ICP-AES for the metal deposit determination is its insufficient sensitivity, since only a few milligrams of actinide metal are deposited.

According to literature, the diffusion coefficient of thorium is $D_{Th} \approx 2.2 \times 10^{-5}$ cm^2 s^{-1} (98, 99); while the diffusion coefficient of uranium is $D_U \approx 1.1 \times 10^{-5}$ cm^2 s^{-1} (92, 110). Thus, the ratio of their square roots is:

$$\frac{D_{Th}^{1/2}}{D_U^{1/2}} = \left(\frac{2.2\times10^{-5}}{1.1\times10^{-5}}\right)^{1/2} = \sqrt{2} \tag{12.14}$$

and so this factor is applied to the salt ratio to arrive at the expected elemental ratio of the deposit (see Equation 12.13).

Table 12.10 summarizes the salt and deposit ratios of the performed runs. It displays the expected deposit ratio as well as the actual one. Also, atomic percentages of salt composition are used here, to be compatible with atomic ratios in the deposit.

The conversion from weight percentage to atomic percentage for salt components is realized as follows:

$$c(ThCl_4)[at\%] = \frac{\frac{c(ThCl_4)[wt\%]}{M(ThCl_4)}}{\frac{c(ThCl_4)[wt\%]}{M(ThCl_4)} + \frac{c(UCl_3)[wt\%]}{M(UCl_3)} + \frac{c(\text{LiCl-KCl})[wt\%]}{M(\text{LiCl-KCl})}} \times 100 \tag{12.15}$$

$$c(UCl_3)[at\%] = \frac{\frac{c(UCl_3)[wt\%]}{M(UCl_3)}}{\frac{c(ThCl_4)[wt\%]}{M(ThCl_4)} + \frac{c(UCl_3)[wt\%]}{M(UCl_3)} + \frac{c(\text{LiCl-KCl})[wt\%]}{M(\text{LiCl-KCl})}} \times 100 \tag{12.16}$$

where M(LiCl-KCl) is the effective molecular weight of the eutectic salt equal to 55.87 g mol^{-1}.

Table 12.10. Salt concentration ratios c_{Th}/c_U (acquired by ICP-AES) and deposit ratios X_{Th}/X_U (acquired by SEM-EDS) of the various runs. Negative difference signifies richer uranium deposit than expected, while positive difference signifies richer thorium deposit than expected.

ID	$c(ThCl_4)$ [at%]	$c(UCl_3)$ [at%]	Salt ratio	Expected deposit ratio	Actual deposit ratio	Diff. (%)
5U-1T	0.11	0.89	0.12	0.17	0.09±0.02	-47%
4U-1T	0.11	0.72	0.15	0.21	0.12±0.04	-43%
3U-1T	0.11	0.55	0.20	0.28	0.20±0.10	-29%
2U-1T	0.10	0.44	0.23	0.33	0.30±0.05	-9%
1U-1T	0.16	0.14	1.14	1.61	1.54±0.21	-4%
3U-3T	0.23	0.54	0.43	0.61	0.62±0.24	+2%
1U-2T	0.27	0.11	2.45	3.64	4.62±1.27	+27%
5U-2T	0.21	0.89	0.24	0.34	0.45±0.08	+32%
5U-3T	0.31	0.85	0.36	0.51	0.78±0.06	+53%
5U-5T	0.45	0.81	0.56	0.79	1.23±0.13	+56%
3U-4T	0.28	0.37	0.76	1.07	1.71±0.32	+60%
2U-4T	0.37	0.30	1.23	1.74	3.20±1.26	+84%
3U-2T	0.28	0.46	0.61	0.86	1.79±0.75	+108%
5U-4T	0.38	0.82	0.46	0.65	1.38±0.09	+112%
1U-3T	0.32	0.04	8.00	11.31	24.69±20.07	+118%
1U-4T	0.42	0.03	14.00	19.80	no U	–

12.4.4.2 Low uranium content in thorium matrix

The case of low uranium content in a thorium matrix is treated first. The relevant runs are: IDs 1U-1T, 1U-2T, 1U-3T, 1U-4T. The uranium content ranged from 0.17 to 0.86 wt%, while the thorium content was between 1.07 and 2.75 wt% (see Tables 12.8 and 12.10).

In extremely small uranium contents (1U-4T, 1U-3T), the uranium codeposition was practically non-existent and the deposit was almost exclusively composed of

thorium. The method is clearly not usable in such extreme.

When small uranium content was encountered (1U-2T), the actual deposit ratio differed from the expected one by slightly elevated thorium content (27 % difference vs. expected ratio, see Table 12.10).

When small uranium content met with comparably small thorium content (1U-1T), the actual deposit ratio was exactly as expected (4 % difference vs. expected ratio, see Table 12.10).

12.4.4.3 Low thorium content in uranium matrix

The case of low thorium content in a uranium matrix is presented next. The relevant runs are: IDs 1U-1T, 2U-1T, 3U-1T, 4U-1T, 5U-1T. Here, the thorium content ranged from 0.67 to 1.07 wt%, while the uranium content was between 0.86 and 5.23 wt% (see Tables 12.8 and 12.10).

When small thorium contents were met by higher uranium contents (all runs except 1U-1T), the actual deposit differed from the expected one by elevated uranium content. The deposit enrichment in uranium was progressively higher (9 to 47 % difference vs. expected ratio) as the thorium content from the expected ratio kept diminishing (0.23 to 0.12)—see Table 12.10.

12.4.4.4 High uranium content in thorium matrix

The case of high uranium content in a thorium matrix is treated next. The relevant runs are: IDs 5U-1T, 5U-2T, 5U-3T, 5U-4T, 5U-5T. Here, the uranium content ranged from 4.67 to 5.23 wt%, while the thorium content was between 0.69 and 2.82 wt% (see Tables 12.8 and 12.10).

An interesting threshold effect was observed. If absolute thorium content in the salt was small (5U-1T), then the expected deposit had elevated contents of uranium (as explained in the previous case). However, once absolute thorium content exceeded 1.3 wt% (0.21 at%)—as in all of the remaining runs—large deviations in favor of rich thorium deposit (vs. expected one) were encountered—see Table 12.10.

The thorium enrichment appears to be progressively higher (32 % to 114 % difference vs. expected ratio) as the thorium content from the expected ratio kept increasing (0.24 to 0.56). Run 5U-4T has even higher thorium content than dictated

by this trend, see Table 12.10.

12.4.4.5 High thorium content in uranium matrix

The case of high thorium content in a uranium matrix is presented last. The relevant runs are: IDs 1U-3T, 2U-4T, 5U-5T, 5U-4T. Here, the thorium content ranged from 2.12 to 2.82 wt%, while the uranium content was between 0.25 and 4.77 wt% (see Tables 12.8 and 12.10).

The threshold effect observed in previous case was confirmed. Almost regardless of the uranium content, when absolute thorium content exceeded 1.3 wt% (all cases), the actual deposit was heavily enriched with thorium (vs. expected one).

The enrichment appears to be progressively higher (54 % to 211 % difference vs. expected ratio) as the thorium content from the expected ratio kept increasing (0.46 to 8.00). Run 5U-4T had again even higher thorium content than dictated by this trend, see Table 12.10.

It is concluded that if threshold amounts of thorium (around 1.3 wt%) are reached, then the actual deposit would deviate from the expected one by being rich in thorium. The extent of this deviation increases as the ratio of thorium in the salt increases.

If thorium stays below the threshold amount, then the ratio of thorium/uranium in the salt dictates the extent of deviation from the expected deposit composition. For uranium-rich salts, the actual deposit is richer in uranium than the expected one. For comparable amounts (ratio around 1), the actual deposit obeys the expected content. Consequently, reliable data can only be collected if the thorium content is below 1.3 wt%.

Finally, if extremely small amounts of uranium (below 0.25 wt%) are encountered, then uranium codeposition is attenuated, and the deposit is almost exclusively composed of thorium. Consequently, the detection limit of the method for these instances is considered to lie around 0.25 wt% UCl_3.

12.4.5 Matrix effects on deposit morphology

One interesting effect of changed morphology by thorium addition to uranium was already mentioned in Section 12.4.2.1. The strong tendency of uranium to alloy with nickel was suppressed by the addition of thorium. Instead, the thorium-uranium

codeposit now formed proper layer on top of the nickel substrate, and genuine bare spots (where no uranium deposit remained) were present.

One example was already given in said section by Figures 12.45 and 12.46 from Run #72. To show that this was no anomaly, more SEM-EDS figures from different runs are presented. Figure 12.58 is from Run #42, Figure 12.59 is from Run #84 and Figure 12.60 is from Run #94.

In all these figures, the reluctance of uranium to alloy with nickel is seen in bare spots. Run #42 is of particular importance, because the thorium content is the lowest, signifying that even a small addition of thorium produces this effect.

Thus, it is concluded that the addition of thorium renders the deposition to proceed without pronounced uranium-nickel alloying effects. One consequence is that Castaing's formula can again be used to estimate the deposit thickness, as was demonstrated in Section 12.4.2.1.

12.5 Discussion

12.5.1 Single salt correlations

During experiments with single salts, it was noted that the variability in deposition times of individual runs is quite large. Consequently, at least two runs (sometimes three) were adopted at each concentration to improve the statistics. Ideally, many more runs would need to be collected at each concentration so that outliers could be properly discarded.

The variability partially stems from the difference in coupon surface features. No two coupons have exactly the same immersion depth, much less the electrochemically active area. In this aspect, the actual detector would behave more predictably, since its surface and its immersion depth would not vary appreciably from run to run.

Even with this limited accuracy, the correlations for thorium and uranium were close to each other, which hints at their similar rate of deposition.

This method appears feasible for use in single analyte salts. However, so do the competing methods, especially voltammetry (which is faster and more practical). The only benefit of this method over voltammetry is its isotopic resolution due to the use of alpha spectroscopy.

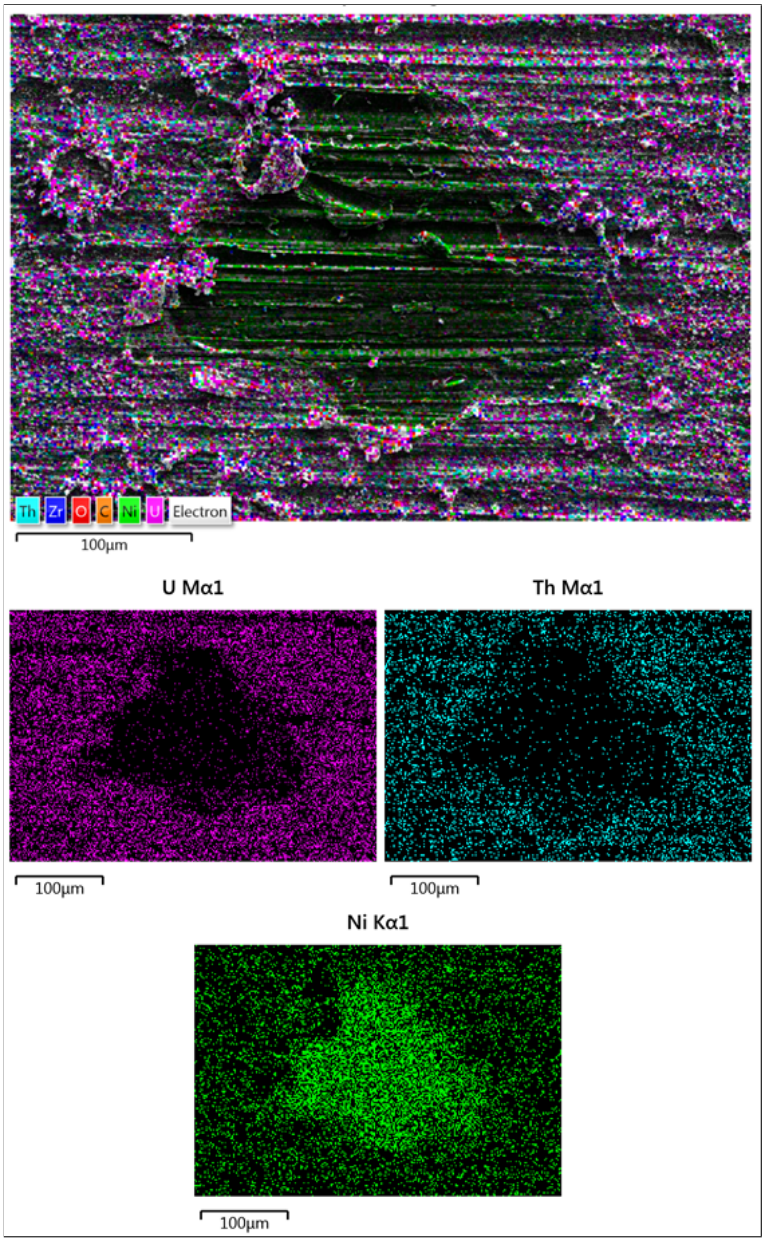

Figure 12.58. SEM-EDS map of Run #42. E_{pulse} = -2.33 V, E_{relax} = -2.14 V, T = 773 K, $c(ThCl_4)$ = 0.67 wt%, $c(UCl_3)$ = 2.65 wt%.

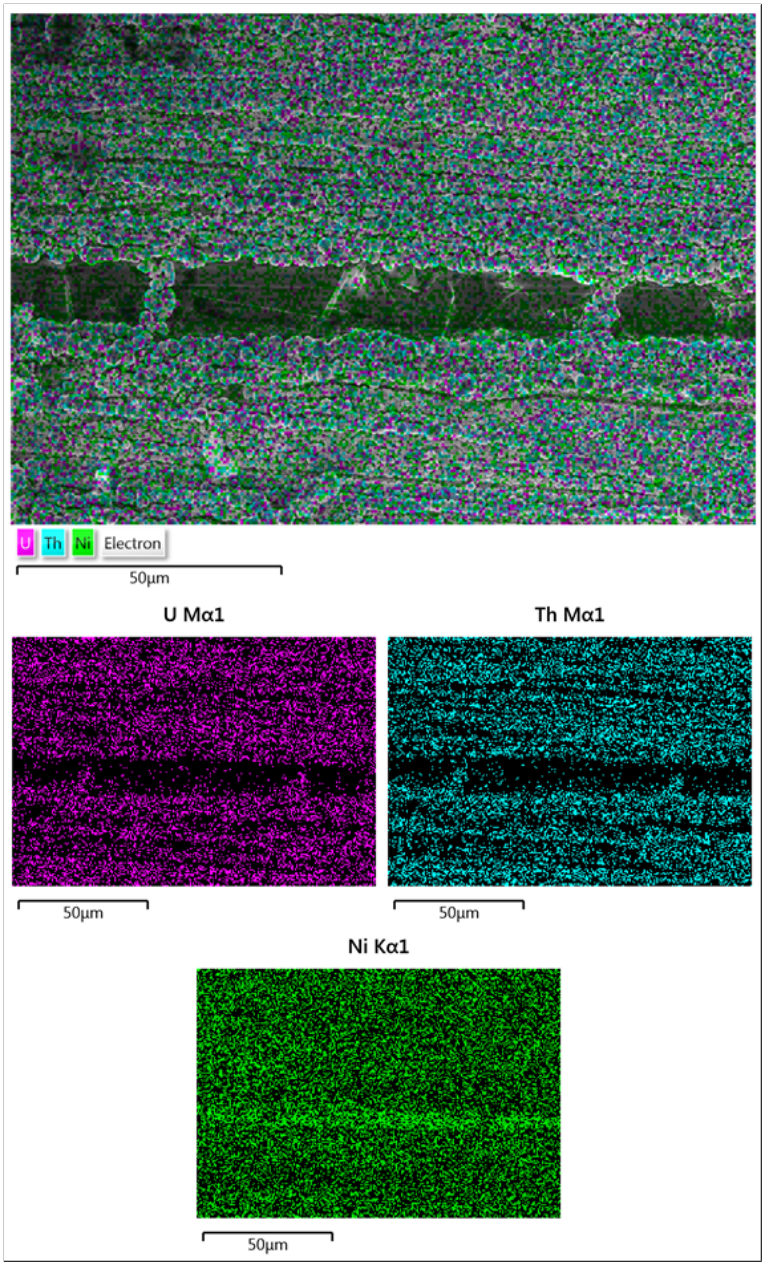

Figure 12.59. SEM-EDS map of Run #84. E_{pulse} = -2.40 V, E_{relax} = -2.12 V, T = 773 K, $c(ThCl_4)$ = 1.8 wt%, $c(UCl_3)$ = 0.7 wt%.

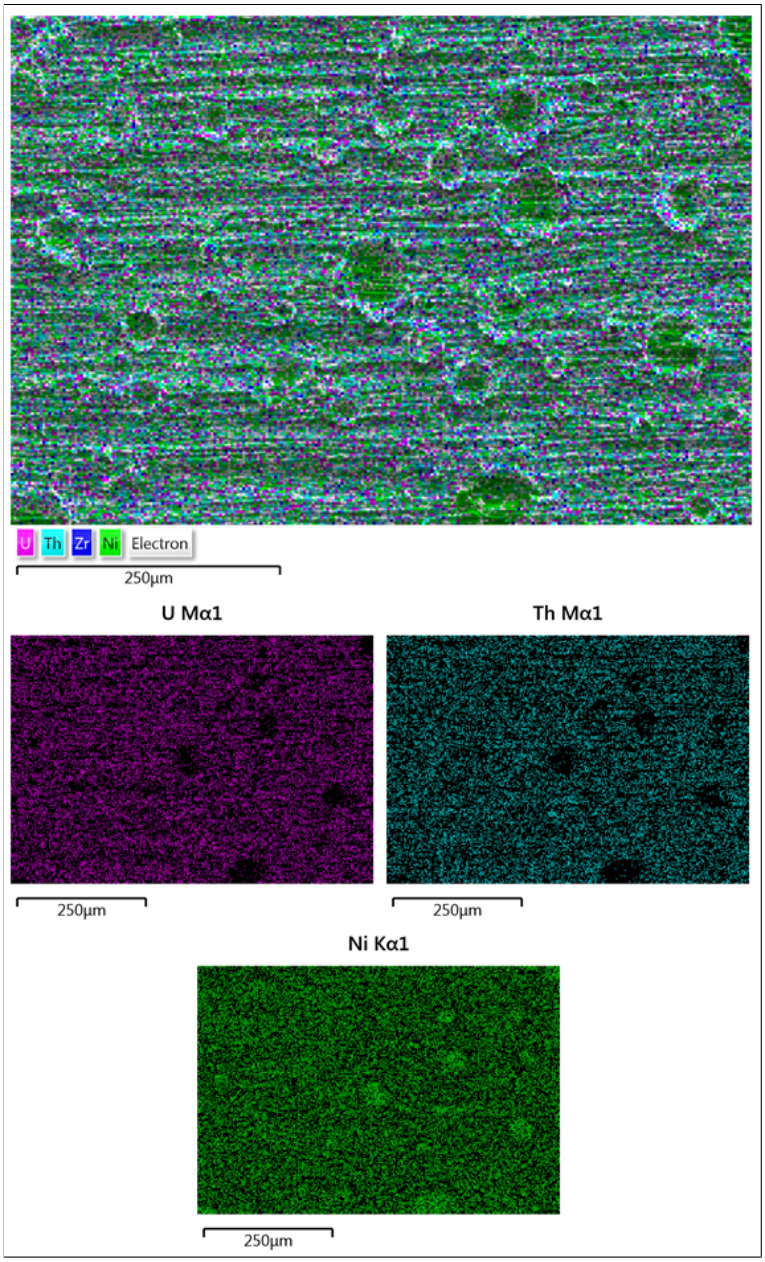

Figure 12.60. SEM-EDS map of Run #94. E_{pulse} = -2.40 V, E_{relax} = -2.12 V, T = 773 K, $c(ThCl_4)$ = 1.8 wt%, $c(UCl_3)$ = 2.2 wt%.

12.5.2 Factors behind unexpected matrix effects

12.5.2.1 Hypothesis formulation

The method assumed the deposition rates of Th and U from the Th-U mixed salts are the same as those from Th-only and U-only salts. Thus, the correlations used for single salts could be used to predict the total $ThCl_4$+UCl_3 concentration just based on the deposition time, as the Th and U deposition current contributions combine to integrate to the total measured charge. Alpha spectroscopy (or other method, here SEM-EDS) would then supply information about the ratio, and a complete picture of both analytes' concentrations could be reconstructed.

However, deposition times higher than expected ones were encountered in all cases (see Section 12.4.3). This result suggests that the deposition rate of the individual elements was lowered compared to single salt experiments. Furthermore, it was discovered that this retardation was mutual (affected both thorium and uranium).

A hypothesis explaining such behavior is presented. Based on the research of Bagri (111) (same LiCl−KCl melt, same temperature), the activity a_i of species i in the salt can be affected by the addition of another species j. Specifically, the activity coefficient γ_i tends to decrease. Since the equation for calculating activity:

$$a_i = \gamma_i c_i \tag{12.17}$$

only contains γ_i and concentration, and since concentration does not diminish, it is concluded that the activity a_i decreases.

If the model of decreasing activity is adopted, then Nernst equation (Equation 4.3) dictates that a shift in the cathodic direction in the equilibrium potential of the element occurs. This cathodic shift in equilibrium potential signifies that the applied overpotential is effectively decreased.

The equation for overpotential η (Equation 10.6) using Nernst equation for equilibrium potential (Equation 4.3) is reiterated here, this time with activity coefficients explicitly shown:

$$\eta = E - E^0 - \frac{RT}{zF} ln \frac{a_{Ox}}{a_{Red}} = E - E^0 - \frac{RT}{zF} ln \frac{\gamma_{ox} c_{ox}}{\gamma_{red} c_{red}} \tag{12.18}$$

In order for the method to work, the overpotential must be large enough to carry out the deposition under conditions of diffusion limitation (see Section 10.12.2).

However, with this cathodic shift the diffusion-limited regime might no longer be attained.

If that is the case, a mixed regime of reaction kinetics and diffusion is attained, where the value of potential does affect the deposition rate. A slight change in the overpotential changes the observed deposition rate (see Figure 10.1). Consequently, the method premise is not met, and results based on these measurements would be erroneous.

It is hypothesized that the deposition time retardation was caused by a decrease in individual deposition rates due to a switch from a diffusion-limited regime (maximum rate) to a mixed kinetics regime (lower than maximum rate). This switch was in turn caused by cathodic shift in equilibrium potential due to decrease in activities (in both species). A scheme showing this hypothesis is presented in Figure 12.61.

Thus, large fluctuations in deposition rates could be observed, dependent on the magnitude of shift away from the diffusion-limited kinetics. The deposition time can be significantly prolonged, but can never become shorter than the expected value according to the hypothesis. This is in accordance with the observations (see Figures 12.51, 12.53, 12.55, 12.57).

12.5.2.2 Hypothesis validation

In order to quantitatively support the hypothesis that the observed combined deposition rates are more affected by reaction kinetics than the previously observed rates for individual components, one should examine the following equation for deposition current density based on combined kinetic and diffusion-limited processes (112):

$$i = \frac{i_0[exp(\alpha z F \eta/RT) - exp(-\alpha z F \eta/RT)]}{1 + i_0[\frac{1}{i_l} exp(\alpha z F \eta/RT) - \frac{1}{i_l} exp(-\alpha z F \eta/RT)]} \tag{12.19}$$

This equation can be used to show whether the individual deposition experiments, and the combined deposition experiments were conducted under strict diffusion-limited regime or not. The equation collapses to either: (a) the Butler-Volmer equation (Equation 10.10) in the case of totally kinetically controlled system, or (b) the limiting current value i_l (see Section 10.3) in the case of diffusion-limited regime.

In order to evaluate the kinetic effects, Equation 12.19 is transformed so that the limiting current density i_l is the unknown variable, while i is supplied from the

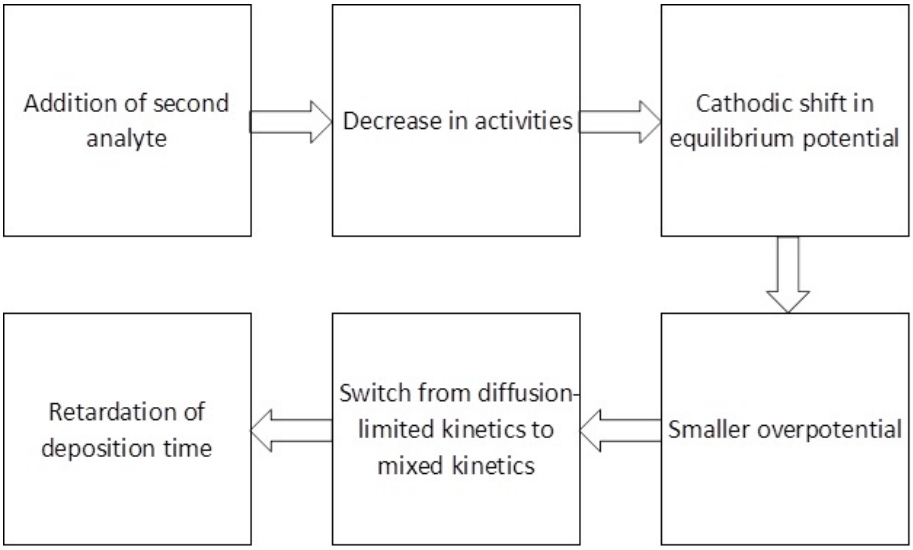

Figure 12.61. Hypothesis explaining the observed retardation of deposition times in mixed salts.

experiment. The transformation assumes the anodic process to be negligible:

$$i = \frac{-i_0\, exp(-\alpha z F\eta/RT)}{1 - \frac{i_0}{i_l}\, exp(-\alpha z F\eta/RT)} \tag{12.20}$$

$$1 - \frac{i_0}{i_l}\, exp(-\alpha z F\eta/RT) = \frac{-i_0\, exp(-\alpha z F\eta/RT)}{i} \tag{12.21}$$

$$i_l - i_0\, exp(-\alpha z F\eta/RT) = \frac{-i_0 i_l\, exp(-\alpha z F\eta/RT)}{i} \tag{12.22}$$

$$i_l + \frac{i_0 i_l\, exp(-\alpha z F\eta/RT)}{i} = i_0\, exp(-\alpha z F\eta/RT) \tag{12.23}$$

$$i_l(1 + \frac{i_0\, exp(-\alpha z F\eta/RT)}{i}) = i_0\, exp(-\alpha z F\eta/RT) \tag{12.24}$$

$$i_l = \frac{i_0\, exp(-\alpha z F\eta/RT)}{1 + \frac{i_0\, exp(-\alpha z F\eta/RT)}{i}} \tag{12.25}$$

If the resulting i_l value is similar to the experimental i, then the deviation from diffusion-limited kinetics is negligible. However, the values of α, i_0, E, and E_{eq} have too much uncertainty associated with them to meaningfully complete the analysis. Particularly in the two-analyte system, the $E_{eq,i}$ is uncertain as it is hypothesized to shift by an unknown amount due to decrease in individual species' activity. Consequently, activity coefficients γ_i for both analytes for the particular solution need to be known as well. Experiments should be run in the future to measure these properties in order to complete the analysis.

12.5.2.3 Deposit composition

These fluctuations in (total) deposition rates also augment differences in deposition rates between thorium and uranium. A slight change in overpotential can—outside diffusion-limited kinetics—have drastic impact on the ratio of deposited elements. One element can still find itself in the diffusion-limited regime and deposit at maximum rate (or be at a shoulder and deposit slightly slower than maximum rate), while the other element can be deep in the mixed kinetics regime and deposit at only a fraction of its maximum rate.

Inconsistent element ratios in the deposit were encountered (see Section 12.4.4) which supports this assertion of the method premise not being met. In the diffusion-limited regime, the deposit ratio should mirror the ratio of elements in the salt multiplied by a factor involving their diffusion coefficients (see Equation 12.13), but that was not observed.

If strict proportionality between salt and deposit ratios was not attained, the expectation was that uranium will be present in larger-than-proportional quantities since its redox potential is more anodic, suggesting larger overpotential applied to uranium than to thorium. Surprisingly, it was thorium that was (usually) present in larger-than-proportional quantities (a threshold value for thorium concentration appears to tell when it would start dominating).

To explain this behavior, another hypothesis is drawn that thorium activity coefficient γ_{Th} does not drop as sharply as uranium activity coefficient γ_U does when they are combined in a mixed salt, and consequently their redox potentials switch places (thorium becomes more anodic than uranium).

A relatively simple remedy can be applied to solve these undesirable matrix effects, in that a larger overpotential is applied, in order to force both elements back into the diffusion-limited kinetics. A caution needs to be exercised, however, since higher overpotentials bring with them undesirable effects on morphology (see Section 10.6.2). Extreme values of overpotential even promote undesirable solvent codeposition.

12.5.2.4 Deposition morphology

The last matrix effect discussed is the one pertaining to deposit morphology. It was shown in Section 12.4.5 that the alloying tendencies of uranium (which alone formed alloys with nickel substrate) are diminished by the presence of thorium. Consequently, layers of deposit more akin to the thorium-only case were encountered in the mixed salt, and uranium penetration into nickel substrate was suppressed.

Unlike in the deposit composition case—where threshold levels of thorium above 1.3 wt% triggered disproportionately richer thorium deposits—here even minor thorium additions to uranium-bearing salt are having dramatic effect on the morphology.

Thorium-uranium interaction during deposition likely interferes with the (previously observed) uranium-nickel interaction. The magnitude of the thorium-uranium interaction is significantly larger than the uranium-nickel interaction due to thorium being the dominant ion of the two actinides.

The dominance is inferred based on the hypothesis described in previous Section 12.5.2.3: the activity of thorium a_{Th} being greater than the activity of uranium a_U (due to thorium activity coefficient γ_{Th} decreasing less sharply than uranium activity coefficient γ_U in the mixed salt).

12.5.3 Benchmarking vs. voltammetry

It was established that under current conditions, the method is not able to produce any meaningful concentration determinations. Thus, a direct comparison with a different method is not possible.

However, a CV of the single and mixed salt is presented for reference (a multitude of these data was collected simultaneously during the experimental runs), to show that CV would also struggle in resolving the concentration information from the mixed salt.

Two figures are presented. Figure 12.62 displays CVs of relatively low concentrations of thorium and uranium, either alone or in a mix. Figure 12.63 displays CVs of relatively high concentrations of the two actinides.

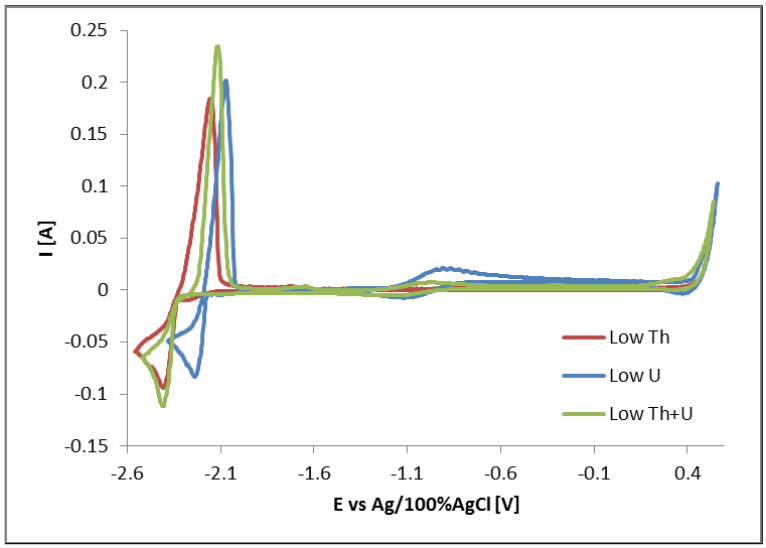

Figure 12.62. CVs of low concentrations of $ThCl_4$ and UCl_3 in LiCl−KCl. A = 1.2 cm^2, T = 773 K, ν = 200 mV s^{-1}, $c(ThCl_4)$ = 1.5 wt%, $c(UCl_3)$ = 1.6 wt%, $c(ThCl_4 + UCl_3)$ = 1.1+0.9 wt%. WE: W, CE: Zr, RE: [Ag/AgCl].

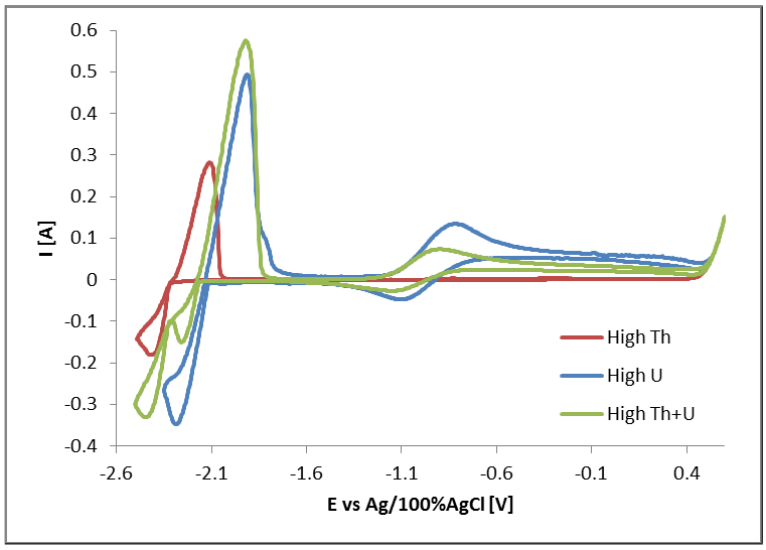

Figure 12.63. CVs of high concentrations of $ThCl_4$ and UCl_3 in LiCl−KCl. A = 1.2 cm^2, T = 773 K, ν = 200 mV s^{-1}, $c(ThCl_4)$ = 3.2 wt%, $c(UCl_3)$ = 5.8 wt%, $c(ThCl_4 + UCl_3)$ = 2.0+5.0 wt%. WE: W, CE: Zr, RE: [Ag/AgCl].

Figure 12.62 shows a complication, where the uranium peak in the mixed salt (green) practically disappears and only one peak in place of thorium is present. The magnitude of this peak is higher than that of thorium alone, which is evident from the comparison of concentrations of thorium in thorium-only salt (1.5 wt%, yet smaller peak) and in mixed salt (1.1 wt%, yet larger peak). Thus, this peak is a combination of thorium and uranium and needs to be deconvoluted (difficult). Consequently, concentration determination is not possible based on this figure, at least not with traditional univariate techniques.

Figure 12.63 resolves the above complication (at least partially), since both peaks in the mixed salt appear at their appropriate positions. However, the magnitude of the peaks in the mixed salt is not fully proportional to concentration. The magnitude of uranium peak is significantly diminished, much more than would be appropriate due to concentration difference (5.8 wt% in uranium-only vs. 5.0 wt% in mixed salt). The thorium peak, on the other hand, is significantly exaggerated—the magnitude is higher than that of thorium alone, albeit having lower concentration (3.2 wt% in thorium-only vs. 2.0 wt% in mixed salt). Consequently, concentration determination is very problematic here as well.

The issues with CV have previously been encountered in the *Part I* (see Section 6.4). Only there, the uranium peak retained its (proper) height and was amenable to relatively accurate concentration determination. The thorium peak was exaggerated, it was hypothesized to be due to increase in electrode area caused by prior uranium deposition.

CHAPTER 13

PART II CONCLUSIONS

A theoretical treatment of a novel analytical technique capable of determining actinide concentrations in molten salts—by combining electrodeposition and alpha spectroscopy—was introduced, and experimental verification of this technique was sought.

An electrochemical deposition at 773 K of thorium or uranium from LiCl-KCl-$ThCl_4$ and LiCl-KCl-UCl_3 systems, respectively, was performed to support the novel analytical technique. A stainless steel or nickel working electrode was used as a surrogate to alpha particle detector surface onto which the actinides deposited. Zirconium counter electrode was used to eliminate chlorine evolution during deposition.

The deposition mechanism of thorium on stainless steel and nickel was investigated under three different deposition techniques: chronopotentiometry, chronoamperometry, and repeating chronoamperometry; with the goal to acquire a 1 µm thick layer of deposit, free of dendrites.

Chronopotentiometry was found to be the least useful technique for electrodeposition. Under chronoamperometry, thorium deposition on stainless steel yielded somewhat satisfactory results, albeit dendritic formations were frequently encountered. Repeating chronoamperometry proved to be the most useful technique on both stainless steel and nickel. It suppressed the growth of dendrites at the expense of slightly higher codeposited zirconium content (from the counter electrode).

On stainless steel, globular interconnected formations of desired thickness with good surface coverage were obtained. On nickel, 3D island of roughly desired thickness with incomplete surface coverage were obtained. Here, some alloying tendencies were observed where thorium and nickel were present in location with no apparent surface deposits—this effectively compensated the incomplete surface coverage.

The deposition mechanism of uranium on nickel was investigated by repeating chronoamperometry. Significant alloying tendencies were observed, where uranium first merged with the nickel substrate. Only when this top nickel layer was saturated, deposits of pure uranium started forming on top of the nickel substrate. The tendency of uranium to form dendrites was suppressed, and thus satisfactory, alloyed deposits were obtained.

Due to reusability requirements of the alpha particle detector, the deposit needs to completely strip off the surface before a new measurement can commence. The stripping of both elements was investigated using chronoamperometry on nickel. Thorium was completely stripped away and no significant surface alterations were found. Uranium was nearly completely stripped away (a concentration of 0.5 at% remained) and no significant surface alterations were found.

The analytical technique expects the deposition time to be a function of concentration, and requires the construction of such correlation. Satisfactory correlation was created up to about 3.5 wt% $ThCl_4$, and up to about 6 wt% UCl_3. The correlation was of the $y = ax^b$ type. Unexpectedly, the correlation was almost identical for thorium and uranium.

Experiments in the mixed thorium uranium salts investigated the effects the individual actinides might have on each other (matrix effects). The effects (a) on deposition time, (b) on deposit ratio, and (c) on morphology of the deposit were investigated. An experimental matrix ranging between 0–2.5 wt% $ThCl_4$ and 0–5 wt% UCl_3 was established, with 16 individual data points collected within this space. Electrodeposition took place on nickel using repeating chronoamperometry.

(a) The effects on deposition time revealed that the deposition in the mixed salt was retarded in comparison to equivalent-concentration single-analyte runs (regardless whether thorium or uranium ones). This trend was consistent in all data points collected and prompted construction of a hypothesis to explain such effect.

The hypothesis assumes that the activity coefficient of one species was decreased by the introduction of the second species (whose activity coefficient also decreased). This prompted their respective redox potentials to shift cathodically, which in turn decreased the applied overpotential. The overpotential was no longer sufficient to

ensure deposition under diffusion-limited conditions (where maximum rate is attained). Instead, the deposition shifted into mixed kinetics conditions (where lower than maximum rate is attained) either for one or for both elements. Consequently, lower deposition rates were seen, requiring longer deposition time.

This supposed departure from diffusion-limited conditions prevents the new method from delivering meaningful concentration determinations. A recommendation for future runs is to increase the overpotential further, to retain diffusion-limited conditions.

(b) The effect of mixed salt on deposit ratios revealed that the expected ratios—which were prescribed to be proportional to salt concentrations of respective actinides—were not met. In some cases the deposit was richer in uranium more than expected, in most cases the deposit was richer in thorium more than expected. The effect is again ascribed to the violation of diffusion-limited deposition conditions.

In a few runs the expected ratio was achieved—these were the runs where absolute thorium content was below 1.5 wt%, and uranium content was below 3.2 wt%. Arguably, these runs were the least affected by decrease in activities and subsequent decrease in overpotential. A strong effect of thorium enrichment being higher than expected with increasing thorium content in the salt was noted.

(c) The last effect of mixed salt on deposit morphology revealed that uranium tendency to alloy with nickel was diminished by even small additions of thorium. Consequently, the mixed deposits were more resembling those seen by thorium-only depositions.

CV was selected to be a benchmark method to which the new analytical technique presented in this work would compare. Thus, CVs were collected simultaneously with the electrodeposition runs. Due to the failure of the new method to present meaningful data which could be compared to CV, no rigorous comparison between the two was attempted.

Instead, a couple CVs were presented to show that the concentration determination would be extremely problematic. The reason is the diminishing or complete disappearance of uranium peak in mixed salt at higher or lower uranium concentrations, respectively; and the exaggeration of thorium peak (actually mixed thorium-uranium peak) in mixed salt at practically all thorium concentrations. This effect was already

seen in the *Part I* when mixed thorium uranium salt was investigated using CV.

Regarding the feasibility of the new proposed analytical technique: if diffusion-limitation conditions are fulfilled in the mixed salt depositions, then this technique could bring accurate results, at least below 1.3 wt% thorium content and above 0.25 wt% uranium content. The combination of near real-time availability with the isotopic resolution (due to use of alpha spectroscopy) makes the technique very attractive for special nuclear applications, particularly the UNF electrorefiner.

Future work should explore the mixed salt depositions when diffusion-limited conditions are met. Furthermore, different material than nickel might be more appropriate as a surrogate to the alpha particle detector. Deposition parameters for this new material need to be optimized again, since this material can be dissimilar to nickel.

CHAPTER 14

FINAL CONCLUSION

The dissertation investigated actinide metal electrochemistry in a high temperature molten salt environment, with special attention given to real-time concentration monitoring in nuclear applications. In *Part I*, monitoring of thorium and uranium in fluoride salts, and in salt/bismuth system was investigated using cyclic voltammetry. In *Part II*, thorium and uranium monitoring in chloride salts was investigated using novel, hyphenated technique which combines a separation step (electrochemical separation) with a detection step (alpha particle spectroscopy).

In *Part I*, thorium and uranium reduction mechanisms previously investigated by other researchers have been verified. Values for diffusion coefficients for these two elements have been extracted over a concentration range (0.5–4.0 An wt%), and a trend line was produced from this data. This extends the library of diffusion coefficients, as other studies typically measured only one value at very low concentration (< 0.5 An wt%).

For real-time concentration monitoring in single-analyte salts, calibration curves of cathodic peak current densities vs. analyte concentration were produced up to 5 AnF_4 wt%. It was noted that the regression gave satisfactory results without the need to account for diffusion coefficient variation with concentration.

Experiments in the mixed thorium-uranium salt yielded satisfactory concentration monitoring of uranium, and problematic concentration monitoring for thorium. A method other than cyclic voltammetry needs to be used for thorium monitoring.

Experiments in salt/bismuth extraction showed that thorium readily extracts into bismuth phase if no uranium is present. Real-time uranium concentration monitoring was determined feasible.

In *Part II*, a theoretical treatment of the novel analytical technique was laid down.

The attractiveness of the novel technique stems from the combination of near real-time availability and isotopic resolution. The technique necessitated investigation of deposition mechanisms of thorium and uranium on stainless steel and nickel using various electrodeposition methods. Satisfactory deposits for both elements were achieved by a repeating chronoamperometry method, which was not previously reported in the literature.

For near real-time concentration monitoring in single-analyte salts, calibration curves of deposition time vs. analyte concentration were produced up to 3.5 $ThCl_4$ wt% and 6 UCl_3 wt%. Experiments in the mixed thorium-uranium salt identified serious interference between the two actinides (matrix effects). Investigated matrix effects pertain to variations in deposition time, deposit ratio, and morphology of the deposit.

The significant variation in deposition time prevented construction of meaningful concentration calibration curve for the mixed salt. A hypothesis has been formulated to explain the variation. A central piece of this hypothesis is the notion that activity of a species is diminished by the addition of second species. This in turn alters the equilibrium potential of the individual analyte and may shift the deposition condition away from the desired mass transfer-limited kinetics. This hypothesis is another contribution to the existing theoretical framework.

The variation in deposit ratio was again ascribed to the violation of mass transfer-limited kinetics. A strong effect of thorium enrichment being higher than expected with increasing thorium content was identified. The variation in deposit morphology revealed that thorium presence diminishes the uranium tendency to form alloys with nickel. The mixed deposits were resembling the ones collected in thorium-only runs. Overall, thorium appears to be the dominant species as variations in its concentration produce more dramatic changes than variations in uranium concentration. These findings constitute a new contribution to the existing body of knowledge.

Thus, the idea of real-time concentration monitoring was investigated in both parts, while each part approached the problem from a different angle. Both parts brought new findings to the field, *Part I* brought mostly experimental findings, while *Part II* brought a theoretical framework to support a novel analytical method.

REFERENCES

[1] Schrader, G. F.; Elshennawy, A. K. *Manufacturing Processes and Materials*; Society of Manufacturing Engineers, Dearborn, MI, 2000.

[2] Lane, J.; MacPherson, H.; Maslan, F. *Fluid Fuel Reactors*; Addison-Wesley, Reading, MA, 1958.

[3] Rosenthal, M.; Kasten, P.; Briggs, R. *Nucl. Technol.* **1970**, *8*, 107–117.

[4] Grimes, W. *Nucl. Technol.* **1970**, *8*, 137–155.

[5] Haubenreich, P. N.; Engel, J. *Nucl. Technol.* **1970**, *8*, 118–136.

[6] McFarlane, H. *Prog. Nucl. Energy* **2014**, *77*, 1–420.

[7] Whatley, M.; McNeese, L.; Carter, W.; Ferris, L.; Nicholson, E. *Nucl. Technol.* **1970**, *8*, 170–178.

[8] Flibe Energy, http://flibe-energy.com (accessed 2017–05–05).

[9] National Research Council, *Electrometallurgical Techniques for DOE Spent Fuel Treatment*; National Academies Press, 2000.

[10] Lee, H.; Park, G.-I.; Lee, J.-W.; Kang, K.-H.; Hur, J.-M.; Kim, J.-G.; Paek, S.; Kim, I.-T.; Cho, I.-J. *Sci. Technol. Nucl. Install.* **2013**, *2013*.

[11] Stika, M.; Rappleye, D.; Simpson, M. F.; Jeong, S. M. *AIChE J.* **2016**,

[12] Uhlíř, J. *J. Nucl. Mater.* **2007**, *360*, 6–11.

[13] Khokhlov, V.; Ignatiev, V.; Afonichkin, V. *J. Fluorine Chem.* **2009**, *130*, 30–37.

[14] Hargraves, R. B. *Thorium: Energy Cheaper Than Coal*; Createspace, 2012.

[15] Elsheikh, B. M. *J. Radiat. Res. Appl. Sci.* **2013**, *6*, 63–70.

[16] Serp, J.; Allibert, M.; Beneš, O.; Delpech, S.; Feynberg, O.; Ghetta, V.; Heuer, D.; Holcomb, D.; Ignatiev, V.; Kloosterman, J. L. *Prog. Nucl. Energy* **2014**, *77*, 308–319.

[17] Chamelot, P.; Massot, L.; Hamel, C.; Nourry, C.; Taxil, P. *J. Nucl. Mater.* **2007**, *360*, 64–74.

[18] Lacquement, J.; Boussier, H.; Laplace, A.; Conocar, O.; Grandjean, A. *J. Fluorine Chem.* **2009**, *130*, 18–21.

[19] Apple, R. F. *Method No. 9021206, ORNL Master Analytical Manual*; 1965; Technical Report for Oak Ridge National Laboratory: Oak Ridge, TN.

[20] Thoma, R. E. *MSR Program Semiannual Progress Report, ORNL-4344*; 1968; Technical Report for Oak Ridge National Laboratory: Oak Ridge, TN.

[21] Carter, W.; Nicholson, E. *Design and cost study of a fluorination–reductive extraction–metal transfer processing plant for the MSBR*; 1972; Technical Report for Oak Ridge National Laboratory: Oak Ridge, TN.

[22] Straka, M.; Korenko, M.; Lisỳ, F. *J. Radioanal. Nucl. Chem.* **2010**, *284*, 245–252.

[23] Nourry, C.; Souček, P.; Massot, L.; Malmbeck, R.; Chamelot, P.; Glatz, J.-P. *J. Nucl. Mater.* **2012**, *430*, 58–63.

[24] Chamelot, P.; Massot, L.; Cassayre, L.; Taxil, P. *Electrochim. Acta* **2010**, *55*, 4758–4764.

[25] Hamel, C.; Chamelot, P.; Laplace, A.; Walle, E.; Dugne, O.; Taxil, P. *Electrochim. Acta* **2007**, *52*, 3995–4003.

[26] Afonichkin, V.; Bovet, A.; Shishkin, V. *J. Nucl. Mater.* **2011**, *419*, 347–352.

[27] Gibilaro, M.; Massot, L.; Chamelot, P.; Taxil, P. *Electrochim. Acta* **2009**, *54*, 5300–5306.

[28] Gibilaro, M.; Massot, L.; Chamelot, P.; Taxil, P. *J. Nucl. Mater.* **2008**, *382*, 39–45.

[29] Taxil, P.; Massot, L.; Nourry, C.; Gibilaro, M.; Chamelot, P.; Cassayre, L. *J. Fluorine Chem.* **2009**, *130*, 94–101.

[30] Bard, A. J.; Faulkner, L. R. *Electrochemical methods: Fundamentals and Applications, 2nd Edition*; Wiley New York, 2001.

[31] Matsumiya, M.; Takagi, R.; Fujita, R. *J. Nucl. Sci. Technol.* **1998**, *35*, 137–147.

[32] Matsuda, H.; Ayabe, Y. *Electrochemistry* **1955**, *59*, 494.

[33] Berzins, T.; Delahay, P. *J. Am. Chem. Soc.* **1953**, *75*, 555–559.

[34] Nicholson, M. *J. Am. Chem. Soc.* **1957**, *79*, 7–12.

[35] Shimada, T.; Iizuka, M.; Ito, Y. *Denki Kagaku* **1992**, *60*, 200–211.

[36] Hikino, S.; Xie, G.; Ema, K.; Ito, Y.; Shou, Z. M. *J. Electrochem. Soc.* **1992**, *139*, 1820–1824.

[37] Cottrell, F. *Z. Phys. Chem.* **1903**, *42*, 385–431.

[38] Rappleye, D.; Jeong, S.-M.; Simpson, M. *Ann. Nucl. Energy* **2015**, *77*, 265–272.

[39] Dalrymple-Alford, P.; Goto, M.; Oldham, K. B. *J. Electroanal. Chem. Interfacial Electrochem.* **1977**, *85*, 1–15.

[40] Oldham, K. B.; Spanier, J. *J. Math. Anal. Appl.* **1972**, *39*, 655–669.

[41] Berghoute, Y.; Salmi, A.; Lantelme, F. *J. Electroanal. Chem.* **1994**, *365*, 171–177.

[42] Saïla, A.; Gibilaro, M.; Massot, L.; Chamelot, P.; Taxil, P.; Affoune, A.-M. *J. Electroanal. Chem.* **2010**, *642*, 150–156.

[43] Outotec, Research Center, HSC Chemistry, v7.11. http://www.outotec.com/hsc (accessed 2017-05-05).

[44] Clayton, F.; Mamantov, G.; Manning, D. *J. Electrochem. Soc.* **1974**, *121*, 86–90.

[45] Tylka, M.; Willit, J.; Prakash, J.; Williamson, M. *J. Electrochem. Soc.* **2015**, *162*, H852–H859.

[46] Rough, F. A.; Bauer, A. A. *Constitution of Uranium and Thorium Alloys*; Battelle Memorial Institute, 1958; Vol. BMI-1300.

[47] Stika, M.; Chaiken, M.; Jarrell, J.; Blue, T.; Cao, L. R.; Simpson, M. F. *ECS Trans.* **2016**, *75*, 603–608.

[48] Stika, M.; Padilla, S.; Jarrell, J.; Blue, T.; Cao, L.; Simpson, M. *J. Electrochem. Soc.* **2017**, *164*, H5078–H5085.

[49] Till, C.; Chang, Y.; Hannum, W. *Prog. Nucl. Energy* **1997**, *31*, 3–11.

[50] Till, C.; Chang, Y. I. *Plentiful Energy: The Story of the Integral Fast Reactor*; CreateSpace, Amazon, 2011.

[51] Inoue, T.; Koyama, T.; Arai, Y. *Energy Procedia* **2011**, *7*, 405–413.

[52] Nagarajan, K.; Reddy, B. P.; Ghosh, S.; Ravisankar, G.; Mohandas, K.; Mudali, U. K.; Kutty, K.; Viswanathan, K. K.; Babu, C. A.; Kalyanasundaram, P. *Energy Procedia* **2011**, *7*, 431–436.

[53] Guoan, Y.; Hui, H.; Rushan, L.; Wenbin, Z. *Procedia Chem.* **2012**, *7*, 215–221.

[54] Taylor, R. *Reprocessing and Recycling of Spent Nuclear Fuel*; Elsevier, 2015.

[55] Park, S. W. *Bull. At. Sci.* **2009**, *26*, 273–288.

[56] Gray, J. *Utility Week* **Mar 2015**, 22–23.

[57] Wade, D.; Chang, Y. *Nucl. Sci. Eng.* **1988**, *100*, 507–524.

[58] Planchon, H.; Sackett, J.; Golden, G.; Sevy, R. *Nucl. Eng. Des.* **1987**, *101*, 75–90.

[59] Vaden, D. *Sep. Sci. Technol.* **2006**, *41*, 2003–2012.

[60] Byung-ki Park, A Time-Dependent Simulation of Molten Salt Electrolysis for Nuclear Wastes Transmutation. Ph.D. thesis, Seoul National University, 1999.

[61] Cumberland, R. M.; Yim, M.-S. *Ann. Nucl. Energy* **2014**, *71*, 52–59.

[62] Rappleye, D. Developing Safeguards for Pyroprocessing: Detection of a Plutonium Co-deposition on Solid Cathode in an Electrorefiner by Applying the Signature-Based Safeguards Approach. M.Sc. thesis, North Carolina State University, 2012.

[63] Effenberger, A. J. Methods for Measurement of Heterogeneous Materials with Laser-Induced Breakdown Spectroscopy (LIBS). Ph.D. thesis, University of California, San Diego, 2009.

[64] Hanson, C.; Phongikaroon, S.; Scott, J. R. *Spectrochim. Acta, Part B* **2014**, *97*, 79–85.

[65] Poa, D.; Tomczuk, Z.; Steunenberg, R. *J. Electrochem. Soc.* **1988**, *135*, 1161–1166.

[66] Iizuka, M.; Inoue, T.; Shirai, O.; Iwai, T.; Arai, Y. *J. Nucl. Mater.* **2001**, *297*, 43–51.

[67] Paek, S.; Kim, T.-J.; Kim, G.-Y.; Ahn, D.-H.; Kim, S.; Jung, Y. *Int. J. Electrochem. Sci* **2014**, *9*, 4925–4931.

[68] Tylka, M.; Willit, J.; Prakash, J.; Williamson, M. *J. Electrochem. Soc.* **2015**, *162*, H625–H633.

[69] Rappleye, D. S. Electrochemical Concentration Measurements for Multianalyte Mixtures in Simulated Electrorefiner Salt. Ph.D. thesis, University of Utah, 2016.

[70] Cao, Lei R, *Monitoring of Actinide Concentrations in Molten LiCl-KCl Salt using Alpha Spectroscopy*; 2015; Department of Energy's Nuclear Energy University Program Report Project No. CFA-15-8074: https://neup.inl.gov/.

[71] Garcia, T. R.; Reinke, B.; Windl, W.; Blue, T. E. *Nucl. Instrum. Methods Phys. Res., Sect. A* **2015**, *780*, 119–126.

[72] de Sanoit, J.; Tran, T. Q.; Pomorski, M.; Pierre, S.; Mer-Calfati, C.; Bergonzo, P. *Appl. Radiat. Isot.* **2013**, *80*, 32–41.

[73] Tran, Q.; Pomorski, M.; de Sanoit, J.; Mer-Calfati, C.; Scorsone, E.; Bergonzo, P. *IEEE Trans. Nucl. Sci.* **2014**, *61*, 2082–2089.

[74] Popov, K.; Grgur, B.; Djokić, S. S. *Fundamental Aspects of Electrometallurgy*; Springer Science & Business Media, 2007.

[75] Knoll, G. F. *Radiation Detection and Measurement*; John Wiley & Sons, 2010.

[76] Schulz, W. W. *Encyclopædia Britannica*; 2014; https://www.britannica.com/technology/thorium-processing/ (accessed 2017-05-05).

[77] Evans, D.; Raynor, G. *J. Nucl. Mater.* **1959**, *1*, 281–288.

[78] Grenthe, I.; Drożdżyński, J.; Fujino, T.; Buck, E. C.; Albrecht-Schmitt, T. E.; Wolf, S. F. *Uranium in The Chemistry of the Actinide and Transactinide Elements*; Springer, 2008.

[79] Schulz, W. W. *Encyclopædia Britannica*; 1998; https://www.britannica.com/technology/uranium-processing/ (accessed 2017-05-05).

[80] Schnell, I.; Albers, R. *J. Phys. Condens. Matter* **2006**, *18*, 1483.

[81] Jamieson, J. *High Temp.-High Pres.* **1973**, *5*, 123–131.

[82] Taylor, A. *J. Inst. Met.* **1950**, *77*, 585–594.

[83] Pimpinelli, A.; Villain, J. *Physics of Crystal Growth*; Cambridge University Press, Cambridge, 1998; Vol. 53.

[84] Popov, K.; Maksimović, M. *Mod. Aspects Electrochem.* **1989**, *19*, 193.

[85] Sand, H. J. *Lond. Edinb. Dubl. Phil. Mag.* **1901**, *1*, 45–79.

[86] Cohen, U. *J. Electrochem. Soc.* **1981**, *128*, 731–740.

[87] Marshall, S.; Redey, L.; Vandegrift, G. F.; Vissers, D. *Electroformation of uranium hemispherical shells*; 1989; Technical Report for Argonne National Laboratory: Argonne, IL.

[88] Yang, Y.; Li, Y.; Pritzker, M. *Electrochim. Acta* **2016**, *213*, 225–235.

[89] JEOL Ltd, Energy Table for EDS Analysis. http://www.jeolusa.com/resources/electron-optics/ (accessed 2017-05-05).

[90] Ehl, R. G.; Ihde, A. J. *J. Chem. Educ.* **1954**, *31*, 226.

[91] Plambeck, J. A. *J. Chem. Eng. Data* **1967**, *12*, 77–82.

[92] Rappleye, D.; Teaford, K.; Simpson, M. F. *Electrochim. Acta* **2016**, *219*, 721–733.

[93] Ziegler, J. F.; Ziegler, M. D.; Biersack, J. P. *Nucl. Instrum. Methods Phys. Res., Sect. B* **2010**, *268*, 1818–1823.

[94] Tomczuk, Z.; Ackerman, J. P.; Wolson, R. D.; Miller, W. E. *J. Electrochem. Soc.* **1992**, *139*, 3523–3528.

[95] Ahluwalia, R. K.; Hua, T. Q.; Vaden, D. *Nucl. Technol.* **2004**, *145*, 67–81.

[96] Okamoto, H. *J. Phase Equilib.* **1991**, *12*, 704–705.

[97] Peterson, D. *J. Phase Equilib.* **1988**, *9*, 490–493.

[98] Pakhui, G.; Chandra, M.; Ghosh, S.; Reddy, B. P.; Nagarajan, K. *Electrochim. Acta* **2015**, *155*, 372–382.

[99] Liu, K.; Yuan, L.-Y.; Liu, Y.-L.; Zhao, X.-L.; He, H.; Ye, G.-A.; Chai, Z.-F.; Shi, W.-Q. *Electrochim. Acta* **2014**, *130*, 650–659.

[100] Cassayre, L.; Serp, J.; Soucek, P.; Malmbeck, R.; Rebizant, J.; Glatz, J.-P. *Electrochim. Acta* **2007**, *52*, 7432–7437.

[101] Martinot, L. *J. Radioanal. Nucl. Chem.* **1986**, *103*, 357–363.

[102] Gunawardena, G.; Hills, G.; Montenegro, I.; Scharifker, B. *J. Electroanal. Chem. Interfacial Electrochem.* **1982**, *138*, 225–239.

[103] Scharifker, B.; Hills, G. *Electrochim. Acta* **1983**, *28*, 879–889.

[104] Massot, L.; Chamelot, P.; Palau, P.; Taxil, P. *Electrochim. Acta* **2005**, *50*, 5408–5413.

[105] Reddy, B. P.; Vandarkuzhali, S.; Subramanian, T.; Venkatesh, P. *Electrochim. Acta* **2004**, *49*, 2471–2478.

[106] Shirai, O.; Iwai, T.; Suzuki, Y.; Sakamura, Y.; Tanaka, H. *J. Alloys Compd.* **1998**, *271*, 685–688.

[107] Masset, P.; Bottomley, D.; Konings, R.; Malmbeck, R.; Rodrigues, A.; Serp, J.; Glatz, J.-P. *J. Electrochem. Soc.* **2005**, *152*, A1109–A1115.

[108] Masset, P.; Konings, R. J.; Malmbeck, R.; Serp, J.; Glatz, J.-P. *J. Nucl. Mater.* **2005**, *344*, 173–179.

[109] Serrano, K.; Taxil, P. *J. Appl. Electrochem.* **1999**, *29*, 505–510.

[110] Serrano, K.; Taxil, P. *J. Appl. Electrochem.* **1999**, *29*, 497–503.

[111] Bagri, P.; Simpson, M. F. *J. Electrochem. Soc.* **2017**, *164*, H5299–H5307.

[112] Free, M. L. *Hydrometallurgy: Fundamentals and Applications*; John Wiley & Sons, 2013.